POLYTECHNIC OF TURIN

Faculty of Engineering
Master’s Degree in Aerospace Engineering

Master Thesis

Analysis of bonded joints for composite structures

Advisors:
prof. Erasmo Carrera
prof. Anita Catapano
prof. Alfonso Pagani
Co-advisors:
dott. Alberto Garcia de Miguel
dott. Enrico Panettieri

Candidate:
Luca Rizzo

March 2018

"We can be Heroes.
Just for one day."
David Bowie

Acknowledgements

I will be forever thankful to prof. Carrera, prof. Pagani and Dr. de Miguel of Politecnico di Torino for the opportunity they gave me to study and live abroad for my Master Thesis and for the constance and helpfulness they had for me during this year of work together.

I thank the entire MUL^2 *Group*, too, because I really felt part of it.

I want to express my deepest gratitude to prof. Catapano and Dr. Panettieri of the I2M - Bordeaux because they hosted me in their university, they followed me with patience and wisdom during the 5 months I stayed with them and they helped me in the first part of my experience which was the most difficult. With them, I thank all my colleagues of I2M who were able to make me feel home: Sarah, Torquato, Pierre, Léna, Timothée, Justine, Louise, Marie-Fraise, Mafoud, Aurore and Hamza. I express a special mention to my dear friend and colleague Khaustubha who helped me a lot of times and was able to calm me down when I can't go on with my work: thanks for everything you did for me.

I thank the "Italo-bordolesi" Martina, Pietro and Chiara and especially Francesco who shared with me a lot of voyages, trains, shops, beers, Ubers, cities, laughs and photos: I won't forget this experience which was great mostly for your support and sympathy.

Thanks to my university friend of the "JJ fans" who shared with me these long years and a special thanks to Bogdan who is the best friend that everyone should have in his life.

Thanks to my dearest friend of "Capolinea" Giulio, Alberto, Ilaria, Giulia, Alessandro, Giulia, Luca, Riccardo and Valentina because they are unique, rare and irreplaceable.

My family: papà Domenico, mamma Leonarda, Erika, Daniele, my grandmother Lucia, my cousins Simona, Luca and Antonio, my uncle Pasquale and my aunt Mara; thanks for what you are, thanks for what you did for me and my studies and thanks for what you will do forever for me.

Summary

The aims of this work, written jointly between Politecnico di Torino and Institut de Mécanique et d'Ingénierie - Université de Bordeaux, are the study of adhesive composite bonded joints and the assessment of the MUL^2 *CODE*, a software developed by the MUL^2 Research Group - Department of Mechanical and Aerospace Engineering of Politecnico di Torino (DIMEAS), for the accurate stress analysis of composite structures. The MUL^2 *CODE* is implemented through the Carrera Unified Formulation (CUF) for 1D structures based on Hierarchical Legendre Expansion (HLE) polynomials.
In the first part of the thesis, the adhesive bonding techniques are investigated and a comparison with mechanical joints is shown: the adhesive bonding method does not provoke preliminary damages as the mechanical bonding (riveting or drilling) which cause locally concentrations of stresses. For this reason, adhesive joints are more and more used in aerospace and mechanical engineering, which require high performances and versatility. On the other hand, adhesive technology on composite structures represents a challenge for several reasons: first of all, the progressive switch from metallic structures in favour of composites, then the impossibility to carry out a direct inspection of each element and, at last, the complex numerical study of the adhesive joints. In order to reduce the computational cost of analysis, CUF 1D is used, according to which the three-dimensional displacements field can be expressed as an arbitrary expansion of the generalized displacements. This theory is able to reduce a 3D problem into a 1D problem whose one-dimensional elements are computationally simpler, but very efficient for the lap analysis, than 3D models.
In the second part, the numerical results for different types of joints (butt joint, single lap joint and hybrid-adhesive double lap joint) are presented. The MUL^2 *CODE* can perform studies with two approaches: the first models the structure through its own thickness, managing to evaluate stress and strain field modelling the lap joint as a thick plate with many composite layers, the latter approach models the structure through its longitudinal axis, enabling to make the most of the beam one-dimensional representation of the joint. Results obtained with the code have been validated through literature benchmarks, a parametric *Python* code and the commercial finite element package ABAQUS, demonstrating the solidity of the software. Finally, an examination of crack propagation in a cohesive element is proposed.

Sommario

Gli obiettivi di questa tesi, scritta in unione tra il Politecnico di Torino e l'Institut de Mécanique et d'Ingénierie - Université de Bordeaux, sono lo studio dei giunti incollati in materiale composito e la validazione del MUL^2 *CODE*, un software sviluppato dal MUL^2 Research Group - Dipartimento di Ingegneria Meccanica e Aerospaziale del Politecnico di Torino (DIMEAS). Tale codice è implementato attraverso la Carrera Unified Formulation (CUF) per le strutture 1D e basato sull'espansione polinomiale di Legendre (Hierarchical Legendre Expansion, HLE).

Nella prima parte della tesi, sono studiate le tecniche di incollaggio ed è proposto un confronto con le giunzioni meccaniche: il metodo di giunzione adesiva non provoca danneggiamenti preliminari come il metodo di giunzione meccanica (utilizzo di rivetti o perforazioni con trapano) che causano concentrazioni locali di stress e, perciò, è sempre più utilizzato nell'ingegneria aerospaziale e meccanica, le quali richiedono elevate performances e versatilità. Dall'altro lato, la tecnica dell'incollaggio sui materiali compositi rappresenta una sfida per diverse ragioni: innanzitutto a causa del progressivo abbandono delle strutture metalliche in favore dei compositi, poi per l'impossibilità di effettuare una ispezione diretta di ogni elemento e, infine, per il complesso studio numerico di questi elementi. Al fine di ridurre il costo computazionale delle analisi, la CUF 1D può essere impiegata con successo, secondo la quale il campo di spostamenti tridimensionale può essere espresso come una espansione arbitraria dei generici spostamenti: questa teoria è in grado di ridurre un problema 3D ad un problema 1D i cui elementi unidimensionali sono computazionalmente più semplici, ma molto più efficienti per le analisi dei giunti, rispetto ai modelli 3D.

Nella seconda parte della tesi, sono presentati i risultati numerici per i diversi tipi di giunti studiati (butt joint, single lap joint e hybrid-adhesive double lap joint). Il MUL^2 *CODE* può realizzare analisi in due modi differenti: il primo modella la struttura attraverso il suo spessore, riuscendo a valutare il campo di spostamenti e tensioni modellando il lap joint come una piastra spessa costituita da molti layers in composito, il secondo approccio modella la struttura lungo il suo asse longitudinale, riuscendo così a sfruttare a pieno la rappresentazione del lap joint come una trave unidimensionale proposta in questo lavoro. I risultati ottenuti con il codice sono stati validati con dei casi di studio da letteratura, un codice *Python* parametrico e il software commerciale agli elementi finiti ABAQUS, dimostrando così la solidità di tale software di calcolo. Infine, è proposta una analisi della propagazione del danno in un elemento coesivo.

Contents

List of Figures

List of Tables

Chapter 1

Elasticity and classical 1D and 2D theories

1.1 The Hooke's law for orthotropic materials

The early studies about the correlation between mechanical strain and deformation on solid bodies were made by Robert Hooke who stated that each solid body warps by shortening or by extending when stressed and such deformation vanishes if stress is removed.
Hooke resumed this fundamental physical principle in the Latin statement *"Ut tensio, sic vis"*, i.e. it's actually that stress (*tensio*) which allows the body to develop an opposite reaction (*vis*) to the external loads applied; a direct proportionality between stress and strain can be defined by virtue of the *Hooke's Law*:

$$\sigma = c\ \varepsilon \tag{1.1}$$

where σ is the stress tensor, c is the *elastic stiffness tensor* of the material and, at last, ε is the strain tensor. If the tensors above are described in terms of components with respect to an orthonormal coordinate system, it is possible to write:

$$\sigma_{ij} = c_{ijkl}\ \varepsilon_{kl} \tag{1.2}$$

but, since the stress and strain tensors are symmetric, for an anisotropic material the tensor c has the following tensorial symmetries:

$$c_{ijkl} = c_{jikl} \qquad c_{ijkl} = c_{ijlk} \qquad c_{ijkl} = c_{klij}, \quad \text{with } i, j, k, l = 1,2,3 \tag{1.3}$$

Hence, using the Voigt's notation [52][12]:

$$\sigma_i = C_{ij}\varepsilon_i, \quad i, j = 1, \ldots, 6 \tag{1.4}$$

with:

$$\{\sigma\} = \left\{ \begin{matrix} \sigma_1 \\ \sigma_2 \\ \sigma_3 \\ \sigma_4 = \tau_{23} \\ \sigma_5 = \tau_{13} \\ \sigma_6 = \tau_{12} \end{matrix} \right\} \qquad \{\varepsilon\} = \left\{ \begin{matrix} \varepsilon_1 \\ \varepsilon_2 \\ \varepsilon_3 \\ \varepsilon_4 = 2\varepsilon_{23} = \gamma_{23} \\ \varepsilon_5 = 2\varepsilon_{13} = \gamma_{13} \\ \varepsilon_6 = 2\varepsilon_{12} = \gamma_{12} \end{matrix} \right\} \tag{1.5}$$

and $[C] \in \mathbb{R}^{6x6}$ as the stiffness matrix, the generalized Hooke's law can be rewritten as follows:

$$\{\sigma\} = [C]\,\{\varepsilon\} \tag{1.6}$$

A completely anisotropic material is characterised by 21 independent elastic components[12], but anisotropic materials (as composites) present often some material symmetries, providing an identical mechanical behaviour with respect to a set of the equivalent directions. The orthogonal symmetry with respect to a plane reduces the 21 elements of the stiffness matrix to 13 because of these relations:

$$C_{41} = C_{42} = C_{43} = C_{46} = C_{51} = C_{52} = C_{53} = C_{56} = 0 \tag{1.7}$$

and this type of material is called *monoclinic*.
The symmetry with respect to three orthogonal planes reduces the 13 elements of the stiffness matrix to only 9 introducing these relations:

$$C_{61} = C_{62} = C_{63} = C_{45} = 0 \tag{1.8}$$

and such a kind of material is called *orthotropic*. Thus, the complete expression of the stiffness matrix for an orthotropic material is the following:

$$\mathbf{C} = \begin{bmatrix} C_{11} & C_{12} & C_{13} & 0 & 0 & 0 \\ C_{12} & C_{22} & C_{23} & 0 & 0 & 0 \\ C_{13} & C_{23} & C_{33} & 0 & 0 & 0 \\ 0 & 0 & 0 & C_{44} & 0 & 0 \\ 0 & 0 & 0 & 0 & C_{55} & 0 \\ 0 & 0 & 0 & 0 & 0 & C_{66} \end{bmatrix} \tag{1.9}$$

Introducing the Young's modulus E, the mathematical formulation of eq. 1.1 becomes:

$$\sigma = E\ \varepsilon \tag{1.10}$$

The Young's modulus (usually measured in [GPa]) quantifies the stiffness of the material and it is, thus, the direct expression of the toughness, that it's shown elastically, to the shape change of the material subjected to stress.

The *Shear modulus* G is described by a function of E:

$$G = \frac{E}{2(1+\nu)} \tag{1.11}$$

and considering ν as the *Poisson's ratio*, eq. 1.6 and 1.9 can be joined in order to state:

$$\begin{Bmatrix} \sigma_1 \\ \sigma_2 \\ \sigma_3 \\ \tau_{23} \\ \tau_{13} \\ \tau_{12} \end{Bmatrix} = \begin{bmatrix} \frac{1-\nu_{23}\nu_{32}}{E_2E_3\Delta} & \frac{\nu_{21}+\nu_{23}\nu_{31}}{E_2E_3\Delta} & \frac{\nu_{31}+\nu_{21}\nu_{32}}{E_2E_3\Delta} & 0 & 0 & 0 \\ \frac{\nu_{21}+\nu_{23}\nu_{31}}{E_2E_3\Delta} & \frac{1-\nu_{13}\nu_{31}}{E_1E_3\Delta} & \frac{\nu_{32}+\nu_{12}\nu_{31}}{E_1E_3\Delta} & 0 & 0 & 0 \\ \frac{\nu_{31}+\nu_{21}\nu_{32}}{E_2E_3\Delta} & \frac{\nu_{32}+\nu_{12}\nu_{31}}{E_1E_3\Delta} & \frac{1-\nu_{12}\nu_{21}}{E_1E_2\Delta} & 0 & 0 & 0 \\ 0 & 0 & 0 & G_{23} & 0 & 0 \\ 0 & 0 & 0 & 0 & G_{31} & 0 \\ 0 & 0 & 0 & 0 & 0 & G_{12} \end{bmatrix} \begin{Bmatrix} \varepsilon_1 \\ \varepsilon_2 \\ \varepsilon_3 \\ \gamma_{23} \\ \gamma_{13} \\ \gamma_{12} \end{Bmatrix} \tag{1.12}$$

where

$$\Delta = \frac{(1-\nu_{12}\nu_{21}-\nu_{23}\nu_{32}-\nu_{13}\nu_{31}-2\nu_{21}\nu_{32}\nu_{13}}{E_1E_2E_3} \tag{1.13}$$

is the determinant of the stiffness matrix in eq. 1.12.
Reversing the equation, the *Compliance Matrix* $[S]$ can be written as:

$$\{\varepsilon\} = [S]\{\sigma\} \tag{1.14}$$

which can be reformulated as:

$$\mathbf{S} = \begin{bmatrix} S_{11} & S_{12} & S_{13} & 0 & 0 & 0 \\ S_{12} & S_{22} & S_{23} & 0 & 0 & 0 \\ S_{13} & S_{23} & S_{33} & 0 & 0 & 0 \\ 0 & 0 & 0 & S_{44} & 0 & 0 \\ 0 & 0 & 0 & 0 & S_{55} & 0 \\ 0 & 0 & 0 & 0 & 0 & S_{66} \end{bmatrix} \tag{1.15}$$

whose complete expression is:

$$\begin{Bmatrix} \varepsilon_1 \\ \varepsilon_2 \\ \varepsilon_3 \\ \gamma_{23} \\ \gamma_{13} \\ \gamma_{12} \end{Bmatrix} = \begin{bmatrix} \frac{1}{E_1} & \frac{-\nu_{21}}{E_2} & \frac{-\nu_{31}}{E_3} & 0 & 0 & 0 \\ \frac{-\nu_{12}}{E_1} & \frac{1}{E_2} & \frac{-\nu_{32}}{E_3} & 0 & 0 & 0 \\ \frac{-\nu_{13}}{E_1} & \frac{-\nu_{23}}{E_2} & \frac{1}{E_3} & 0 & 0 & 0 \\ 0 & 0 & 0 & \frac{1}{G_{23}} & 0 & 0 \\ 0 & 0 & 0 & 0 & \frac{1}{G_{13}} & 0 \\ 0 & 0 & 0 & 0 & 0 & \frac{1}{G_{12}} \end{bmatrix} \begin{Bmatrix} \sigma_1 \\ \sigma_2 \\ \sigma_3 \\ \tau_{23} \\ \tau_{13} \\ \tau_{12} \end{Bmatrix} \tag{1.16}$$

1.2 Theories of structure

In reality, each structural problem is a three-dimensional solid; in structural mechanics, talking about solids means referring to structural problems in which the three dimensions through x, y and z have the same dimension and none of them is negligible and, so for that reason, the displacements field depends on the three coordinates (as seen before: $\mathbf{u} = \mathbf{u}(x, y, z)$). The displacements $\mathbf{u}$ of any point of the body can be written as:

$$\mathbf{u}(x, y, z) = \Big\{u_x, u_y, u_z\Big\}^T \tag{1.17}$$

and, in fact, the functions $u_x(x, y, z)$, $u_y(x, y, z)$, $u_z(x, y, z)$ give the deformed state of the body[16][10].
In order to simplify the problems, we can make a variable, for example z, dependent on a function $F(z)$ and reduce, in this way, the problem from the 3D to the 2D field of study: the new displacements vector is $\mathbf{u} = F(z)\mathbf{u}(x, y)$. Another simplification is possible moving from a two-dimensional field to the 1D one, making displacements dependent no more on the only z by introducing a new function $F(x, y)$ which involves more than one unknown: the displacements vector becomes now $\mathbf{u} = F(x, y)\mathbf{u}(z)$.
The one-dimensional theories are interesting principally because of their simplicity and the low computational cost if compared to 2D (plates and shells) or 3D models (solids).
Typical one-dimensional structures of structural models are beams (fig. 1.1) in which two dimensions (the section ones) are negligible if compared to that one through the longitudinal axis.

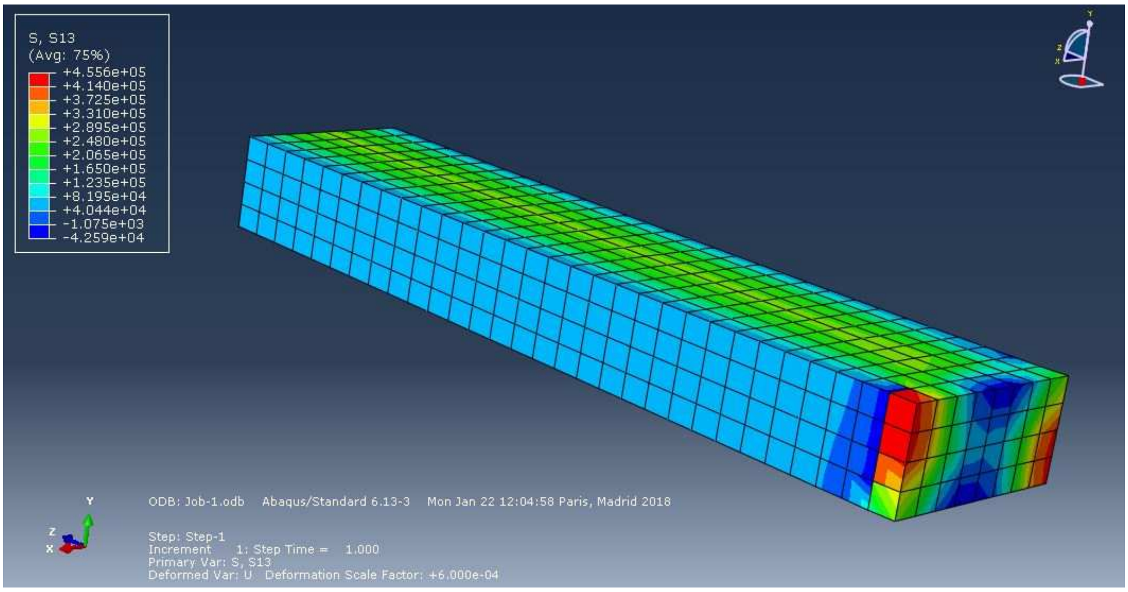

ODB: Job-1.odb Abaqus/Standard 6.13-3 Mon Jan 22 12:04:58 Paris, Madrid 2018

Step: Step-1
Increment 1: Step Time = 1.000
Primary Var: S, S13
Deformed Var: U Deformation Scale Factor: +6.000e-04

Figure 1.1: Clutch beam analysed with ABAQUS software.

In this case, since the dimension of the length l is predominant, the displacements field is:

$$\mathbf{u} = F(x,y)\mathbf{u}(z) \tag{1.18}$$

Different beam theories are used both to describe the behaviour of structures before making more complex analysis (as in FEM method) and to validate exact solution obtained through computational models. Those theories offer high accuracy levels and, among the simplest, the most used and common there are:

- the *Eulero-Bernoulli's Theory* (Euler-Bernoulli Beam Theory, EBBT): the complete three-dimensional displacements field is expressed by a function of the section displacements $U_x(x)$, $U_y(x)$, $U_z(x)$ and by their derivatives through the face from which the longitudinal x-axis comes out: the unknown displacements depend only from the x-coordinate
- Timoshenko's Theory: EBBT's development and further refinement, it is based on the shear deformations and on rotational inertia effects and it is usually applied to short beams, beams made by composites (sandwich) or beams subjected to excitation at high frequencies; Timoshenko's model converges to EBBT's classical one when the shear coefficient $G \to \infty$ (i.e. when the beam becomes infinitely stiff) or when inertia effect are negligible

EBBT's model is defined the *engineer's classical beam theory* or the *classical beam theory* because it calculates very simply the mechanical load and the subsequent deflections of the beam. An high order theory developed from EBBT is the *Sandwich Theory*: it's fundamental in the analysis of vehicle or aerospace structures that, for functional necessities, are made by composites layers.

1.3 1D models: Classical Beam Theories

The theory of structural mechanics which describes beam characteristics, called *Beam Theory*, is fundamental in structural analysis because is able to model every component (both parts of machines and aerospace structures such as wings or the fuselage) in a very simple way, using the thin-walled beam.
Stress characteristics represent the resulting force F and the resulting moment M deriving from the internal forces which act on the beam section. The resulting force F is locally decomposed in two components: the first is N called *Normal Force* and it is the component which is perpendicular to the beam section, the latter is T called *Shear Force* and it is the component which is parallel to the beam section; the normal component M_t of the resulting moment M, which represents the torque acting in the section plane, is called *Twist Torque* while M_f is called *Bending Moment* and it's the component acting in a plane which is orthogonal to the beam section.
External forces are applied to the axis[54] and, so, different forces and moments can be described: $f(s)$ and $m(s)$ are respectively the distributed forces and moments per unit

length, F_0 and F_l are the concentrated forces acting in the extremities (respectively in abscissa $s = 0$ and $s = l$), M_0 and M_l are the concentrated moments acting in the extremities (respectively in abscissa $s = 0$ and $s = l$), F_i and M_i are respectively the concentrated forces and moments acting in the internal points of the axis line, f_v and p_v are respectively the volume forces and surface forces (fig. 1.2).

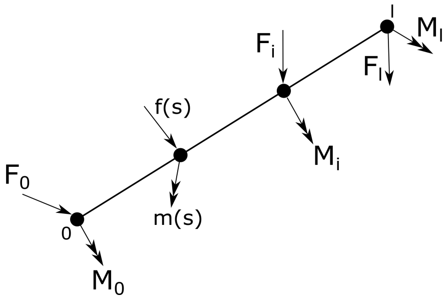

Figure 1.2: Forces and moments acting on axis.

The *Indefinite equations of equilibrium* can be drawn by the study of forces and moments and they represent the equilibrium of a section not subjected to concentrated forces. Those equations, for huge displacements, depend on the bending of the deformed axis because the deformed beam axis is curved, while the informed one is straight; for little displacements, the deformed beam axis can be assumed the same as the informed axis and, in this way, the indefinite equations of equilibrium represent the equilibrium of a rigid beam. The first order equilibrium equations will be formed by the 3 equilibrium in-plane equations (two about translation and one about rotation) of an infinitive beam length dz, neglecting the infinitesimal of higher order than the first one (fig. 1.3).

$$\begin{cases} \frac{dN}{dz} + p = 0 \\ \\ \frac{dT}{dz} + q = 0 \\ \\ \frac{dM}{dz} + m - T = 0 \end{cases}$$

Generally, the indefinite equations of equilibrium are called *Navier's equations* and they are a function of displacements; Navier's theory[48, page 1275] [8, page 16] has not the aim to determine the load that causes the break of the element, but the load which can be applied on the element within leaving any permanent deformations and, for this reason, those equations fall in the theory of elasticity which is subdivised in two principal analysis method: the first is based on displacements formulation (*Navier-Cauchy's equations*) and the latter is based on stress formulations (*Beltrami-Mitchell's equations*).

The Navier-Cauchy's equations allows to solve static-elastic problems having only the displacements as the problem's unknowns, neglecting both deformations and stresses; from the kinematic and constitutive second order equations, three scalar equations with only displacements unknown can be written, making explicit the shear tensor T and the external

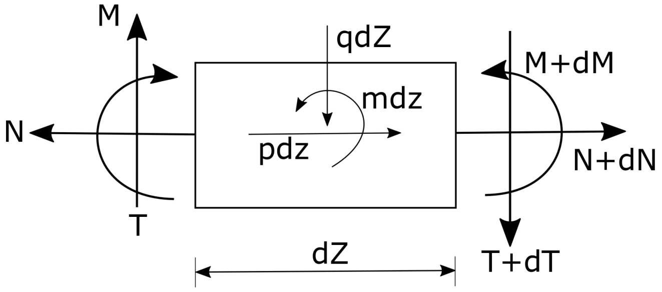

Figure 1.3: Equilibrium equations of a beam long dz.

forces vector. The Beltrami-Mitchell's equations, instead, allows a stress variables problem formulation and it can be written in the static case: deformations and displacements are neglected from the formulation and only stresses are considered as problem's unknowns; deformations are calculated simply with the constitutive equation $\sigma = \mathrm{E}\ \varepsilon$.

1.3.1 Euler-Bernoulli's Model

Let consider a infinite length isotropic beam and be $u_x(x,y,z)$, $u_y(x,y,z)$, $u_z(x,y,z)$ the displacements of any point of the beam in the three directions x, y, z; Euler-Bernoulli's Model is based on three kinematic hypothesis:

- beam cross-section is infinitely stiff in its plane, i.e. in-plane deformations don't exist. This hypothesis means that the displacements field in the plane of the beam cross-section consists only in the two rigid body translations $U_y(x)$ e $U_z(x)$:

$$u_y(x,y,z) = U_y(x) \tag{1.19}$$

$$u_z(x,y,z) = U_z(x) \tag{1.20}$$

- during deformation, the cross-section remains plane, i.e. the displacements axial field consists in a rigid body translation $U_x(x)$ and two rigid body rotations $\Phi_y(x)$ and $\Phi_z(x)$ and it will be, thus, an axial beam deformation (considering the sign convention: rigid body positive translations if concordant with x, y, z; rigid body positive rotations if around y and z):

$$u_x(x,y,z) = U_x(x) + z\Phi_y(x) - y\Phi_z(x) \tag{1.21}$$

- during deformation, the cross-section remains perpendicular to the deformed beam axis: the rotation of the beam section and the inclination angle of the beam have the same value (fig. 1.4)

Finally, the axial beam deformation on the cross-section can be written in the following way:

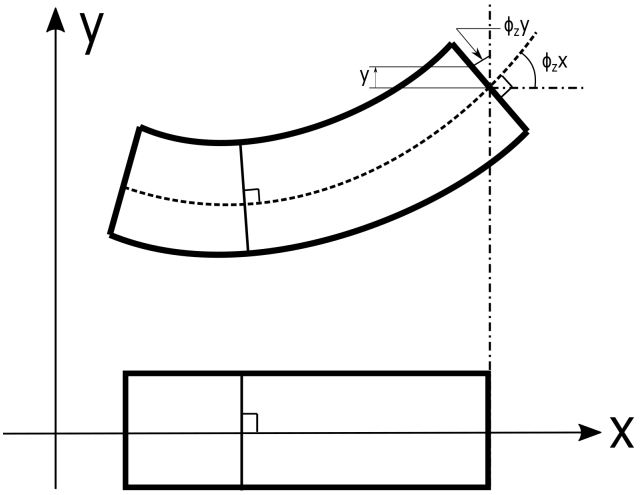

Figure 1.4: Deformed and informed configuration of a generic Euler-Bernoulli's beam.

$$\varepsilon_x(x,y,z) = \Sigma_x(x) - zK_y(x) - yK_z(x) \tag{1.22}$$

where Σ is the axial deformation of the section equal to the first derivative *U’x(x)*, $K_y(x)$ is the section bending around y equal to the second derivative *U”z(x)* and $K_z(x)$ is the section bending around z equal to the second derivative *U”y(x)*.
From the first hypothesis of Euler-Bernoulli's theory, the deformation field in the section plane disappears; from the second equation, the shear deformation field disappears; from the third one, the axial deformation distribution becomes linear. The limit of this theory is the purely kinematic hypothesis on which it states and in particular on the second hypothesis which assumes that section remains plane after deformation and that plane remains perpendicular to the deformed beam axis; this hypothesis involves that angular deformations disappear on the whole section and if the constitutive law $\tau = \mathrm{G}\gamma$ is used (where τ is the shear stress measured in [MPa], G is the shear modulus and γ is the shear deformation equal to the fraction between longitudinal displacements due to the shear force applied on the side of the specimen and the informed length of the side itself), a contradiction will appear: called $F_y(x)$ and $F_z(x)$ the shear forces respectively in y-direction and z-direction, the formulation will be:

$$F_y(x) = \int_A \tau_{xy}(x,y,z)dA = 0 \tag{1.23}$$

$$F_z(x) = \int_A \tau_{xz}(x,y,z)dA = 0 \tag{1.24}$$

(A is the infinitesimal area on which the shear force acts), thus the shear forces and relating γ will be equal to zero and the shear stress, in this way, will be neglected: therefore, the shear distribution along the section can't be uniform as it was supposed at the beginning. To overcome that contradiction, Timoshenko introduced a new theory which, in contrast to Euler-Bernoulli's model, doesn't neglect the shear influence on the beam.

1.3.2 Timoshenko's Model

The kinematic hypothesis of Timoshenko's model [47] states that, even if the sections remain plane, the squareness between the elastic line and the beam section disappears; in the quasi-static case[1], inertial effects are supposed to be negligible. Therefore, the displacements of a generic point of the beam can be expressed as:

$$u(x,z) = u_0(x) + \varphi(x)z \tag{1.25}$$

$$w(x,z) = w_0(x) \tag{1.26}$$

here $u_0(x)$ and $w_0(x)$ are the displacements of the centre of gravity of the section and $\varphi(x)$ is the rotation of the section around the vertical axis (fig. 1.5).

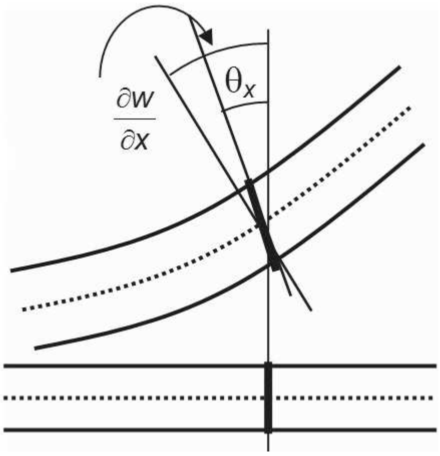

Figure 1.5: Timoshenko's beam deformation. The angle of rotation is $\theta_x = \varphi(x)$, which is not equal to the displacement variation $\frac{\partial w}{\partial x}$.

The Timoshenko's model for a quasi-static case is the same described by Euler-Bernoulli's model if the displacement $\frac{\partial w}{\partial x}$ is negligible, i.e. if this approximated relation is true:

$$\frac{EI}{\kappa L^2 AG} \ll 1 \tag{1.27}$$

where L is the length of the beam, A is the cross-section, E is the Young's modulus, G is the shear modulus, I is the Moment of inertia of plane area[2] and κ is the Timoshenko's

---

[1] A *quasi-static transformation* is a transformation which takes place in an extremely slow way, so that the system, changing from an initial state of equilibrium to a final equilibrium state, passes through infinite equilibrium states, separated each other both by infinitesimal transformations and by infinitesimal properties variations of the system. The word *quasi-static* is preferable to the *static* one because real systems are considered in which forces don't stop instantly their actions, but they still act on the system for an infinitesimal time.

[2] The Moment of inertia of plane area is the geometric property of an area which refers to the distribution of its points in respect of a reference axis.

coefficient depending on beam geometry (κ is almost 5/6 for a rectangular cross section beam).
The boundary conditions which allows to apply Timoshenko's model to a quasi-static case are two and they are true for two different situations:

- *Beam sustained by two ties*: the displacement w is zero in the point when the two ties act, the bending moment M_{xx} can be calculated, while the rotation φ and the shear force F_x are not defined, but they have to be supposed or obtained by *FEM* analysis on the whole beam length
- *Clamped beam*: the displacement w and rotation φ in the point on which the bond acts are zero; if the other extremity isn't bonded at all, the bending moment M_{xx} and the shear force F_x can be calculated

1.4 2D Plane Stress Theory

In the finite element method, a plate loaded in its midplane (which lies halfway between the two faces of the plate) is said to be in a state of *plane stress*, or a *membrane state*, if the following assumptions hold[33]:

- All loads applied to the plate act in the midplane direction and are symmetric to the midplane
- All support conditions are symmetric to the midplane
- In-plane displacements, strains and stresses can be taken to be uniform through the thickness
- The normal and shear stress components in the z direction are zero or negligible (σ_{zz}, σ_{xz}, σ_{yz})
- The plate is transversely homogeneous

The thickness h of the plate should be small, typically 10% or less than the shortest in-plane dimension of the plate itself; if the fourth hypothesis is not true, i.e if z-stresses are accepted, the behaviour of the plate will be the so-called *generalized plane stress state* in which $\varepsilon_z = cost$, thus the strain through the thickness is constant: the *plane strain state* is obtained if strains in the z-direction are precluded.
The mathematical model of a plate in plane stress is set up as a two-dimensional boundary value problem (BVP), in which the plate is projected onto its midplane and this allows to formulate the BVP over a plane domain Ω with a boundary Γ (fig. 1.6)[33]. In this way, the third dimension is represented as functions of x and y that are integrated through the plate thickness z: most plates used as structural components have constant thickness, but if the thickness changes (in these cases the formulation for thickness will be $h = h(x, y)$, so depending on x- and y-coordinates), to maintain the plane stress state, the variation of h should be gradually because sudden changes in thickness may lead to stress concentrations.

Forces can be assumed acting in the interior Ω of the plate; two types of forces can act: the body forces (or volume forces) are forces per unit of plate volume, such as the weight of the plate; face forces, instead, act tangentially to the plate faces and they are referred to the midplane, such as friction and it's fundamental knowing if these forces are specified per unit of surface area or per unit length. Let assume that the plate material is linearly elastic: the unknown fields are displacements, strains and stresses.
The in-plane displacement field is defined by two components:

$$\mathbf{u}(x,y) = \begin{bmatrix} u_x(x,y) \\ u_y(x,y) \end{bmatrix} \tag{1.28}$$

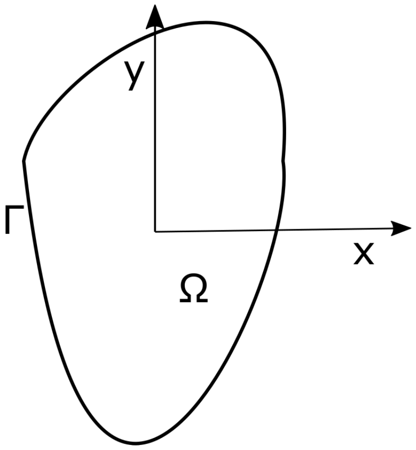

Figure 1.6: A plate structure in plane stress: 2D mathematical idealization as boundary value problem.

The transverse displacement component $u_z(x,y,z)$ (which depends on z) is generally not negligible because of Poisson's ratio effects.
The in-plane strain field forms a tensor defined by three independent components:

$$\varepsilon(x,y) = \begin{bmatrix} \varepsilon_{xx}(x,y) \\ \varepsilon_{yy}(x,y) \\ \gamma_{xy}(x,y) \end{bmatrix} \tag{1.29}$$

In this formulation, ε_{xz} and ε_{yz} are negligible, instead the normal strain ε_{zz} is generally not negligible because of Poisson's ratio effects although it will not appear in the governing equations because the associated stress σ_{zz} is zero.
The in-plane stress field forms a tensor defined by three independent components: σ_{xx} , σ_{yy} and σ_{xy}. As in the previous case of strains, these three components are cast to form a stress vector:

$$\sigma(x,y) = \begin{bmatrix} \sigma_{xx}(x,y) \\ \sigma_{yy}(x,y) \\ \tau_{xy}(x,y) \end{bmatrix} \tag{1.30}$$

and the remaining stresses σ_{zz}, σ_{xz} and σ_{yz} can be negligible.
Ignoring the initial strain effects ε_0 and using the Hooke's law and Young's Modulus, stresses have this mathematical formulation:

$$\sigma = \begin{Bmatrix} \sigma_{xx} \\ \sigma_{yy} \\ \tau_{xy} \end{Bmatrix} = \mathbf{C} \begin{Bmatrix} \varepsilon_{xx} \\ \varepsilon_{yy} \\ \gamma_{xy} \end{Bmatrix} \tag{1.31}$$

where $\mathbf{C}$ is the *Elasticity Matrix* and, so, it is possible to extract the strain formulation as follows:

$$\varepsilon = \mathbf{C}^{-1}\sigma \tag{1.32}$$

and impose the condition of plane stress.
The plate internal forces can be obtained integrating stresses components through the thickness and, if an uniform stress distribution is considered, the forces can be written as follows:

$$p_{xx} = \ \sigma_{xx}\ hp_{yy} = \ \sigma_{yy}\ hp_{xy} = \ \sigma_{xy}\ h \tag{1.33}$$

1.4.1 Governing equations

The three internal fields shown before (displacements $\mathbf{u}$, strains ε and stresses σ) are connected by three field equations: kinematic, constitutive and internal-equilibrium equations[33][14].

1.4.1.1 Strain

If initial strain effects ε_0 are ignored, the total strain at any point within the element can be defined by its three components which contribute to internal work; thus:

$$\begin{bmatrix} \varepsilon_{xx} \\ \varepsilon_{yy} \\ \gamma_{xy} \end{bmatrix} = \begin{bmatrix} \frac{\partial}{\partial x} & 0 \\ 0 & \frac{\partial}{\partial y} \\ \frac{\partial}{\partial y} & \frac{\partial}{\partial x} \end{bmatrix} \begin{bmatrix} u_x \\ u_y \end{bmatrix} = \mathbf{Du} \tag{1.34}$$

where $\mathbf{D}$ is the matrix with partial derivative operators and considering both the displacement of a node having two component:

$$a_i = \begin{Bmatrix} u_i \\ v_i \end{Bmatrix} \tag{1.35}$$

and the six components of element displacements:

$$a_e = \begin{Bmatrix} a_i \\ a_j \\ a_m \end{Bmatrix} \tag{1.36}$$

we obtain, by substituting:

$$\varepsilon = \mathbf{B}a_e = [B_i, B_j, B_m] \begin{Bmatrix} a_i \\ a_j \\ a_m \end{Bmatrix} \tag{1.37}$$

where the matrix **B** is given by:

$$\mathbf{B} = \mathbf{D}N_i = \begin{bmatrix} \frac{\partial N_i}{\partial x} & 0 \\ 0 & \frac{\partial N_i}{\partial y} \\ \frac{\partial N_i}{\partial y} & \frac{\partial N_i}{\partial x} \end{bmatrix} \tag{1.38}$$

in which N_i are the displacement functions which automatically guarantees continuity of displacements with adjacent elements because the displacements vary linearly along any side of the geometry and, if the same displacement is imposed at the nodes, the same displacement will exist all along the interface of the plate.

1.4.1.2 Elasticity matrix - isotropic material

By definition[33][14], for plane stress in an isotropic material we have:

$$\varepsilon_{xx} = \frac{\sigma_{xx}}{E} - \frac{\nu\sigma_{yy}}{E} \tag{1.39}$$

$$\varepsilon_{yy} = -\frac{\nu\sigma_{xx}}{E} + \frac{\sigma_{yy}}{E} \tag{1.40}$$

$$\gamma_{xy} = \frac{2(1+\nu)\tau_{xy}}{E} \tag{1.41}$$

and we can obtain the *Reduced Stiffness Matrix* **Q** as follows:

$$\mathbf{Q} = \frac{E}{1-\nu^2} \begin{bmatrix} 1 & \nu & 0 \\ \nu & 1 & 0 \\ 0 & 0 & (1-\nu)/2 \end{bmatrix} \tag{1.42}$$

in which E is the elastic modulus and ν is Poisson's ratio and considering

$$G = \frac{E}{2(1+\nu)} \tag{1.43}$$

1.4.1.3 Elasticity matrix - anisotropic material

As seen in section 1.1, in order to completely describe the three-dimensional mathematical relationships between stress and strains in an anisotropic material, 21 independent elastic constants are necessary[33]. Let not consider a three-, but a two-dimensional analysis: a symmetry of properties is now possible and only six independent constants can be written in the **Q** matrix:

$$\mathbf{Q} = \begin{bmatrix} d_{11} & d_{12} & d_{13} \\ & d_{22} & d_{23} \\ & & d_{33} \end{bmatrix} \tag{1.44}$$

A transversely stratified isotropic material, whose rotational symmetry of properties exists within the plane of the layers, possesses only five independent elastic constants and the general mathematical relationships between stress and strains are:

$$\varepsilon_{xx} = \frac{\sigma_{xx}}{E_1} - \frac{\nu_2 \sigma_{yy}}{E_2} - \frac{\nu_1 \sigma_{zz}}{E_1} \tag{1.45}$$

$$\varepsilon_{yy} = -\frac{\nu_2 \sigma_{xx}}{E_2} + \frac{\sigma_{yy}}{E_2} - \frac{\nu_2 \sigma_{zz}}{E_2} \tag{1.46}$$

$$\varepsilon_{zz} = -\frac{\nu_1 \sigma_{xx}}{E_1} - \frac{\nu_2 \sigma_{yy}}{E_2} + \frac{\sigma_{zz}}{E_1} \tag{1.47}$$

$$\gamma_{xz} = \frac{2(1+\nu_1)}{E_1} \tau_{xz} \tag{1.48}$$

$$\gamma_{xy} = \frac{1}{G_2} \tau_{xy} \tag{1.49}$$

$$\gamma_{yz} = \frac{1}{G_2} \tau_{yz} \tag{1.50}$$

in which the constants E_1 and ν_1 (from which G_1 depends on) are linked to the behaviour of each layer and E_2, ν_2 and G_2 are linked to the behaviour of a direction normal to the plane. The **Q** matrix in two dimensions, considering generally $E_1/E_2 = n$ and $G_2/E_2 = m$, becomes:

$$\mathbf{Q} = \frac{E_2}{1 - n\nu_2^2} \begin{bmatrix} n & n\nu_2 & 0 \\ n\nu_2 & 1 & 0 \\ 0 & 0 & m(1-\nu_2^2) \end{bmatrix} \tag{1.51}$$

To compute rotation of the layers in the matrix, the *Transformation Matrix* **T** should be introduced: this matrix relates stresses and strains (**C**') in the inclined coordinate system, obtaining the **C** matrix in the universal system of coordinates (fig. 1.7):

$$Q = TQ'T^T \tag{1.52}$$

where

$$T = \begin{bmatrix} cos^2\theta & sin^2\theta & -2sin\theta cos\theta \\ sin^2\theta & cos^2\theta & 2sin\theta cos\theta \\ sin\theta cos\theta & -sin\theta cos\theta & cos^2\theta - sin^2\theta \end{bmatrix} \tag{1.53}$$

Now, stresses and strains can be written as:

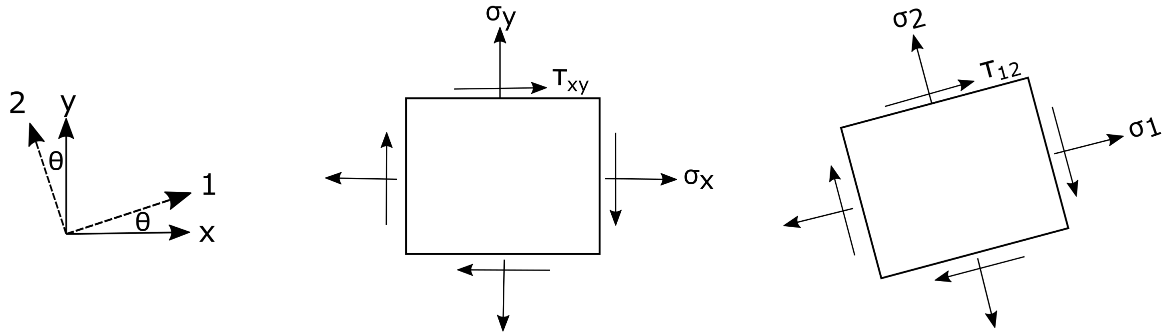

Figure 1.7: Rotation of axes.

$$\sigma'^T\varepsilon' = \sigma^T\varepsilon \tag{1.54}$$

$$\varepsilon'^T Q'\varepsilon' = \varepsilon^T Q\varepsilon \tag{1.55}$$

1.4.2 Boundary conditions

Typical loading and boundary conditions for plane stress problems are forces or distributed forces[17] applied over the thickness of the plate and the supports can be fixed points or fixed edges or roller supports.
The displacement boundary conditions are:

$$u = \hat{u} \tag{1.56}$$

where $\hat{u}$ are prescribed displacement and it is often negligible in fixed portions of the boundary. Instead, force boundary conditions (also called BCs and traction BCs in the literature) can be expressed in the form:

$$\sigma = \hat{t} \tag{1.57}$$

where $\hat{t}$ are the surface tractions specified per unit area.

Chapter 2

An overview on adhesive bonded joints

Adhesive bonded joints represent an increasingly accepted alternative to mechanical joints in engineering applications and provide many advantages over conventional mechanical fasteners. With the development of industries, aluminium became the principal structural material and riveting the most used technique, but from 70s, during which the aerospace engineering (fig. 2.1) had to face the request of better performances, less consumes and better cost-effectiveness, the bonding solution went back on favour in military and civil field.

Continuous junction techniques (welding and bonding) are better than discontinuous ones (riveting and bolting) to match ductile or fragile, isotropic or anisotropic materials, especially for composite materials which are made by several layers bonding one upon the other one. Even more, mechanical joints require a preliminary drilling and, so, a little destruction of the elements to be joined (for example, in composite materials, interruption of the fibres), that for sure cause localized material damage and stress concentration, especially for anisotropic laminates characterized by high stress concentration factors and easy drilling damaging, with significant decrease of the load-carrying capacity of the joined elements. These situations are even more demanding for advanced composites structures because they are brittle and lack of ductility to redistribute loads.

To overcome this limit, hybrid joints, obtained by the superposition of a mechanical joint to a simple adhesively bonded joint, are more and more used in engineering features: adhesively bonded joints are characterized by high stiffness and good fatigue life, even if delamination phenomena localized mostly near the free edges may limit their use, especially for applications where corrosive environments and moisture can lead to premature failure of the bonding, as in aerospace engineering[31].

The use of bonded joints permits to obtain components characterized by good stiffness, lightweight, good static and fatigue strength, thanks especially to the absence of significant notch effects on the components to be joined together[29]. It is possible to compare mechanical bonded and adhesively bonded joint's characteristics with simple experimental tests[21] (fig. 2.2 and fig. 2.3): the tensile strength and the damage mechanisms under

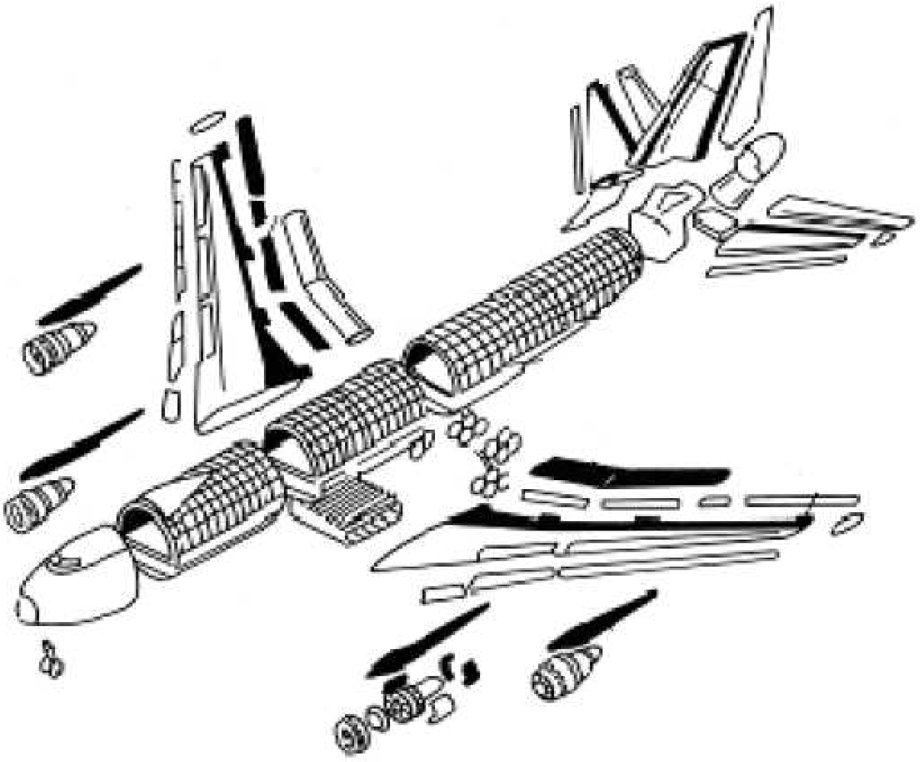

Figure 2.1: Modern aircraft: in black the bonded parts.

static stress are determined by tensile tests performed by using a MTS 810 servo-hydraulic testing machine on two specimens and, according to ASTM standard[6], all the experimental tests have been carried out under a constant crosshead speed of 1 mm/min: the adhesively bonded joint shows a linear behavior until failure and, analyzing the corresponding fracture surface, it's evident that the failure of the joint is caused by the adhesive failure (which propagates from the attach edge of the more compliant adherent) at the interface with the aluminum alloy adherend. The mechanical riveted specimen, with aluminum and steel rivets, initially exhibits a linear behaviour, followed by a successive elasto-plastic phase, then a final phase characterized by a load decrease, up to the complete failure of the joint which continues until the end of the test.

Both the specimens (that one made by aluminium adhesive and that one with steel rivets) exhibit the same stiffness in the elastic and elasto-plastic phases, but the loads of the linearity deviation are different (about 3 kN and 6 kN for the first and the latter, respectively) and also the tensile strengths are different (about 5 kN for the first specimen with aluminum and 8.5 kN for mechanical bonded one). The linearity deviation corresponds to the transition from the initial condition of friction due to the preload of the rivet to the secondary condition in which part of the load is transmitted through shear stresses on the rivets: it's evident that the specimens with steel rivets exhibit a failure load of about 70% higher than that of the specimens adhesives; instead, no significant damage of the adhesively aluminum joint, is observed.

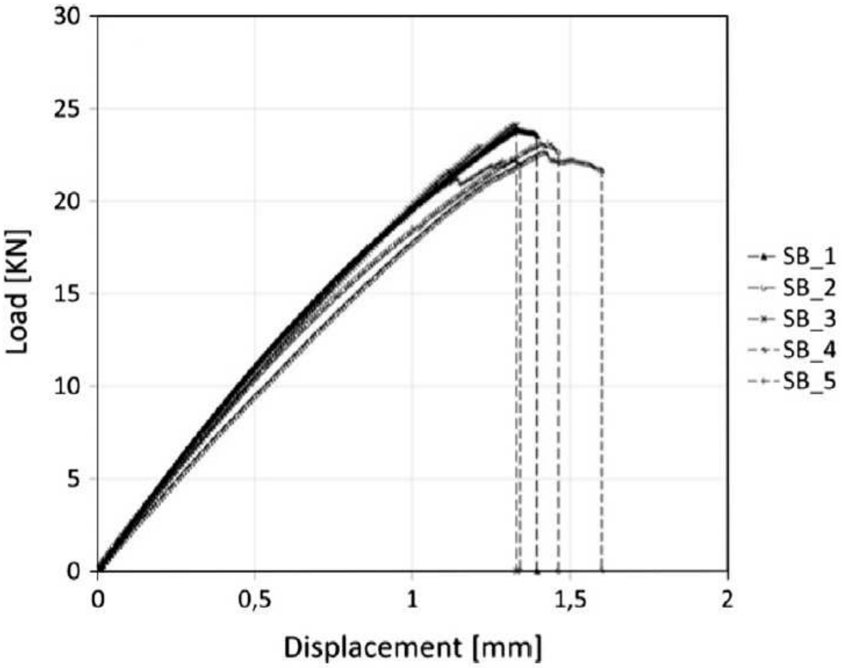

Figure 2.2: Tensile stress results for different simply adhesive bonded joints (SB)[21].

In reality, discontinuous mechanical junctions are still used in engineering because of the influence that environment features have on adhesives, their difficulties to be inspected and checked, although continuous joints guarantee better structural efficiency, lower weight, thermal and electrical insulation and better aerodynamics. In summary, the main advantages of a bonding junction are the more uniform distribution of stresses, if compared to mechanical joints, because:

- no drillings are used and this leads to a reduction of stresses concentrations
- jointing forces are distributed uniformly on the surface
- the surface in which there is the juncture is quite huge and this implies a great capacity of spreading loads
- bonding techniques does not modify neither chemical composition nor structure of adherends and they can joint both very thin and very thick adherends or totally different materials
- bonding techniques gives thermal and electrical insulation and they damp the vibrations
- fatigue behaviour and damage tolerance are increased

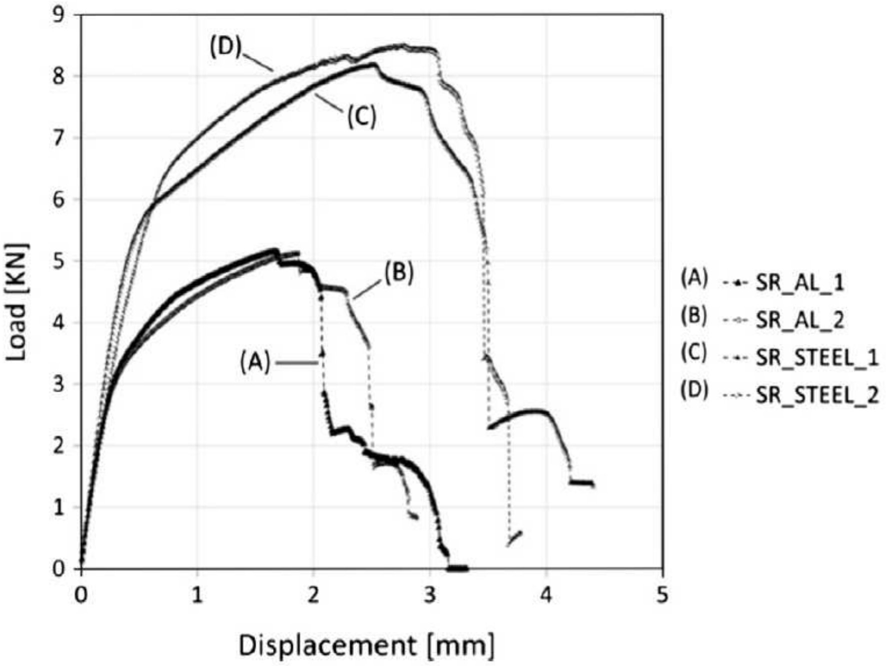

Figure 2.3: Tensile stress results for different simply riveted joints (SR)[21] with aluminium or steel adherends.

- low cost

On the contrary, bonding joints have some disadvantages:

- great deformation mostly from peeling stress than traction or shear stress
- complex structural analysis for critical applications or with geometrical difficulties
- accurate preparation of parts before bonding
- no direct inspection; non-destructive controls have to be carried out
- repairing a joint is impossible
- the maximum operative temperature can be very low and it affects joint stiffness

2.1 Bonding Techniques

An adhesive is a chemical substance able to bond two other materials through superficial adherence[6] and the aim of structural bonding techniques is realizing joints with such a level of stiffness that they can be subjected to stress levels next to their failure values and, in this way, it is possible to take full use of mechanical performances of adherends, obtaining high efficiency joints.

In order to obtain the best performances from a bonded joint, some aspects have to be underlined, most of all the geometry of the joint: the crack stress of a bonded joint depends on mechanical characteristics of the materials which compose the joint itself, on the size of the adhesive zone, on load disposition and on internal stresses. The joint does not experience uniform distribution of stresses and the crack origins in correspondence of stresses peaks, although the crack stress is computed by dividing the crack force by the bonding surface. The stress peaks may be due to the differences in deformations between adherends and adhesive, different thermal expansion coefficient and the bending effects due to the thickness of the adherends, whose surfaces, jointly with adhesive's one, have to be prepared before the bonding phase: it's fundamental removing impurity and layers of oxides before which may interfere with the mechanical properties of the joint. Adhesives are an important part of the joint and the phases of production of a lap joint are:

- removing layers of oxides: the failures concentrate locally where oxide layers lean
- maximizing the contact between the adhesive and the two adherends, increasing the superficial roughness of the two parts
- guaranteeing the initial stiffness of the joint through an high level of adhesion forces, using pretreatment which increases the free energy of the adherends: in this way, adhesive and adherends have more energetic and stable interface chemical bonds
- protecting the surfaces of the adherends before the bonding operations, above all for metal adherends

Adhesives used in structural applications are summarized in fig. 2.4.

2.2 Analytical Methods for Single Lap Joints

The main approach which state at the basis of the design of adhesive joints is the stress analysis approach which is generally formulated on a maximum stress or maximum strain as a failure criterion and in fact the failures are assumed to occur when the maximum stress or strain at the end of the bonded overlap reaches a critical value. Stress analysis in the very thin adhesive layer are very complex because peel and shear stresses overlap on the structure and they are closely linked; in addition, the deformations of adherends, with respect to the adhesive and stress concentrations in the joint, can also produce large local stresses: it's now evident that it's complicated to determine the local stresses in the adhesive joints.

The classical geometry of a Single Lap Joint is shown in fig. 2.5, clamped on one side and loaded on the other: if the load is not applied on the centre of gravity (not eccentric load), a bending moment will be created and it will be sum to that moment caused by the deformation of the structure; this varying moment across x-axis creates that normal stress across y-axis called *Peel Stress* and the structure deforms qualitatively with the shape reported in fig. 2.6.

The value of the bending moment at the free edges overlaps between adherends and adhesive and can be used as boundary conditions for differential equations exposed in

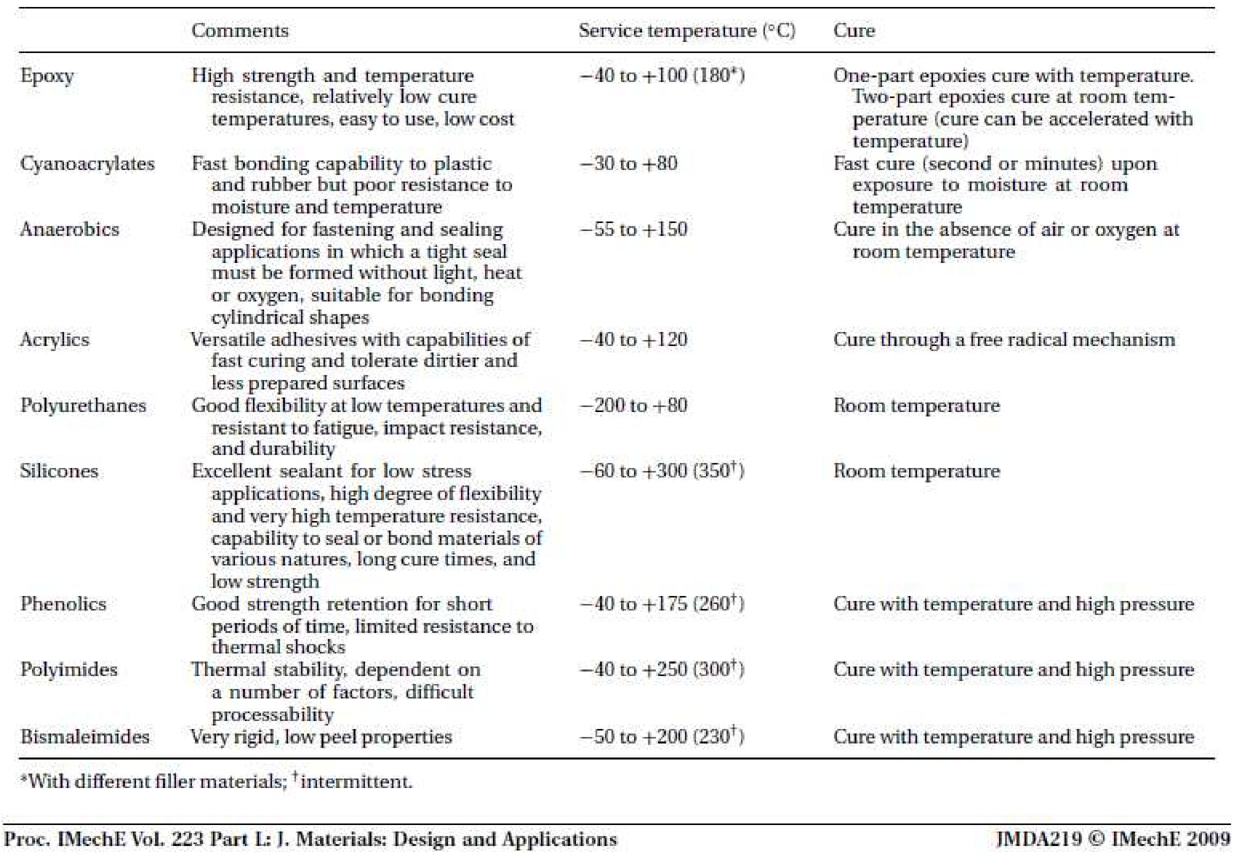

	Comments	Service temperature (°C)	Cure
Epoxy	High strength and temperature resistance, relatively low cure temperatures, easy to use, low cost	−40 to +100 (180*)	One-part epoxies cure with temperature. Two-part epoxies cure at room temperature (cure can be accelerated with temperature)
Cyanoacrylates	Fast bonding capability to plastic and rubber but poor resistance to moisture and temperature	−30 to +80	Fast cure (second or minutes) upon exposure to moisture at room temperature
Anaerobics	Designed for fastening and sealing applications in which a tight seal must be formed without light, heat or oxygen, suitable for bonding cylindrical shapes	−55 to +150	Cure in the absence of air or oxygen at room temperature
Acrylics	Versatile adhesives with capabilities of fast curing and tolerate dirtier and less prepared surfaces	−40 to +120	Cure through a free radical mechanism
Polyurethanes	Good flexibility at low temperatures and resistant to fatigue, impact resistance, and durability	−200 to +80	Room temperature
Silicones	Excellent sealant for low stress applications, high degree of flexibility and very high temperature resistance, capability to seal or bond materials of various natures, long cure times, and low strength	−60 to +300 (350†)	Room temperature
Phenolics	Good strength retention for short periods of time, limited resistance to thermal shocks	−40 to +175 (260†)	Cure with temperature and high pressure
Polyimides	Thermal stability, dependent on a number of factors, difficult processability	−40 to +250 (300†)	Cure with temperature and high pressure
Bismaleimides	Very rigid, low peel properties	−50 to +200 (230†)	Cure with temperature and high pressure

*With different filler materials; †intermittent.

Proc. IMechE Vol. 223 Part L: J. Materials: Design and Applications JMDA219 © IMechE 2009

Figure 2.4: Types of adhesives.

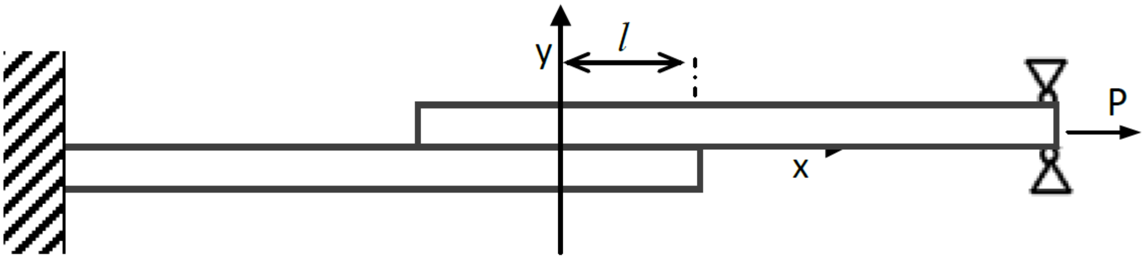

Figure 2.5: Literature representation of a classic Single Lap Joint used for analysis.

the previous sections to obtain the expression for peel stress and, then, the distribution of shear stress can be evaluated; therefore, following these steps, deformations in the adhesive layer can be analysed and, from them, considering the Young's Modulus E_a and Shear Modulus G_a of the adhesive, the values of peel and shear stress can be calculated.

One of the first analyses on bonded joints was done by Bikerman[7], who assumed linear elasticity of the adhesive and that both the flexible and rigid substrates behave as perfectly elastic materials; also the shear stresses were eliminated because the adhesive could be

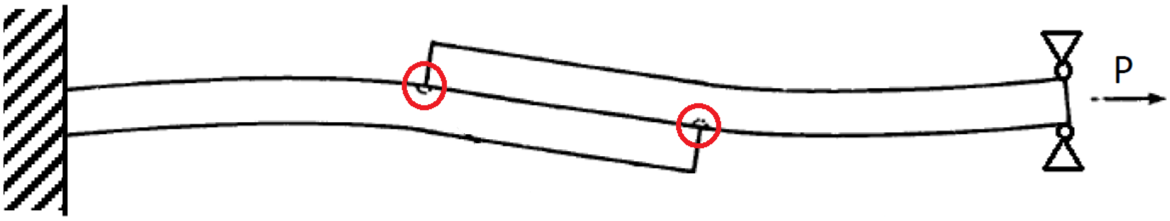

Figure 2.6: Maximum deformation areas on a Single Lap Joint (red spots).

modeled as individual fibres extending between substrates with no interdependence and his experiments leaded to the assumption that an adhesive with a low Young's modulus E should perform very well concerning the peel stress, but that low modulus may be the responsable of the performances decrease if the shear stress is calculated.

Volkersen[53] presented in 1938 a single lap joint whose main hypothesis was that the adherends are subjected only to a tension stress and the adhesive to a shear stress and both stresses (tension and shear stresses) are constant through the thickness. He studied the adhesive shear stress distribution along the bond line in the single lap joint loaded in tension by assuming that both the adherend and adhesive materials are elastic and, in this way, he was able to calculate the shear stress in terms of the differential stretching of the adherends: the shear stress is not uniformly distributed because of the stress concentration on the ends of the overlap area. Goland and Reissner[32] explored this type of joint considering, besides the shear stress, the effects of the adherend bending leading to peel stress in the adhesive layer; they were the first to take into account the bending of the adherends in the stress analysis of the single lap joint and they assumed a joint in a plane strain state and that the adherends and adhesives behave as elastic materials, presenting a full elastic analysis of the adhesive joint which calculates the adhesive shear and tensile stresses in the overlap region (fig. 2.7).

As expected, the most stressed zones are the overlapped free edges and the central zone is unloaded because the load is applied on the two adherends, with a little compression zone after the edge peak of peel stress: the value of this peak and the position of the compression depends on the elasticity and thickness of the materials. In this case the plot is symmetrical, but, if the thickness or stiffness of the two adherends change, stresses will be huger in the zone of the free edges: however, in every configuration, the stress concentration on the free edges is directly related to the geometrical discontinuity of the edge itself.

The Single Lap Joints with classical boundary conditions and loads described in this thesis takes direct inspiration from the study of M. Vable & J. Maddi[34] published on *"International Journal of Adhesion & Adhesive"*[1] and it has the following bonding, geometrical and physical characteristic (fig. 2.8, tab. 2.1) taken from [34, page 137]:

In [34] the *Boundary element method (BEM)* is used in which only the boundaries of each material are discretized, while in FEM the entire domain of the joint is discretized:

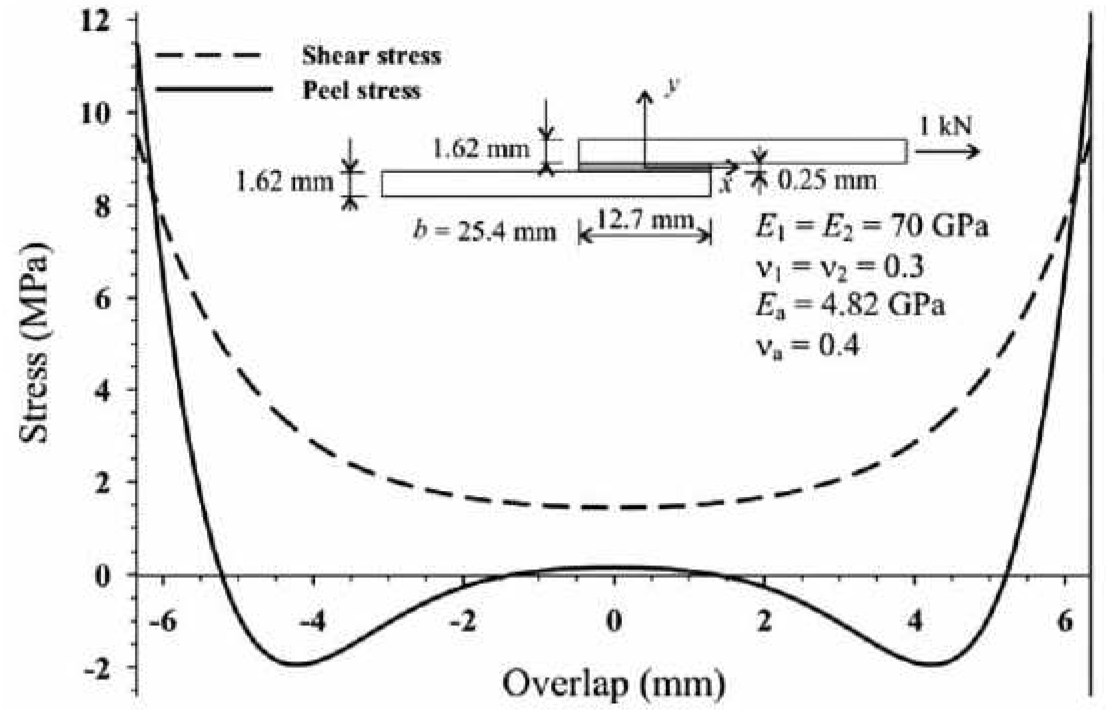

Figure 2.7: Goland and Reissner's adhesive shear and peel stress distributions for aluminium alloy adherends and an epoxy adhesive[32].

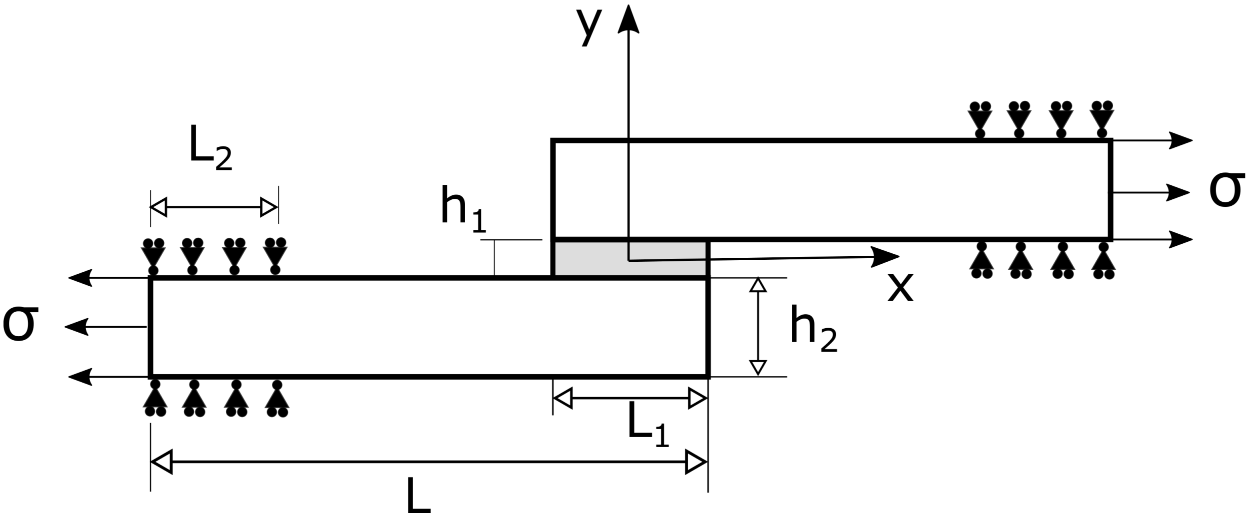

Figure 2.8: Single Lap Joint, Vable & Maddi.

the domain discretization poses more difficulties in finite element method, while in BEM the changes of boundary shape has little impact on modeling, even if the application of

Geometrical characteristics	**Value**
L_1	12.7 mm
L_2	12.7 mm
L	76.2 mm
h_1	0.15 mm
h_2	1.6 mm
$E_{Adhesive}$	3 GPa
$E_{Adherend}$	69 GPa
$\nu_{Adhesive}$	0.36
$\nu_{Adherend}$	0.32
σ	150 N

Table 2.1: Single Lap Joint, Vable & Maddi.

BEM to bonded joints is not simple because the formulation of BEM generates integral expressions for stresses and displacements, in which the integration is performed on the boundary of each material and, for that reason, BEM has many sources of error.
As it will be shown more precisely in the next chapters, the creation of graded mesh is better than no mesh gradation (fig. 2.9 and 2.10): determining the number of elements to use, the mesh gradation and the polynomial order of the interpolating functions, a mesh refinement scheme can minimize the errors. These results shown in [34] highlight the criticality of mesh gradation in regions of large stress gradients: small changes in the location of nodes of the structure have significant impact on the maximum value of stresses detected in regions of large stress gradients and, in fact, graded meshes have faster convergence (more accurate results with fewer degrees of freedom) than uniform meshes in the most stressed regions.
To keep the mesh nearly the same as those of Pickett & Hollaway (who provided studies that used non-linear analysis methods to evaluate composite bonded joint configurations[42]), Vable & Maddi employed an uniform and a graded 240 four noded quadrilateral elements; the graded mesh for the four noded elements in the bonded region for the adhesive and the adherends was produced by starting from the free edges of the bonded region and increasing the length of successive elements by a factor of 1.25. Vable & Maddi's results were obtained using the commercial finite element package $ABAQUS$[34].
Instead, Pickett & Hollaway, who studied a tubular lap joint (fig. 2.11) deriving from Robert Cook's[13] and Adams & Peppiatt's[44] works, employed two meshes:

- the square-edged solutions were obtained from a mesh of 92 8-node elements with a total of 343 nodes (fig. 2.12)

- the remainder of the solutions (lap and scarf joints with an adhesive fillet) were obtained using a mesh generation routine giving a mesh of 555 nodes and 164-8 node elements (fig. 2.13)

For comparison, graphical results for Adams & Peppiatt[1] (fig. 2.14, fig. 2.15) and Pickett & Hollaway (fig. 2.16, fig. 2.17) are shown

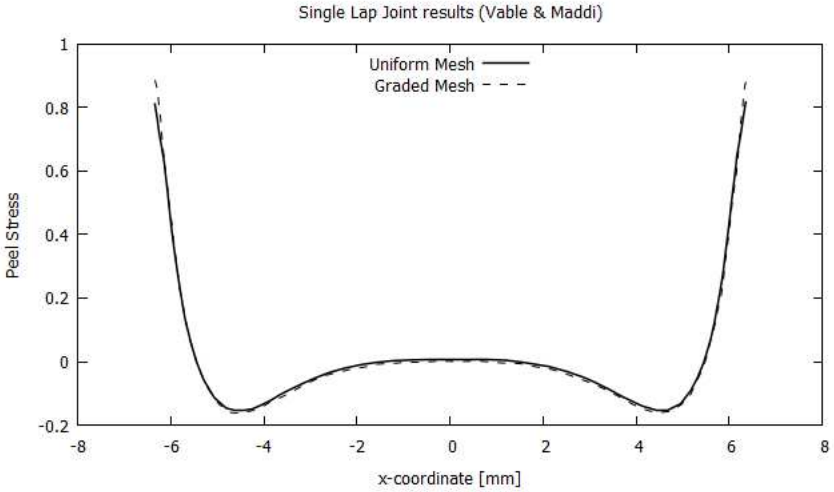

Figure 2.9: Single Lap Joint results for Peel Stress, Vable & Maddi.

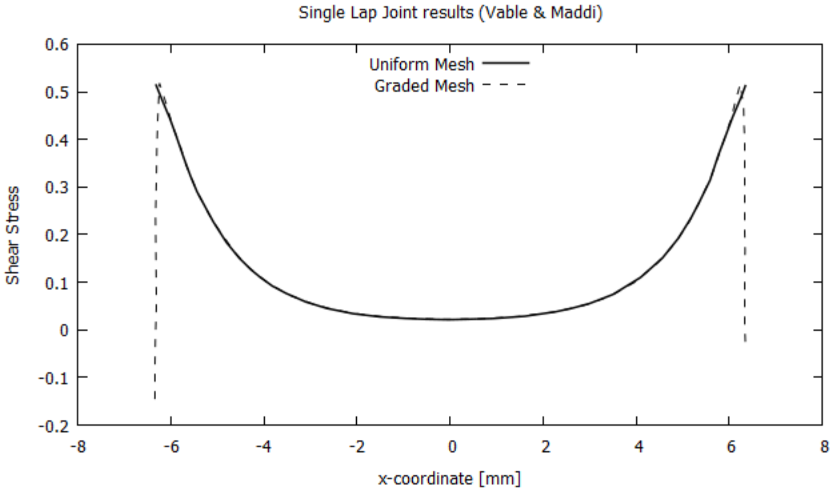

Figure 2.10: Single Lap Joint results for Shear Stress, Vable & Maddi.

---

[1] Lubkin and Reissner have analysed the stresses in tubular lap joints under a tensile axial load: their analytical method assumes that the adhesive can be approximated to an infinite number of tensile and shear springs and that the transversal stress in the adherends can be neglected in comparison with this stress in the adhesive[44].

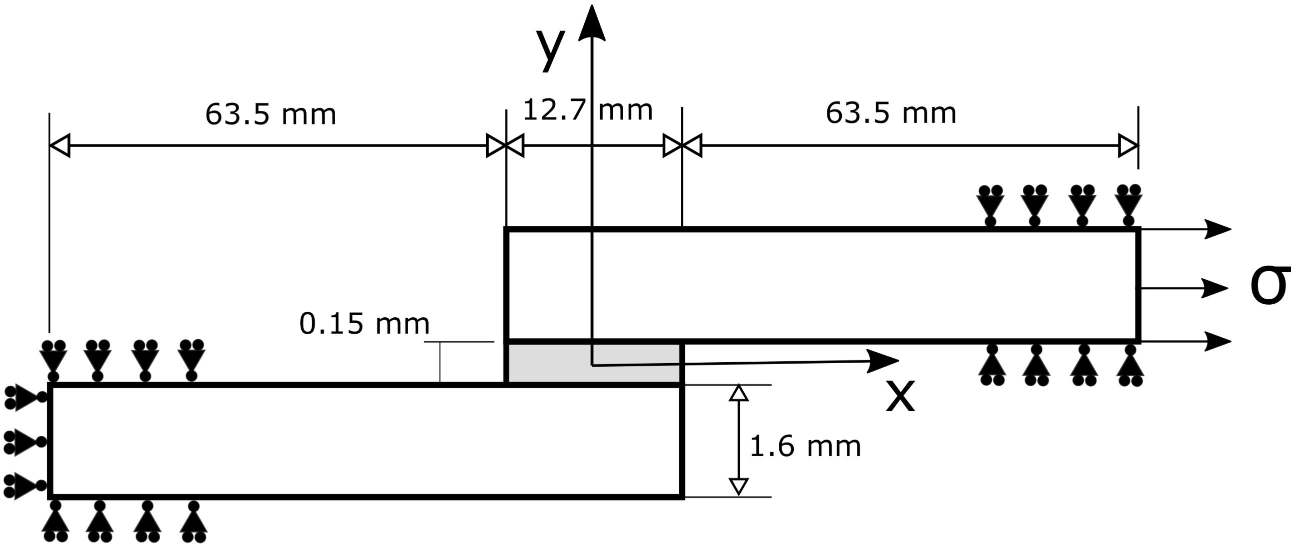

Figure 2.11: Single lap joint, Pickett & Hollaway.

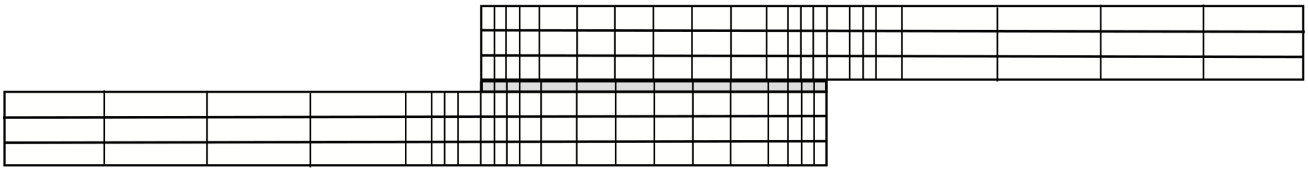

Figure 2.12: First finite element Mesh with 92 8-node elements, Pickett & Hollaway.

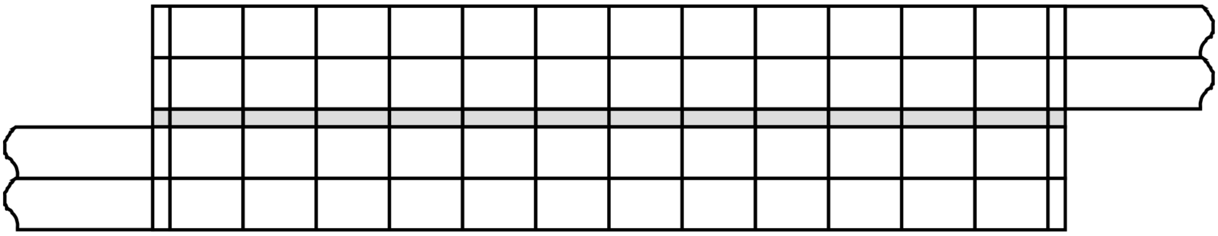

Figure 2.13: Second finite element mesh used for the overlap region with 164-8 node elements, Pickett & Hollaway.

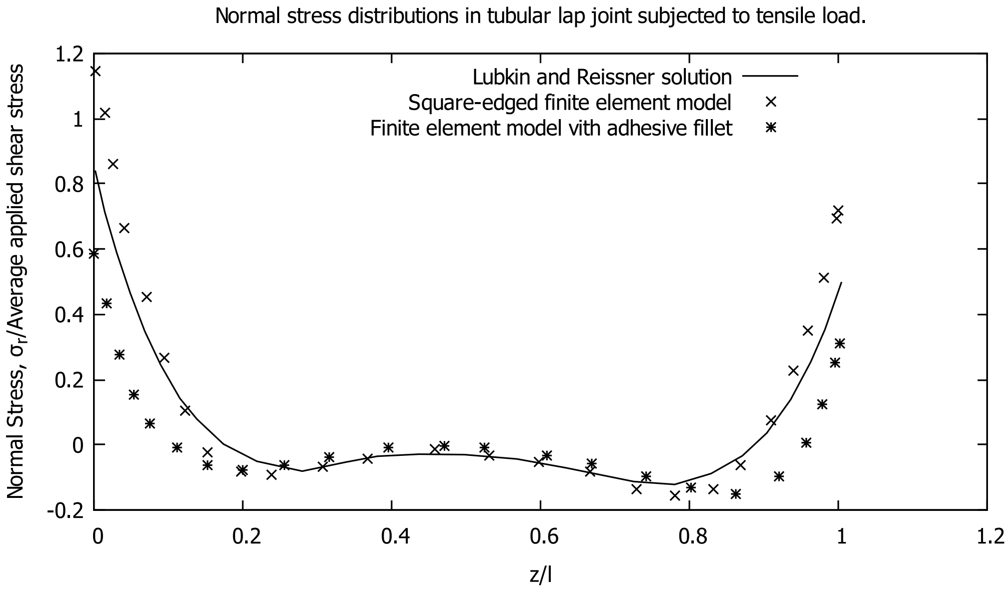

Figure 2.14: Peel stress distributions in tubular lap and scarf joints subjected to tensile load, Adams & Peppiatt.

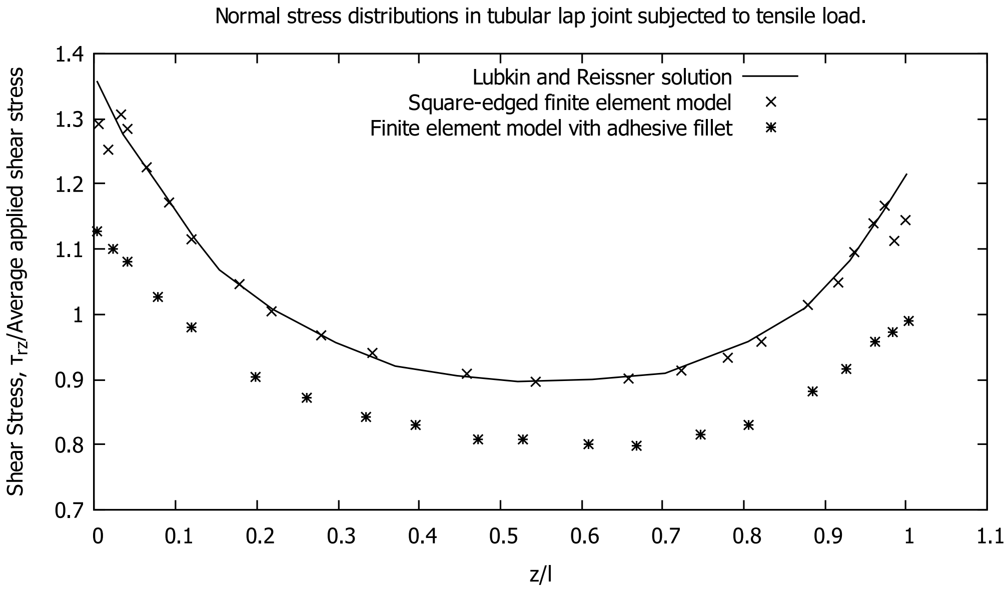

Figure 2.15: Shear stress distributions in tubular lap and scarf joints subjected to tensile load, Adams & Peppiatt.

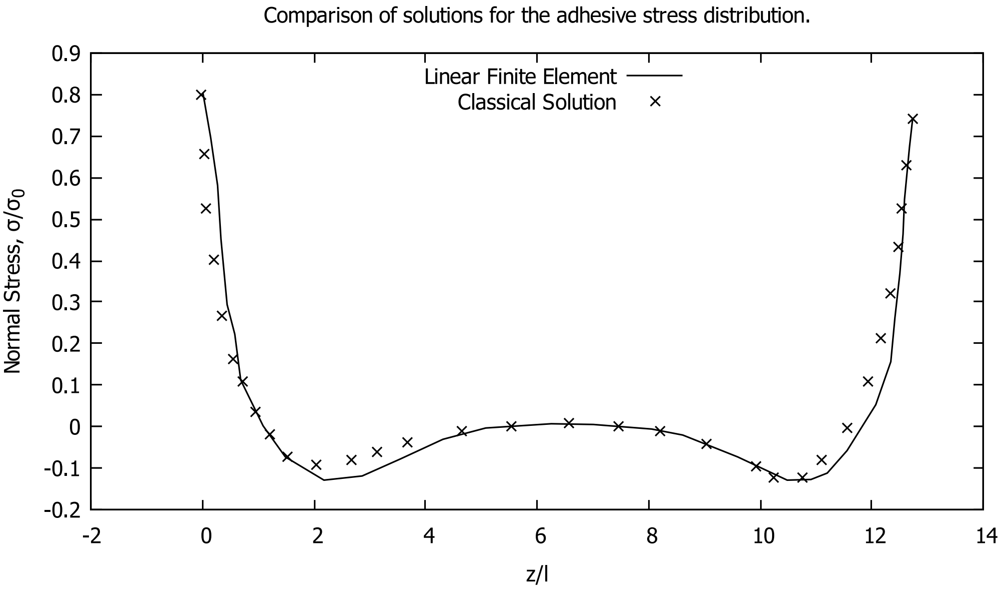

Figure 2.16: Peel stress distribution, Pickett & Hollaway.

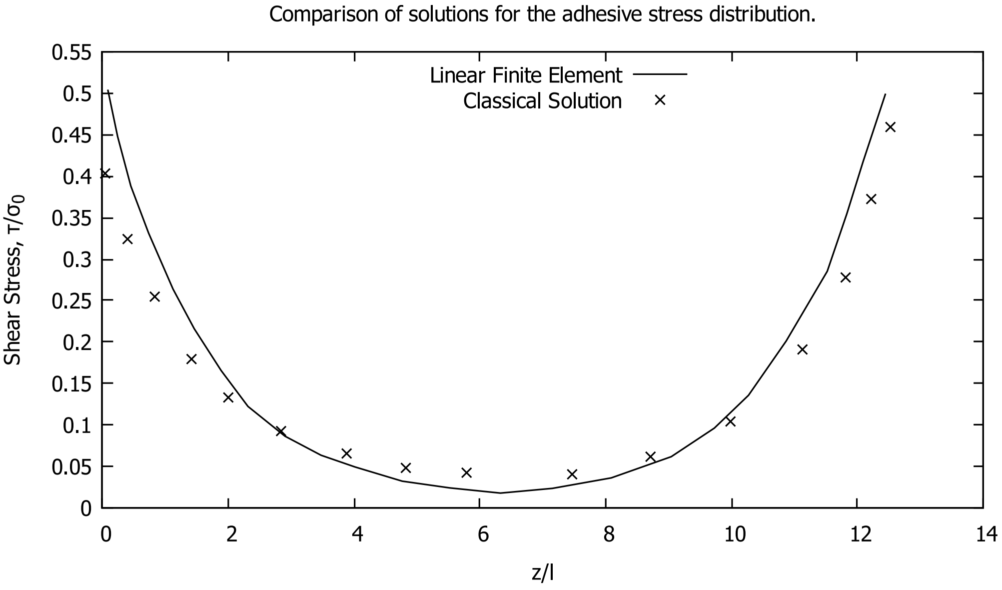

Figure 2.17: Shear stress distribution, Pickett & Hollaway.

Three-dimensional tests[4] validate previous analysis: in Kaya & Tekelioglu's works, an adhesively bonded single lap joint under axial tension force is studied; the adherends are assumed as isotropic and homogeneous aluminum, adhesive is modelled as an isotropic material and the variations of the stresses along the width are investigated (fig. 2.18, fig. 2.19). They used the finite element method with hexahedral elements with eight nodes having three degrees of freedom each, six elements were used through the thickness of the adherend and two elements through the thickness of the adhesive layer, so, the model consists of 4048 elements and 5148 nodes; results are shown below (peel and shear stress are normalized by the respective mean stress values and x- and y-coordinates by the length of the respective sides):

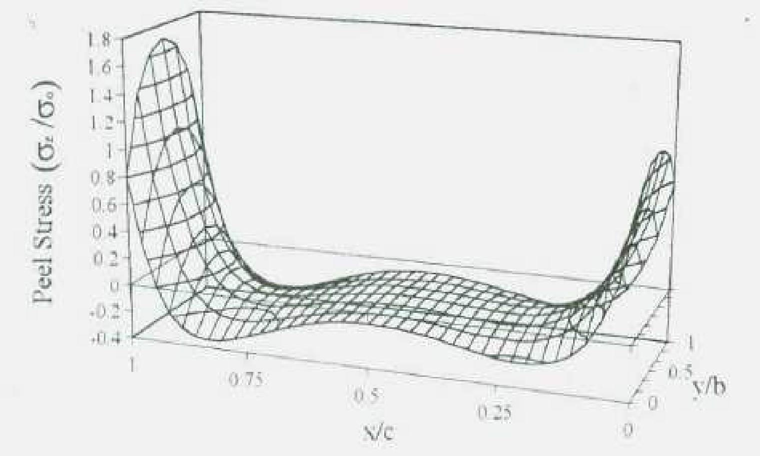

Figure 2.18: Peel Stress for three-dimensional analysis[4].

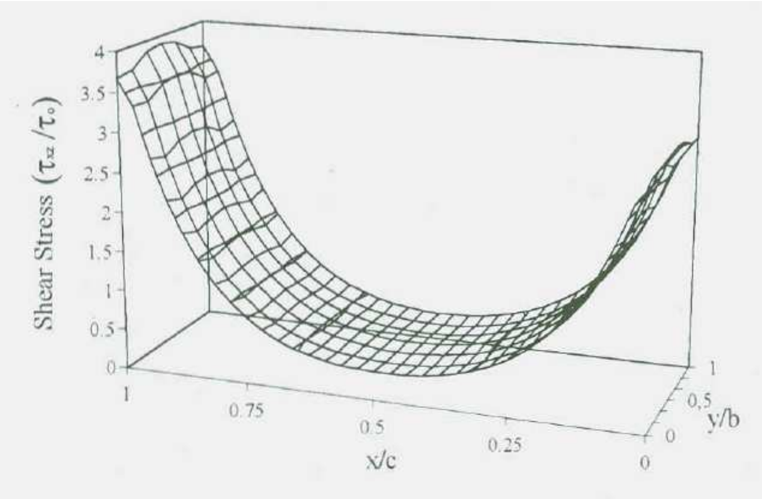

Figure 2.19: Shear Stress for three-dimensional analysis[4].

2.3 Joint Failures

As told previously, adhesive's bonding is a material jointing process in which an adhesive, placed between the adherend surfaces, solidifies to produce an adhesive bond and the modes of joint's failures are determined by the quality of the bond at each interface, specimen geometry and loading. According to ASTM D5573[6], in composite adhesive joints there are seven typical characterized modes of failure (fig. 2.20, fig. 2.21): adhesive failure, cohesive failure, thin-layer cohesive failure, fibre-tear failure, light-fibre-tear failure, stock-break failure and mixed failure, which (all together) belong to macro-areas of structural stress concentration (traction, compression, cleavage, shear and peeling). Although several researches made during the years[29][36][37][43][26], the failure prediction of the composite bonded joints is still difficult because the failure strength and mode are different according to various bonding methods and parameters; however, the primary failure modes for composite sandwich structures are buckling, local delamination and fatigue/fracture.

Three approaches have been used for studies: in the *continuum mechanics approach*[27], the adhesive and adherends are modelled by using continuum elements, assuming that the adhesive is perfectly bonded to the adherends and, thus, the assumption of a perfect bond means that the finite-element analysis takes no account of the adhesion properties of the interface; in the *fracture mechanics approach*[28], an energy parameter (toughness) is used as the failure criterion. In principle, it is possible to determine values of toughness as a function of the relative amounts of normal and shear deformation acting at the crack tip (in the adhesive, along the interface or through the adherend), and to use the concepts of mixed-mode fracture mechanics (failure occurs if local mixed mode energy release rate exceeds a critical value) to predict the appropriate crack path to calculate the strength of the joint under different loading conditions: this is the case of linear elastic fracture mechanics that relies on the existence of a crack and linear elasticity; the last approach is the *singularity approach*[15] (the fracture mechanics approach with no initial crack), which uses a generalized stress-intensity factor, analogous to the stress-intensity factor in classical fracture mechanics, to predict the beginning of the fracture for bonded joints: it was assumed that the beginning of fracture occurs when the generalized stress-intensity factor reaches its critical value and it was noticed that the intensity increased with increasing adhesive thickness and observed that this would account for decreasing joint strength with increasing adhesive thickness, which is verified experimentally.

Buckling is one of the most important failure modes for composite structures, which have low modulus of elasticity; instead, for all kinds of loading on skins and joints between composite materials, local delamination is one of the most severe failure modes since it can result in catastrophic failure for the global system structure; at last, interlaminar shear strength and through-thickness normal strength must then be carefully designed to prevent composite structures from local delamination.

The beginning of the various failure modes depends on the material properties of the constituents (facings, adhesive, and core), geometric dimensions and type of loading. Toftegaard & Lystrup[23] investigated theoretically and experimentally the failure modes in joined sandwich panels and observed two different types of failures: the first is the shear

failure of the base panel and the other one is the failure through the T-joint itself. The shear failure is a classical shear failure of sandwich panels consisting of shear fracture of the core and delamination between the core and skin laminates. The two types of failure resemble the failure types found for pullout loading of a T-joint with filler fillet and relatively thick overlaminates.
Safety considerations often require that adhesively bonded structures, particularly those employed in primary load-bearing applications, include mechanical fasteners (e.g. bolts) as an additional safety precaution, but these practices result in heavier and more costly components: the development of reliable design and predictive methodologies can be expected to result in more efficient use of composites and adhesives. To design structural joints in engineering structures, it is necessary to be able to analyse them and this means to determine stresses and strains under a given loading and to predict the probable points of failure.

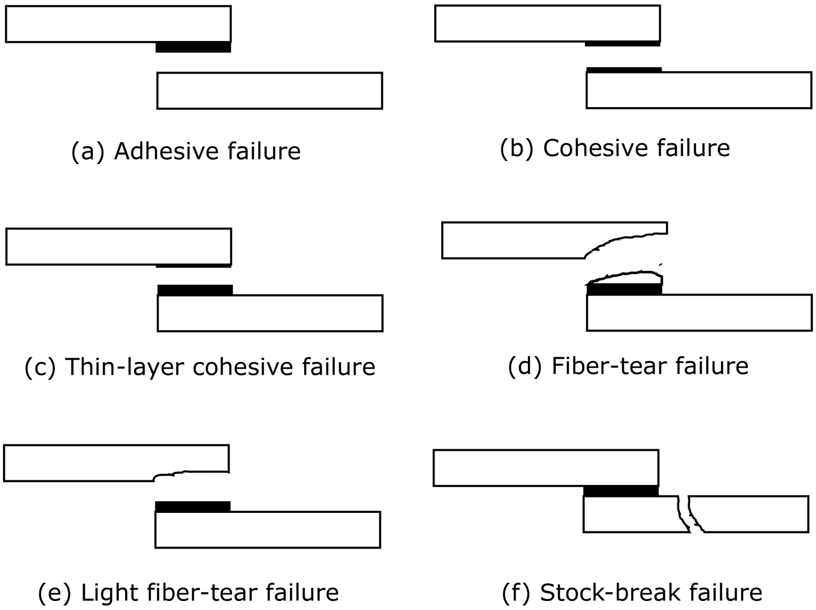
(a) Adhesive failure
(b) Cohesive failure
(c) Thin-layer cohesive failure
(d) Fiber-tear failure
(e) Light fiber-tear failure
(f) Stock-break failure

Figure 2.20: Modes of failure for a single lap joint.

Delaminations is one of the most critical and studied failure mode in laminated composites when there is no reinforcement in the thickness direction and they are generally assumed to take place at the interface between adjacent plies and treated as a fracture process between anisotropic layers, such as between adhesive and adherends[20]; these breakages may be induced by interlaminar peel and shear stresses associated to some geometrical configurations such as free edges or curved sections and they can buckling and growth under service conditions thus leading to the premature collapse of the structure as well as to the premature buckling of the laminate and stiffness degradation.
In this chapter the cohesive behaviour of the adhesives will be studied: in order to design structures that are damage-tolerant, analyses must be conducted to study the propagation of delaminations and this calculation can be performed using cohesive elements

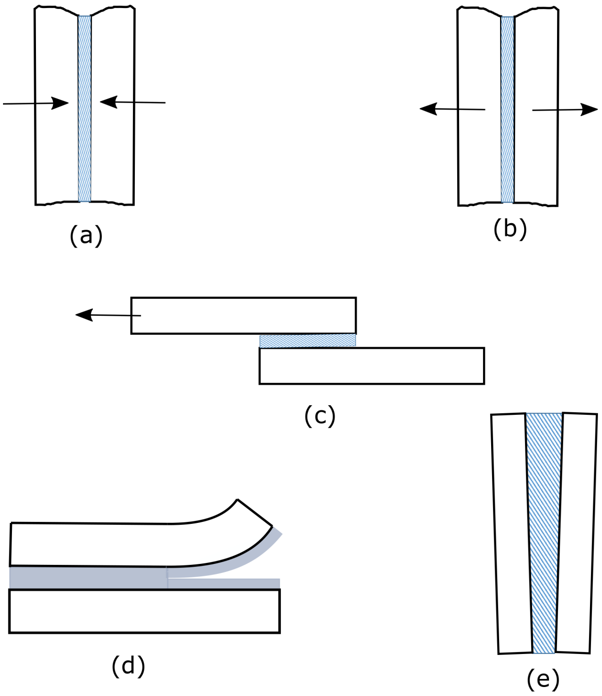

Figure 2.21: Typical stress failures in bonded joints: (a) compression, (b) traction, (c) shear, (d) peeling, (e) cleavage.

(implemented both in MUL^2 *CODE* and in ABAQUS), which can combine aspects of strength-based analysis to predict the onset of damage at the interface adherend-adhesive and of fracture mechanics to predict the propagation of a delamination in the material using the Cohesive Zone Model.

2.3.1 Linear elastic fracture mechanics, LEFM

The first of the three basic fracture mechanics modes of pure crack is the **Mode I** in which the loading is applied normally to the crack plane and provokes the opening of the crack and whose effects are the same as which ones caused by the peel stress; the second one is the **Mode II** in which a shear in-plane loading is applied and it produces the sliding of crack faces over each other and the last one is the **Mode III** which consists in an out-of-plane shear stress which moves the crack edges across each other in opposite directions (fig. 2.22). Mixed modes can occur as a combination of the three basic modes.

The energy associated to the crack propagation is called G which states for *energy release rate*, defined as the rate of change in potential energy with crack area for a linear elastic material: crack extension occurs when the energy release rate reaches a critical value, $G = G_c$, which is a measure of fracture toughness[25] and, as a consequence, a crack can only grow if the fracture process is in constant or decreased total energy. Thus, the critical condition for crack extension G_c can be defined as the point where crack growth occurs under equilibrium conditions: the balance equation under equilibrium conditions

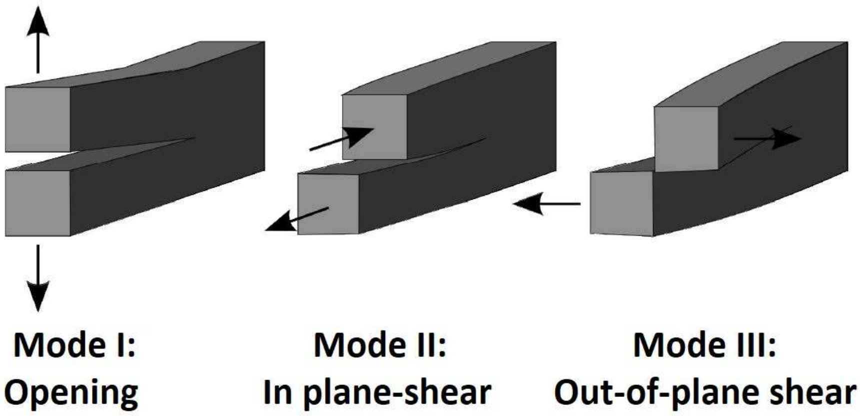

Figure 2.22: The three basic crack mode[5].

for an incremental increase in crack area, dA, can be so expressed as:

$$\frac{dE}{dA} = \frac{dP}{dA} + \frac{dW_s}{dA} = 0 \Rightarrow -\frac{dP}{dA} = \frac{dW_s}{dA} \tag{2.1}$$

where E is the total energy, dP is the potential energy in the form of strain energy and work done by external forces and W_s is the work needed to create two new surfaces; for an edge crack, two new surfaces are created when a crack is formed and, so, the expression for W_s becomes:

$$\frac{dW_s}{dA} = 2\gamma_s \tag{2.2}$$

where γ_s is the material specific surface energy. In brittle materials, a crack can form simply by breaking the atomic bonds and the surface energy γ_s represents the total energy of the broken bonds in an unit area; instead, in ductile metals, the crack propagation includes a plastic zone next to the crack tip which contributes to additional energy dissipation. The main hypothesis of this theory states that the global behaviour of the structure must be linear elastic, while plasticity must be confined to small regions around the crack tip and, thus, the modified expression takes the form:

$$W_f = \gamma_s + \gamma_p \tag{2.3}$$

where W_f is the fracture work made by the crack and γ_p is the plastic work per unit area of surface created. The concept is based on the energy release rate, G, defined as a measure of energy available for an increment of crack extension:

$$G = -\frac{dP}{dA} \tag{2.4}$$

Crack extension occurs when the energy release rate reaches a critical value, i.e when

$$G = G_c = \frac{dW_s}{dA} = 2W_f \tag{2.5}$$

However, the LEFM approach is incapable of dealing with those joints with large-scale plastic deformation occurring in the adherends because in these situations the energy absorbed by the fracture process is coupled with the energy dissipated by the macroscopic plasticity in adherends[25][30] and it is very difficult to separate one from the other: as a result, the measured joint toughness will depend on the joint geometry and cannot be treated as a material property.

2.3.2 Cohesive zone method, CZM

In order to analyse the phenomena of failure and fracture mechanics efficiently, especially in very thin geometries and in homogeneous solids, a general numerical method being able to simulate the initial loading, the damage initiation with initial debonding and the damage evolution until complete separation and failure is the *cohesive zone method*[38] which can be modelled as an interface between two continuum surfaces. The main aspect of CZM is that the stress of the cohesive zones works as a restraining stress that keeps the separating surfaces together and it corresponds to atomic or molecular attractions; this stress $\sigma = \sigma(\delta)$ is due to the external load T applied on the body and can be seen as a function of the separation distance δ_T included in Γ which is a generic surface around the crack tip (fig. 2.23):

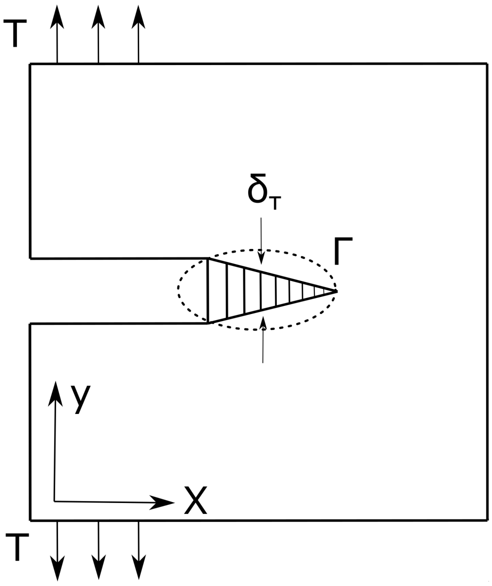

Figure 2.23: The cohesive zone: the crack characteristics[46].

The J-integral is the evaluation of the work in the crack zone made through a balance of forces; with reference to (fig. 2.23) the J-integral for the entire cohesive zone is[39]:

$$J = \int_{\Gamma} \left(W \, dy - T \frac{\partial u}{\partial x} \, ds \right) \tag{2.6}$$

Reducing Γ only to the lower and upper surface of the cohesive zone (CZ), $dy = 0$ and so eq. 2.6 can be rewritten as:

$$J = -\int_{CZ} \sigma(\delta)\frac{d\delta}{dx}dx = -\int_{CZ} \frac{d}{dx}\left\{\int_0^{\delta} \sigma(\delta)d\delta\right\}dx = \int_0^{\delta_\tau} \sigma(\delta)d\delta \tag{2.7}$$

When a cracked structure is exposed to some external loads, the crack surfaces are subjected to forces which prevent the surfaces from separating: these are the cohesive forces and the cohesive stress is a function of the relative displacement between the crack surfaces. The external loads will increase the infinitesimal separation δ until it reaches the value called δ^* in which the bond between the crack faces breaks and new free surfaces are created (fig. 2.24).

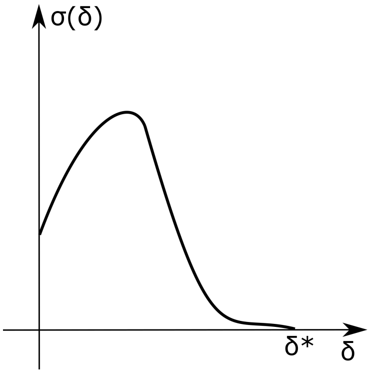

Figure 2.24: A typical stress-displacement diagram for a cohesive element.

When two new free surfaces are created, the cohesive stresses perform some amount of work:

$$W = \int_0^{\delta_{*\tau}} \sigma(\delta)d\delta = \int_0^{\delta_\tau} \sigma(\delta)d\delta \Rightarrow W = J \tag{2.8}$$

To propagate a crack through the distance Δa, a surface energy is needed which corresponds to:

$$\Delta W_s = \int_0^{\Delta a}\int_0^{\delta_*} \sigma(\delta)\; d\delta\; dx \tag{2.9}$$

and, using eq. 3.3, now it is possible to write the equation of crack development in the cohesive zone as:

$$\int_0^{\delta_*} = 2\gamma_s + \gamma_p \tag{2.10}$$

Cohesive elements are described by a constitutive law representing the crack propagation; in fact, the main statement of the CZM (modeled with continuum mechanics) is the traction-separation relation that simulates the effect of the fracture process and the interface tractions and separations between two bonded elements provides the link between

that fracture process and the macroscopic deformation in the surrounding materials.
This constitutive relation for a cohesive interface shows that the traction across the interface will vary depending on the separation of the crack and, with increasing separation, the traction will reach a maximum, start to decrease and eventually be reduced to zero: when the traction is zero, a complete decohesion of material occurs. The cohesive elements model the initial loading, the damage initiation and the damage evolution and these three parts can be identified in a curve as it is shown in fig. 2.25 in which a basic bilinear traction-separation law is described. This type of linear law is frequently used in calculations, but also an exponential function (fig. 2.26) can be used to study the softening after damage initiation because crack propagation can be simulated using different parameters that control the advance of the crack front for cohesive zone models with different mathematical formulations: these analyses can be even based on the local energy release or on the separation of the crack surfaces which corresponds to the displacement of the cohesive elements.

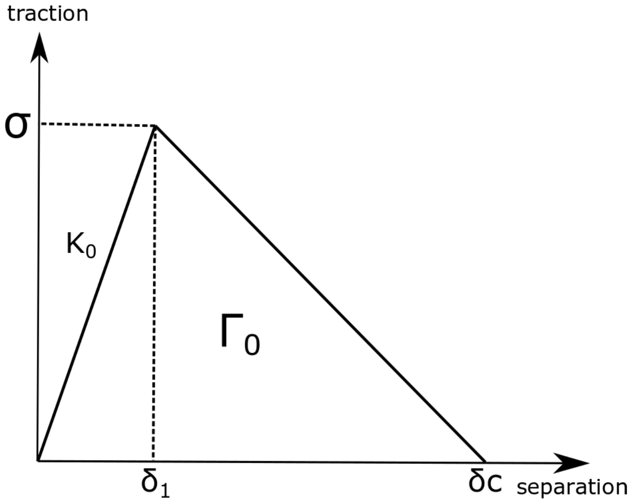

Figure 2.25: Bilinear traction-separation law.

Referring to fig. 2.25, the bilinear model is uniquely defined by this set of parameters: σ is the peak stress supported by the bonding tractions, δ_1 is a shape parameter, δ_c is the critical displacement, Γ_0 is the area of the triangle which represents the work of separation per unit area of crack advance (equal to the area under the traction-separation curve) and K_0 is the slope of the first part of the curve (which ensures realistic pre-crack conditions). The damage evolution, in both linear or exponential description, can be expressed as δ_f which is a function of the critical energy release rate Γ_0 calculated as follows:

$$\Gamma_0 = \int_0^{\delta_0} T(\delta) d\delta \tag{2.11}$$

It is important to underline that the cohesive model is a phenomenological model which can only model the real physical fracture process which in ductile materials involves also the processes of elasticity, plasticity and damage and, so, the shape of the

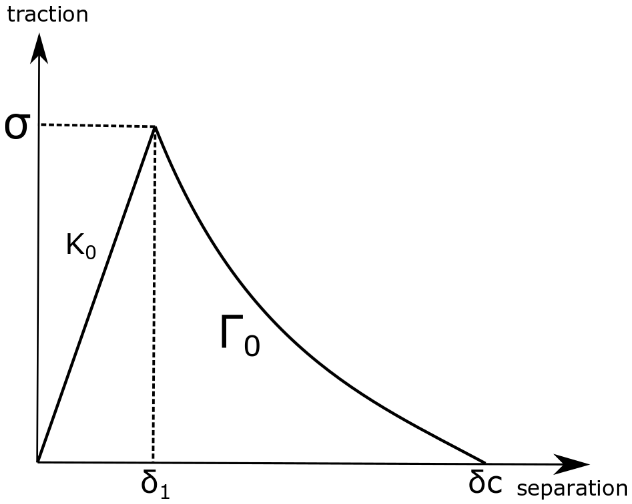

Figure 2.26: Exponential traction-separation law.

traction-separation law cannot easily be determined experimentally, and would have to be assumed; for example, Tvergaard and Hutchinson developed a model for an idealized traction-separation law specified on the crack plane[51] in which the relation is built on an increase of traction in the cohesive element until it reaches the peak traction δ_1 (fig. 2.27). Then, the traction will be constant until δ_2 is reached and, after that, the damage evolution is modeled until reaching δ_c where fracture occurs. In this case, Γ_0 is expressed as:

$$\Gamma_0 = \int_0^{\delta_1} \sigma d\delta = \frac{1}{2}\left[\delta_c + \delta_2 - \delta_1\right] \tag{2.12}$$

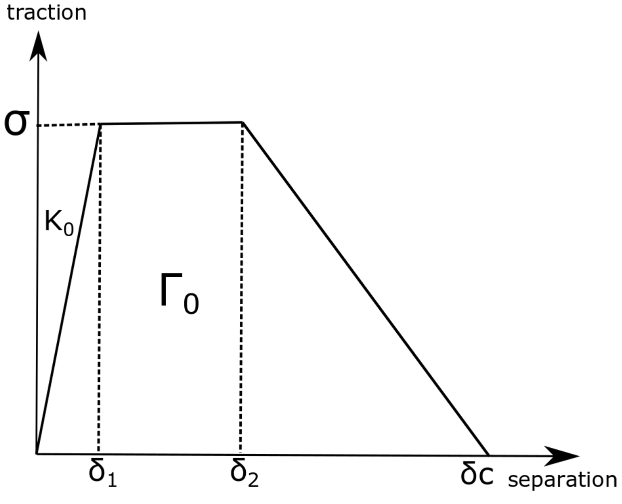

Figure 2.27: Tvergaard and Hutchinson traction-separation model[51].

Chapter 3

CUF 1D Model

The *Carrera Unified Formulation* (CUF) was developed by Carrera and his collaborators in the 1990s[10] as a hierarchical formulation to generate refined theories of structures based on the idea that non-classical effects (such as shear effects, warping, planar deformations and bending and torsional behaviour) can be studied increasing the order of the model used for analysis. The CUF 1D model is build on the beam cross-section (fig. 3.1) displacement field and is described by an expansion of generic functions F_τ

$$\mathbf{u}(x, y, z) = F_\tau(x, z) u_\tau(y), \qquad \tau = 1, \ldots, \mathrm{M} \tag{3.1}$$

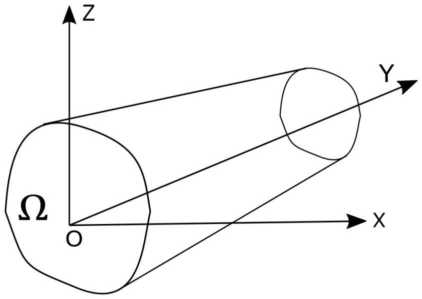

Figure 3.1: Coordinate system of the beam model.

where F_τ are the base functions approximating the generic displacements variable u along the volume V of the body, u_τ is the displacement vector and M is the number of the terms for the expansion; the choice of F_τ and M is arbitrary, thus different base functions of any order can be taken into account to model the displacement field of a beam above its cross-section. The order N of the expansion is arbitrary and is set as an input of the analysis and is usually made through a convergence study.
At first, the mathematical expansion theory used for the different CUF model orders was the *Taylor Expansion* (TE), but in order to overcome limits imposed by Taylor's polynomials and to achieve better results, the displacements field can be expressed with *Lagrangian Expansion* (LE) which allows to have only displacements variables and to

enrich the most important zones of the elements to study with many sub-domains, in order to better describe local phenomena and deformations. A further development of CUF theory was made by using the Hierarchical Legendre Expansion (HLE) which can be thought as a combination of TE and LE in order to enrich the locally the polynomial order. The unknowns of the HLE models are the generalized displacements and their derivatives and the expansion order is also increased in a hierarchical manner, as for TE and the kinematics of the model of Legendre expansions can be enriched locally over the physical surface of the cross-section, as for LE models.

3.1 Hierarchical High-Order Models

3.1.1 Taylor Expansion, TE

The *Taylor Expansion (TE)* is based on Taylor-like polynomial expansions of the displacements field over the cross-section of the structure (i and j are positive integers). The order N of the expansion is arbitrary and is set as an input of the analysis.
A convergence study is usually needed to choose N for a given structural problem and a generic displacements field can be expressed in this way[40]:

$$u_x = \sum_{N_i=0}^{N} \left(\sum_{M=0}^{N_i} x^{N-M} z^{M} \right) u_{x\, \frac{N(N+1)+M+1}{2}} \tag{3.2}$$

$$u_y = \sum_{N_i=0}^{N} \left(\sum_{M=0}^{N_i} x^{N-M} z^{M} \right) u_{y\, \frac{N(N+1)+M+1}{2}} \tag{3.3}$$

$$u_z = \sum_{N_i=0}^{N} \left(\sum_{M=0}^{N_i} x^{N-M} z^{M} \right) u_{z\, \frac{N(N+1)+M+1}{2}} \tag{3.4}$$

For example, the second-order model $N = 2$ has the following kinematic model[55][19]:

$$u_x = u_{x1} + x u_{x2} + z u_{x3} + x^2 u_{x4} + xz u_{x5} + z^2 u_{x6} \tag{3.5}$$

$$u_y = u_{y1} + x u_{y2} + z u_{y3} + x^2 u_{y4} + xz u_{y5} + z^2 u_{y6} \tag{3.6}$$

$$u_z = u_{z1} + x u_{z2} + z u_{z3} + x^2 u_{z4} + xz u_{z5} + z^2 u_{z6} \tag{3.7}$$

The 1D model described by eq. 3.5, 3.6, 3.7 has 18 generalized displacement variables (three constant, six linear, and nine parabolic terms): classical beam theories are obtainable as particular cases of Taylor expansions, even if classical theories require reduced material stiffness coefficients to contrast Poisson locking.
Nevertheless, the use of Taylor-type expansions has some intrinsic limitations that led to the introduction of different polynomial classes: first of all, the introduced variables have a mathematical meaning (derivatives at the beam axes) and, so, higher order terms do not

always have a physical local meaning, but they can have cross-section properties only; for this reason, the extension to large rotation formulation could lead to some mathematical difficulties.

3.1.2 Lagrange Expansion, LE

The *Lagrange Expansion* class *(LE)* exploits Lagrange polynomials to build 1D refined models that have displacement variables only: interpolation functions of the most used lagrangian L9 element (nine-point polynomials) are:

$$F_\tau = \frac{1}{4}(r^2 + rr_\tau)(s^2 + ss_\tau) \tag{3.8}$$

$$F_\tau = \frac{1}{2}s_\tau^2(s^2 + ss_\tau)(1 - r^2) + \frac{1}{2}r_\tau^2(r^2 + rr_\tau)(1 - s^2) \tag{3.9}$$

$$F_\tau = (1 - r^2)(1 - s^2) \tag{3.10}$$

in which r and s can vary between -1 and 1 and r_τ and s_τ are the coordinate frame of the nine points whose locations are shown in fig. 3.2, so, the displacement field of a L9 element is:

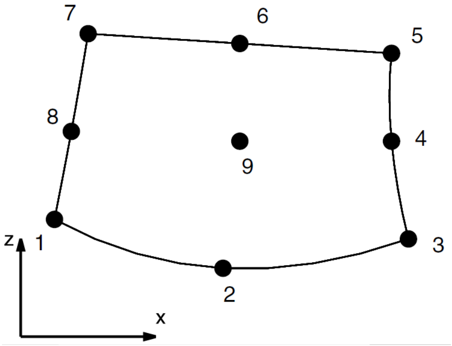

Figure 3.2: Lagrangian element with 9 nodes, L9 [40][55].

$$u_x = F_1u_{x1} + F_2u_{x2} + F_3u_{x3} + F_4u_{x4} + F_5u_{x5} + F_6u_{x6} + F_7u_{x7} + F_8u_{x8} + F_9u_{x9} \tag{3.11}$$

$$u_y = F_1u_{y1} + F_2u_{y2} + F_3u_{y3} + F_4u_{y4} + F_5u_{y5} + F_6u_{y6} + F_7u_{y7} + F_8u_{y8} + F_9u_{y9} \tag{3.12}$$

$$u_z = F_1u_{z1} + F_2u_{z2} + F_3u_{z3} + F_4u_{z4} + F_5u_{z5} + F_6u_{z6} + F_7u_{z7} + F_8u_{z8} + F_9u_{z9} \tag{3.13}$$

where u_{x1}, …, u_{z9} are the displacements variables.

In LE, each variable has a precise physical meaning (the problem unknowns are only translational displacements) and, in fact, unknown variables can be put in fixed zones (sub-domains) of the cross-section refining and enriching the model in certain areas only; more, geometrical boundary conditions can be applied both in sub-domains of the cross-section (and not only to the whole cross-section) and along the beam-axis, as well. The cross-section itself can be divided into further beam sections and easily assembled since the displacements at each boundary are used as problem unknowns and, at last, the extension to geometrically non-linear problems appears more suitable than in the case of Taylor-type higher-order theories.

3.1.3 Hierarchical Legendre Expansion, HLE

The one-dimensional *Hierarchical Legendre Expansion* models (HLE) are formulated by expressing the 3D displacements field as a Legendre-based expansion of the generalized displacements along the beam axis[18]: the rates of convergence are exponential. Two-dimensional polynomial expansions can be then defined by extending the above procedure to quadrilateral domains on the beam cross-section: in this case, nodal, edge and internal polynomials are used as interpolation functions over the section.

For Taylor Expansion models (TE) the generalized displacement unknowns (displacements and their derivatives) are expanded on the cross-section surface from the reference axis and the polynomial order of the model is increased in a hierarchical manner by adding new terms to the kinematic field[41]; Lagrange Expansion models (LE) are based on local expansions of pure displacement unknowns within each of the sub-domains in which the surface is divided[11]. HLE can be thought as a combination of these two models: the unknowns of the HLE models are the generalized displacements and their derivatives and the expansion order is also increased in a hierarchical manner, as for TE; Legendre-like expansions can be enriched locally over the physical surface of the cross-section, as for LE models. The expansion order is set as a free input of the model in the solver code and this determines the number of unknowns to be solved: HLE, so, combines the main advantages of TE (e.g., the hierarchy of the higher-order terms) and LE (e.g., exact geometrical description of the beam physical surfaces)[18].

In order to demonstrate the numerical convergence of the solution, especially when problem is modelled using a finite element program, more than one solution to the same problem is required; three methods are used in this report:

- *h - method*[2] : improves results by using a finer mesh of the same type of element. This method refers to decreasing the characteristic length *(h)* of elements, dividing each existing element into two or more elements without changing the type of elements used and, so, more accurate information is obtained by increasing the number of elements[1]. A coarse mesh leads to a very inaccurate stress distribution across the region analysed; therefore, in order to increase the accuracy of the solution, more

---

[1] In mathematics the variable h is used to specify the step size in numeric integration: this explains the name given to this method.

elements must be added: this means creating a finer mesh.
The *h - method* analytical steps are: as an initial run, a coarse mesh is used to model the problem and a solution is obtained. To check this solution, a finer mesh is created (the mesh must always be changed if a more accurate solution is desired). Now, the problem is run again to obtain a second solution. If there is a large difference between the two solutions, the mesh must be made even finer and then problem must be solved again: this process is repeated until the solution error acquires low values

- *p - method*[2] : improves results by using the same mesh, but increasing the displacement field accuracy in each element. This method refers to increasing the degree of the highest complete polynomial *(p)* within an element without changing the number of elements used[2]. In order to increase the accuracy of the solution, the complexity of the shape functions must be increased: in this way, increasing the polynomial order increases the complexity of the shape function.
  The *p - method* analytical steps are: as an initial run, the solution might be solved using a first order polynomial shape function and a solution is obtained. To check this solution, the problem will be solved again using a more complicated (for example third order) shape function and a second solution is obtained: the output from the two runs is compared. If there is a large difference between the two solutions, then the solution should be run using a third (or higher) order polynomial shape function: this process is repeated until the solution error acquires low values

- *hp - method* : the analysis shown in the next chapters for both Peel and Shear Stress will use the *hp - method* based on Hierarchical Legendre Expansions *(HLE)*, a complex combination of both finer and finer meshes and higher and higher polynomial degree expansions.

3.2 CUF Finite Element Formulation

The proper and general form of governing equations are derived from discretizing the beam axis with classical 1D elements, as follows:

$$\mathbf{u}(x,y,z) = F_\tau(x,z)N_i(y)q_{\tau i} \tag{3.14}$$

N_i stands for the shape functions and $q_{\tau i}$ for the nodal displacement vector,

$$\mathbf{q}_{\tau i} = \left\{ q_{u_{x_{\tau i}}}, q_{u_{y_{\tau i}}}, q_{u_{z_{\tau i}}} \right\} \tag{3.15}$$

Now, according to the notation of fig. 3.1 in which Ω stands for the cross section of the structure, stresses σ and strains ε can be rewritten as follows:

---

[2] The “p” in *p - method* stands for “polynomial”: the mesh does not need to be changed when using the *p - method.*

$$\sigma_p = \{\sigma_{zz}, \sigma_{xx}, \sigma_{xz}\}^T \qquad \varepsilon_p = \{\varepsilon_{zz}, \varepsilon_{xx}, \varepsilon_{xz}\}^T \tag{3.16}$$

$$\sigma_n = \{\sigma_{zz}, \sigma_{xx}, \sigma_{xz}\}^T \qquad \varepsilon_n = \{\varepsilon_{zz}, \varepsilon_{xx}, \varepsilon_{xz}\}^T \tag{3.17}$$

where p refers to terms on the cross section and n are the terms acting on the plans perpendicular to Ω.
For little displacements if referring to the cross section of the beam, the relation between σ and ε is linear so, from eq. 3.16 and 3.17, it's possible to write:

$$\varepsilon_n = \{u_{z,y} + u_{y,z} \;\; u_{x,y} + u_{y,z} \;\; u_{y,y}\}^T \tag{3.18}$$

$$\varepsilon_p = \{u_{z,z} \quad u_{x,x} \quad u_{z,x} + u_{x,z}\}^T \tag{3.19}$$

which can be expressed as:

$$\varepsilon_n = D_n u = (D_{np} + D_{ny} u) \tag{3.20}$$

$$\varepsilon_p = D_p u \tag{3.21}$$

where D_{np}, D_{ny} and D_p are the differential matrices written as

$$D_p = \begin{bmatrix} 0 & 0 & \frac{\partial}{\partial z} \\ \frac{\partial}{\partial x} & 0 & 0 \\ \frac{\partial}{\partial z} & 0 & \frac{\partial}{\partial x} \end{bmatrix} \qquad D_{np} = \begin{bmatrix} 0 & \frac{\partial}{\partial z} & 0 \\ 0 & \frac{\partial}{\partial x} & 0 \\ 0 & 0 & 0 \end{bmatrix} \qquad D_{ny} = \begin{bmatrix} 0 & 0 & \frac{\partial}{\partial y} \\ \frac{\partial}{\partial y} & 0 & 0 \\ 0 & \frac{\partial}{\partial y} & 0 \end{bmatrix} \tag{3.22}$$

and also stresses σ, using eq. 3.8, can be rewritten as:

$$\sigma = \tilde{C}\varepsilon \tag{3.23}$$

which, from eq. 3.20 and 3.21, becomes

$$\sigma_p = \tilde{C}_{pp}\varepsilon_p + \tilde{C}_{pn}\varepsilon_n \tag{3.24}$$

$$\sigma_n = \tilde{C}_{np}\varepsilon_p + \tilde{C}_{nn}\varepsilon_n \tag{3.25}$$

in which $\tilde{C}_{pp}$, $\tilde{C}_{pn}$, $\tilde{C}_{np}$, $\tilde{C}_{nn}$ are the coefficient matrices of the material. Using shape functions N_i and F_τ, strains expressed in 3.20 and 3.21 can be written as

$$\varepsilon_n = (D_{np} F_\tau I) N_i q_{\tau i} + F_\tau (D_{ny} N_i I) N_i q_{\tau i} \tag{3.26}$$

$$\varepsilon_p = (D_p F_\tau I) N_i q_{\tau i} \tag{3.27}$$

where **I** is the *3 x 3* identity matrix.

3.2.1 The Principle of Virtual Displacements (PVD)

The *Principle of Virtual Displacements* (PVD) can study non-elastic problems and it is based on two totally independent systems which act within a structural model:

- *system "a"*: it involves the stress due to the constraints (internal loads) or mechanical loads (external loads)
- *system "b"*: the body warps in respect of links between internal constraints and deformations due to external loads; the deformed body maintains continuity and each material properties

In a system, the work made by all the external loads F^a when the respective points of applications are subjected to the displacements η_b due to the deformations of the *system "b"* is called external work L_e^{ab} and it can be expressed in this way:

$$L_e^{ab} = \Sigma \left(F^a \eta^b \right) \tag{3.28}$$

where the sum is extended to every concentrated forces of *system "a"*; if the forces were distributed on lines (beams), surfaces (plates) or volumes (shells), the sum has to be substituted by, respectively, simple, double or triple integrals.
The internal work L_i^{ab} is defined by the integral of the work made by the stress forces of the *system "a"* (calculated on each volume part which constitute the whole structure) to provoke the deformations on *system "b"*. The Principle of Virtual Displacements, thus, states the following equality:

$$L_{ext}^{ab} = L_{int}^{ab} \tag{3.29}$$

the work made by the external forces must have the same value as the internal displacements in the structure.
Some correlations between different situations state:

- the system of forces and tensions is in equilibrium
- the system of displacements and deformations is congruent
- the work made by the external forces is the same as the work made by the internal tensions

and a criterion of necessity states between these statements: if the first two statements are true, also the last one will be true and, generally, if two of the statements are true, also the other one will be true. This relationship between them is fundamental to solve a statically indeterminate beam (the main application field of this principle): considering a system of forces and stresses in equilibrium, if the PVD is true upon a system of displacements and deformations, this last is necessarily congruent; vice versa, considering a system of congruent displacements and deformations, the equality between internal and external forces leads necessarily to state the system of forces and stresses in equilibrium and, thus, the *PVD*, considering a system of forces and stresses (or displacements and deformations) which is surely in equilibrium (or congruent), provides informations about the only solution of the problem, which must be both in equilibrium and congruent.

3.2.2 Stiffness Matrix

According to the principle of virtual displacements seen before, for CUF the eq. 3.29 can be written as:

$$\delta L_{int} = \int_V (\delta \varepsilon^T \sigma) dV = \delta L_{ext} + \delta L_{ine} \tag{3.30}$$

where V is the volume domain of the body, δL_{int} is the internal work (strain energy), δL_{ext} is the external work, δL_{ine} is the inertial work (which can be included directly in the external work) and δ stands for the virtual variation; as usual, σ and ε stand, respectively, for the stress and strain vectors.
Stiffness matrix is obtained from eq. 3.30 rewritten (using equations 4.24 and 4.25) as:

$$\delta L_{int} = \int_V (\delta \varepsilon_p^T \sigma_p + \delta \varepsilon_n^T \sigma_n) dV = \delta L_{ext} + \delta L_{ine} \tag{3.31}$$

Substituting the constitutive equations for materials (eqs. 3.24, 3.25, 3.26, 3.27), the internal work δL_{int} becomes

$$\begin{aligned} \delta L_{int} = \delta q_{\tau i}^T \int_l \int_\Omega &([N_i(D_{np}^T F_\tau I) + (D_{ny}^T N_i I) F_\tau][\tilde{C}_{np}(D_p F_s I) N_j + \\ &+ \tilde{C}_{nn}(D_{np} F_s I) N_j + \tilde{C}_{nn} F_s (D_{ny} N_j I)] + \\ &+ N_i (D_p^T F_\tau I)[\tilde{C}_{pp}(D_p F_s I) N_j + \tilde{C}_{pn}(D_{np} F_s I) N_j + \\ &+ \tilde{C}_{pn} F_s (D_{ny} N_j I)] \, d\Omega \, dy) \, q_{sj} = \delta L_{ext} + \delta L_{ine} \end{aligned} \tag{3.32}$$

which can be written in as simpler way, expressing the **Stiffness matrix** $K^{ij\tau s}$:

$$\delta L_{int} = \delta q_{\tau i}^T K^{ij\tau s} q_{sj} \tag{3.33}$$

By introducing eqs. 3.24 and 3.25 in eq. 3.33 it is possible to rewrite the virtual variation of $K^{ij\tau s}$ as

$$\begin{aligned} K^{ij\tau s} = I_l^{ij} \int_\Omega &(D_{np}^T F_\tau I)[\tilde{C}_{np}(D_p F_s I) + \tilde{C}_{nn}(D_{np} F_s I)] + \\ &+ (D_p^T F_\tau I)[\tilde{C}_{pp}(D_p F_s I) + \tilde{C}_{pn}(D_{np} F_s I)] \, d\Omega + \\ &+ I_l^{ij,y} \int_\Omega [(D_{np}^T F_\tau I)\tilde{C}_{nn} + (D_p^T F_\tau I)\tilde{C}_{pn}] F_s \, d\Omega \, I_{\Omega_y} + \\ &+ I_l^{i,yj} I_{\Omega_y} \int_\Omega F_\tau [\tilde{C}_{np}(D_p F_s I) + \tilde{C}_{nn}(D_{np}^T F_s I)] \, d\Omega + \\ &+ I_l^{i,yj,y} I_{\Omega_y} \int_\Omega F_\tau \tilde{C}_{nn} F_s \, d\Omega \, I_{\Omega_y} \end{aligned} \tag{3.34}$$

where:

$$I_{\Omega_y} = \begin{bmatrix} 0 & 1 & 0 \\ 1 & 0 & 0 \\ 0 & 0 & 1 \end{bmatrix} \tag{3.35}$$

and

$$(I_l^{ij}, I_l^{ij,y}, I_l^{i,yj}, I_l^{i,yj,y}) = \int_l (N_i N_j, N_i N_{j,y}, N_{i,y} N_j, N_{i,y} N_{j,y}) \tag{3.36}$$

The matrix $K^{ij\tau s}$ is called the fundamental nucleus of the Stiffness Matrix: it does not depend on the expansion order of the theory or on the polynomial expansion F_τ chosen and, thus, both LE and TE and HLE can be obtained from the same fundamental nucleus; its components are reported below[35][40]:

$$\begin{aligned} K_{xx}^{ij\tau s} = {} & \tilde{C}_{22} \int_\Omega F_{\tau,x} F_{s,x} \, d\Omega \int_l N_i N_j \, dy + \tilde{C}_{66} \int_\Omega F_\tau F_s \, d\Omega \int_l N_{i,y} N_{j,y} \, dy + \\ & + \tilde{C}_{44} \int_\Omega F_{\tau,z} F_{s,z} \, d\Omega \int_l N_i N_j \, dy + \tilde{C}_{26} \int_\Omega F_{\tau,x} F_s \, d\Omega \int_l N_i N_{j,y} \, dy + \\ & + \tilde{C}_{26} \int_\Omega F_\tau F_{s,x} \, d\Omega \int_l N_{i,y} N_j \, dy \end{aligned} \tag{3.37}$$

$$\begin{aligned} K_{xy}^{ij\tau s} = {} & \tilde{C}_{66} \int_\Omega F_\tau F_{s,x} \, d\Omega \int_l N_{i,y} N_j \, dy + \tilde{C}_{45} \int_\Omega F_{\tau,z} F_{s,z} \, d\Omega \int_l N_i N_j \, dy + \\ & + \tilde{C}_{23} \int_\Omega F_{\tau,z} F_s \, d\Omega \int_l N_i N_{j,y} \, dy + \tilde{C}_{36} \int_\Omega F_\tau F_s \, d\Omega \int_l N_{i,y} N_{j,y} \, dy + \\ & + \tilde{C}_{26} \int_\Omega F_{\tau,x} F_{s,x} \, d\Omega \int_l N_i N_j \, dy \end{aligned} \tag{3.38}$$

$$\begin{aligned} K_{xz}^{ij\tau s} = {} & \tilde{C}_{45} \int_\Omega F_{\tau,z} F_s \, d\Omega \int_l N_i N_{j,y} \, dy + \tilde{C}_{12} \int_\Omega F_{\tau,x} F_{s_z} \, d\Omega \int_l N_i N_j \, dy + \\ & + \tilde{C}_{16} \int_\Omega F_\tau F_{s,z} \, d\Omega \int_l N_{i,y} N_j \, dy + \tilde{C}_{44} \int_\Omega F_{\tau,z} F_{s_x} \, d\Omega \int_l N_i N_j \, dy \end{aligned} \tag{3.39}$$

$$\begin{aligned} K_{yx}^{ij\tau s} = {} & \tilde{C}_{66} \int_\Omega F_{\tau,x} F_s \, d\Omega \int_l N_i N_{j,y} \, dy + \tilde{C}_{45} \int_\Omega F_{\tau,z} F_{s,z} \, d\Omega \int_l N_i N_j \, dy + \\ & + \tilde{C}_{23} \int_\Omega F_\tau F_{s,x} \, d\Omega \int_l N_{i,y} N_j \, dy + \tilde{C}_{36} \int_\Omega F_\tau F_s \, d\Omega \int_l N_{i,y} N_{j,y} \, dy + \\ & + \tilde{C}_{26} \int_\Omega F_{\tau,x} F_{s,x} \, d\Omega \int_l N_i N_j \, dy \end{aligned} \tag{3.40}$$

$$\begin{aligned} K_{yy}^{ij\tau s} = {} & \tilde{C}_{66} \int_\Omega F_{\tau,x} F_{s,x} \, d\Omega \int_l N_i N_j \, dy + \tilde{C}_{36} \int_\Omega F_{\tau,x} F_s \, d\Omega \int_l N_i N_{j,y} \, dy + \\ & + \tilde{C}_{36} \int_\Omega F_\tau F_{s,x} \, d\Omega \int_l N_{i,y} N_j \, dy + \tilde{C}_{55} \int_\Omega F_{\tau,z} F_{s,z} \, d\Omega \int_l N_i N_j \, dy + \\ & + \tilde{C}_{33} \int_\Omega F_\tau F_s \, d\Omega \int_l N_{i,y} N_{j,y} \, dy \end{aligned} \tag{3.41}$$

$$\begin{aligned} K_{yz}^{ij\tau s} = {} & \tilde{C}_{22} \int_\Omega F_{\tau,z} F_{s,x} \, d\Omega \int_l N_i N_j \, dy + \tilde{C}_{55} \int_\Omega F_{\tau,z} F_s \, d\Omega \int_l N_i N_{j,y} \, dy + \\ & + \tilde{C}_{13} \int_\Omega F_\tau F_{s,z} \, d\Omega \int_l N_{i,y} N_j \, dy + \tilde{C}_{16} \int_\Omega F_{\tau,x} F_{s,z} \, d\Omega \int_l N_i N_j \, dy \end{aligned} \tag{3.42}$$

$$\begin{aligned} K_{zx}^{ij\tau s} = {} & \tilde{C}_{45} \int_\Omega F_\tau F_{s,z} \, d\Omega \int_l N_{i,y} N_j \, dy + \tilde{C}_{12} \int_\Omega F_{\tau,z} F_{s,x} \, d\Omega \int_l N_i N_j \, dy + \\ & + \tilde{C}_{16} \int_\Omega F_{\tau,z} F_s \, d\Omega \int_l N_i N_{j,y} \, dy + \tilde{C}_{44} \int_\Omega F_{\tau,x} F_{s,z} \, d\Omega \int_l N_i N_j \, dy \end{aligned} \tag{3.43}$$

$$\begin{aligned} K_{zy}^{ij\tau s} = {} & \tilde{C}_{45} \int_\Omega F_{\tau,x} F_{s,z} \, d\Omega \int_l N_i N_j \, dy + \tilde{C}_{55} \int_\Omega F_\tau F_{s,z} \, d\Omega \int_l N_{i,y} N_j \, dy + \\ & + \tilde{C}_{13} \int_\Omega F_{\tau,z} F_s \, d\Omega \int_l N_i N_j \, dy + \tilde{C}_{16} \int_\Omega F_{\tau,z} F_{s,x} \, d\Omega \int_l N_i N_j \, dy \end{aligned} \tag{3.44}$$

$$\begin{aligned} K_{zz}^{ij\tau s} = {} & \tilde{C}_{55} \int_\Omega F_\tau F_s \, d\Omega \int_l N_{i,y} N_{j,y} \, dy + \tilde{C}_{11} \int_\Omega F_{\tau,z} F_{s,z} \, d\Omega \int_l N_i N_j \, dy + \\ & + \tilde{C}_{45} \int_\Omega F_\tau F_{s,x} \, d\Omega \int_l N_{i,y} N_j \, dy + \tilde{C}_{45} \int_\Omega F_{\tau,x} F_s \, d\Omega \int_l N_i N_{j,y} \, dy + \\ & + \tilde{C}_{44} \int_\Omega F_{\tau,x} F_{s,x} \, d\Omega \int_l N_i N_j \, dy \end{aligned} \tag{3.45}$$

The assembling loop of the stiffness matrix is shown in fig. 3.3.
Finally, the work of the external forces δL_{ext} can be expressed as:

$$\begin{aligned} \delta L_{ext} & = \int_V (\delta u^T \tilde{F}) \, dV = \\ & = \delta q_{\tau i}^T \int_V (N_i(y) F_\tau(x,z) \tilde{F}) \, dV = \\ & = \delta q_{\tau i}^T P^{\tau i} \end{aligned} \tag{3.46}$$

where $\tilde{F}$ is the generic load and $P^{\tau i}$ is the vector of the nodal forces, so the following linear algebraic system has to be solved:

$$\tilde{K} q = \tilde{F} \tag{3.47}$$

in which $\tilde{K}$ is the global stiffness, q is the loading and $\tilde{F}$ is the unknowns arrays, respectively.

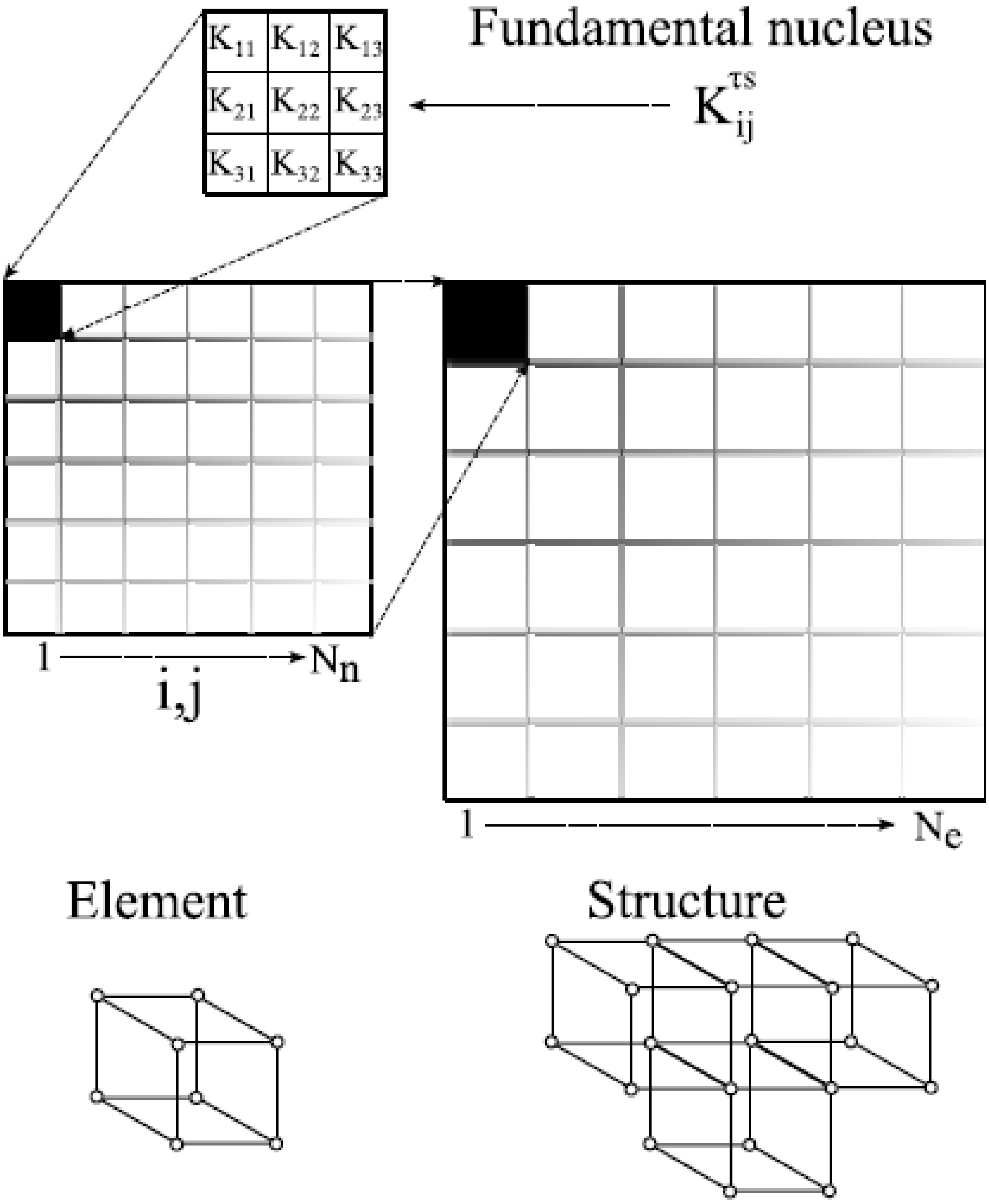

Figure 3.3: Assembly procedure for a stiffness matrix for a solid model[55].

Chapter 4

Numerical modelling of bonded joints

The theoretical insights expressed in the previous chapters for the calculation of Young's and shear modulus, the Poisson's coefficient and the stress and strain evolution allow only to show the theoretical behaviour of materials under loads and constraints. This chapter shows the numerical results obtained by using the MUL^2 *CODE*[3] and the aim is dual: first of all, the validation of the code in reference to literature results and to the commercial finite element package ABAQUS; then, the investigation of concentration and distribution of Peel and Shear stresses in lap joints of different nature such as butt joint, single lap and double lap joint. Values of stress for both MUL^2 *CODE* and ABAQUS have been normalized by the Young's modulus of the adhesive to make the results independent from the material used.

4.1 Adhesive butt joint of thin plates

The problem solved in this report is the 3D solution (fig. 4.1) of a two-dimensional case of study taken from T. Sawa's works[50][9] included in the da Silva & Ochsner's essay[49] and it consists in two adherends bonded by an adhesive: each finite strip was analysed through the two-dimensional theory of elasticity based on the three-body contact problem using Airy's stress functions, which were selected from solutions for the method of separation of variables. Then, in order to verify the analytical results, an experiment was performed concerning the strains produced on the adherends (thickness $H = 4mm$) in which the specimens were prepared from steel and aluminum.
From the hypothesis and geometrical relationships reported in [50] and using Cartesian coordinates *(x, y, z)*, physical characteristics can be evaluated in the following tab. 4.1[1]:

In [50] the tensile loading is applied to both ends of the adherends developed by Fourier series and called $F(x)$ and $G(x)$ respectively for the top and bottom adherend

---

[1] In the table 4.1, *"1"* stands for the bottom adherend, *"2"* for the adhesive and *"3"* for the top adherend.

Quantity	**Value**	**Geometrical characteristics**	**Value**
E_1	75 GPa	E_2	25 GPa
		E_3	50 GPa
G_1	28.195 GPa	G_2	9.398 GPa
		G_3	18.79 GPa
ν_1	0.33	ν_2	0.33
		ν_3	0.33
h_1	0.4 mm		
h_2	0.08 mm		
h_3	0.4 mm		
H (thickness)	0.4 mm		
l (half-length)	1 mm		

Table 4.1: Butt joint - Material and geometrical properties.

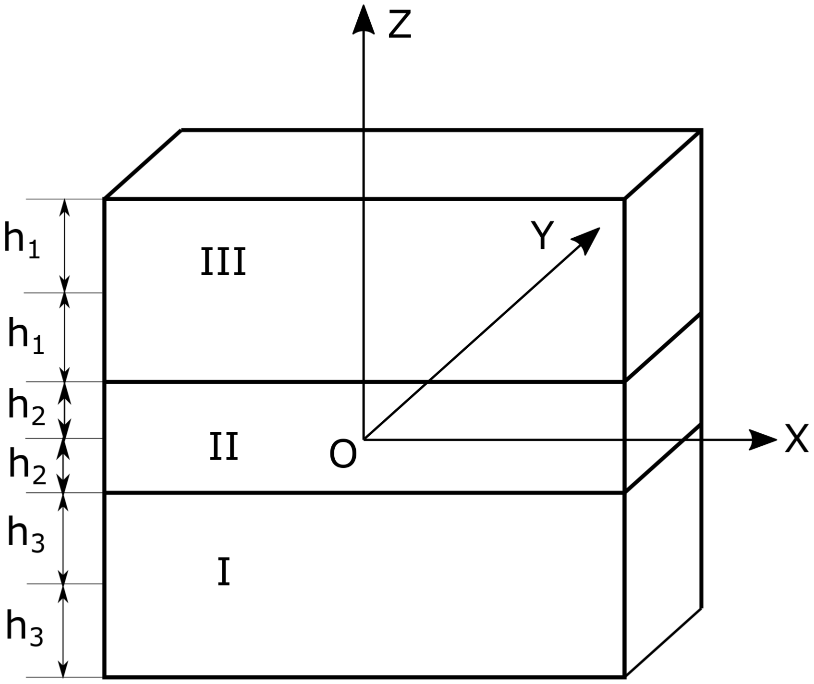

Figure 4.1: Adhesive butt joint, Sawa[50].

stress distribution; the boundary conditions are described by:

- on finite stripe of adherend **I**:

$$\begin{cases} \sigma_x^I = \tau_{xy}^I = 0, \quad x = \pm l \\ \sigma_y^I = F(x) = a_0 + \sum_{s=1}^{\infty} a_s cos\left(\frac{s\pi x}{l}\right), \quad y_1 = h_1 \\ \tau_{xy}^I = 0 \end{cases} \tag{4.1}$$

- on finite strip of the adhesive (**II**):

$$\sigma_x^{II} = \tau_{xy}^{II} = 0, \qquad x = \pm l \tag{4.2}$$

- on finite strip of the adherend **III**:

$$\begin{cases} \sigma_x^{III} = \tau_{xy}^{III} = 0, \qquad x = \pm l \\ \sigma_y^{III} = G(x) = b_0 + \sum_{s=1}^{\infty} b_s cos\left(\frac{s\pi x}{l}\right), \qquad y_1 = h_1 \\ \tau_{xy}^{III} = 0 \end{cases} \tag{4.3}$$

- at the interface between finite strips **I** and **II**:

$$\begin{cases} (\sigma_y^I)_{y_1=-h_1} = (\sigma_y^{II})_{y_2=h_2} \\ (\tau_{xy}^I)_{y_1=-h_1} = (\tau_y^{II})_{y_2=h_2} \\ (u^I)_{y_1=-h_1} = (u^{II})_{y_2=h_2} \\ \left(\frac{\partial \nu^I}{\partial x}\right)_{y_1=-h_1} = \left(\frac{\partial \nu^{II}}{\partial x}\right)_{y_2=h_2} \end{cases} \tag{4.4}$$

where a_0, b_0, a_s, b_s are the Fourier's coefficients referred to $F(x)$ and $G(x)$.

4.1.1 MUL^2 *CODE* discretization

The beam element chosen to analyse the butt-joint are the cubic beam elements $2B4$ through the thickness (fig. 4.2 e 4.3) used for their high accuracy and the symmetry conditions are applied.
The cross-section domain used in MUL^2 *CODE* is shown in fig. 4.4: the entire butt joint was divided into 8 rectangular elements and, so, an uniform mesh was used across the joint itself; an isotropic material was defined with no lamination. In order to simplify the problem, differently from Sawa, the forces acting on the joint studied with MUL^2 *CODE* were not deducted from a Fourier's expansion, but from a force grid only on the top face made by concentrated forces applied on the nodes **13**, **14**, **15**. Then, the joint has been clamped through z-axis on bottom face (nodes **1**, **2**, **3**), through x-axis across that plane (nodes **2**, **5**, **8**, **11**, **14**) and the 4^{th} node of the central node **8** was clamped through y-axis: this way of representation on MUL^2 *CODE* created a case of study equivalent to the Sawa's one (opposing forces on top and bottom faces); static analysis with MITC integration is performed. The entire analytical method used in MUL^2 *CODE* is shown only for this section: further analysis will be conducted with the same process.

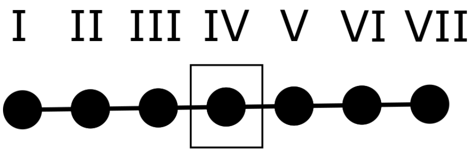

Figure 4.2: $2B4$: the central node used for analysis is highlighted.

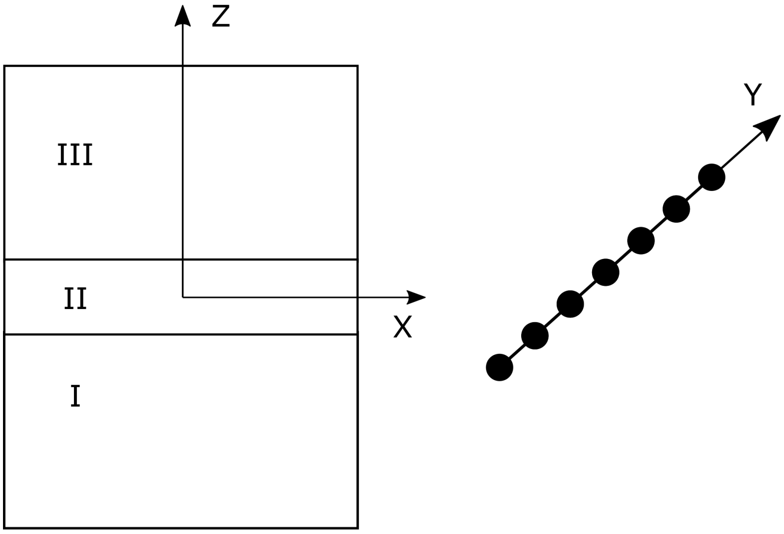

Figure 4.3: *MUL*^{2} *CODE* butt joint analysed. On the left, the butt joint is shown while, on the right, the $2B4$ through the thickness and y-axis.

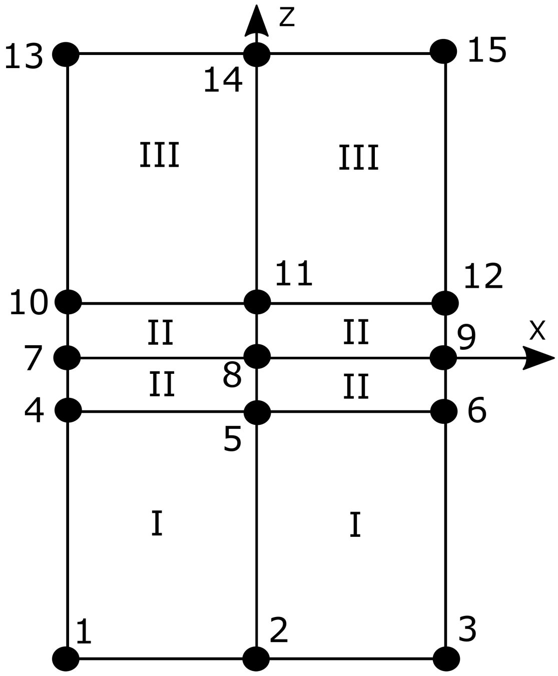

Figure 4.4: *MUL*^{2} *CODE* HLE discretization.

In tab. 4.2 the DOFs of polynomial expansion analysis is reported:

Model	**DOFs**
HLE 1	315
HLE 2	777
HLE 3	1239
HLE 4	1869
HLE 5	2667
HLE 6	3633
HLE 7	4767
HLE 8	6069

Table 4.2: DOFs - Butt joint.

The stress tension σ_{ym} corresponds to the value of tension in the interface of the section (at $z = h_2$); after normalising values by σ_{ym}, graphical results can be calculated (fig. 4.5, 4.6, 4.7):

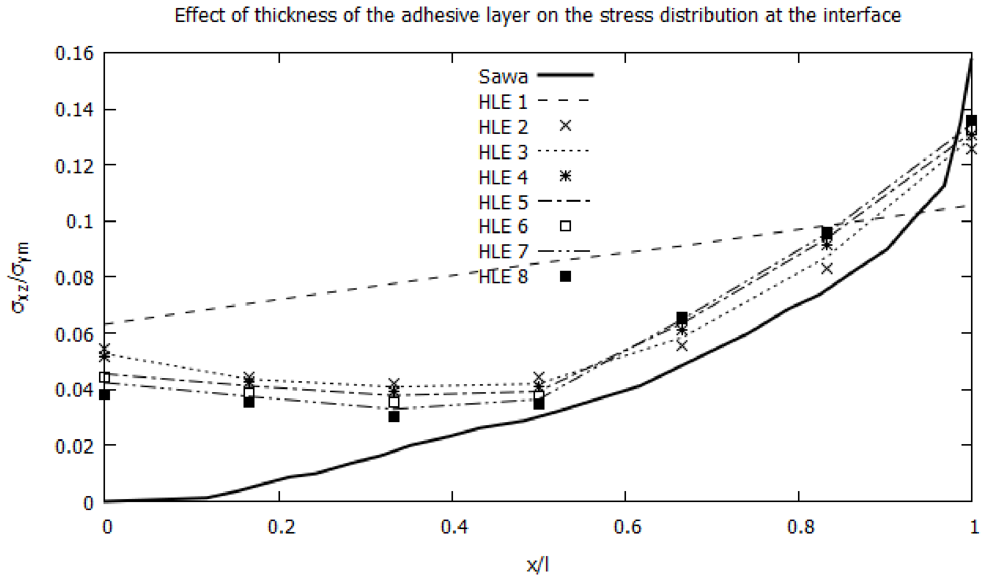

Figure 4.5: Stress σ_{xz} (Shear Stress) distribution - Adhesive butt joint.

As it is possible to see, results show the efficiency of MUL^2 *CODE* in capturing almost the same values of stresses of an analytical and, then, experimental computation[50] (the little gap between the two solutions is probably due to the different type of forces applied on the two joints): this comparison and matching between the MUL^2 *CODE* and this first literature result is used as validation in order to use the code for the analysis of the following lap joints.

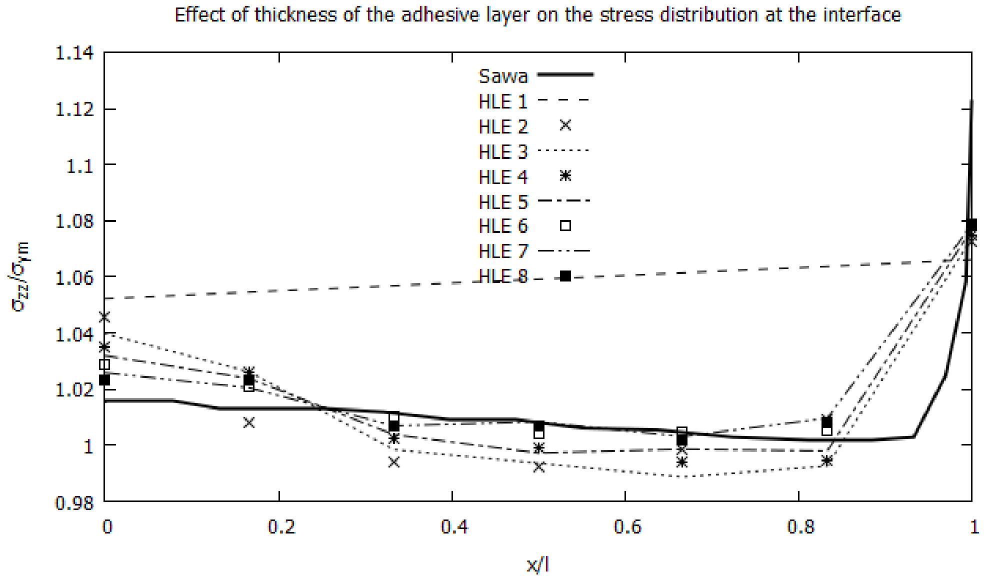

Figure 4.6: Stress σ_{zz} (Peel Stress) distribution - Adhesive butt joint.

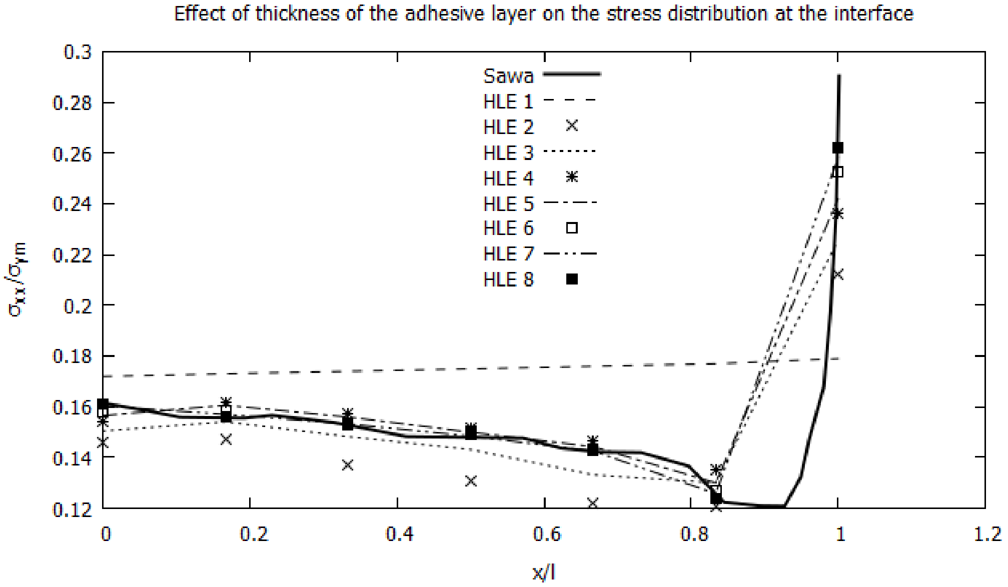

Figure 4.7: Stress σ_{xx} (Longitudinal Stress) distribution - Adhesive butt joint.

4.2 Single Lap Joint - MUL^2 ***CODE*** analysis

4.2.1 First Approach: cross axis

Using the MUL^2 *CODE*, two approaches can be adopted to model lap joints. The first one, hereinafter First Approach, allows to model structures placing the main axis through thickness, so, the y-axis of figure fig. 4.8 and fig. 4.9. This approach is useful to study the distribution of stresses, strains and other factors like temperature or crack development in thick plate which have loads applied both on upper and bottom face: in this way, in fact, the beam elements chosen will lean upon the cross axis detecting each single variations of the problem's unknowns.

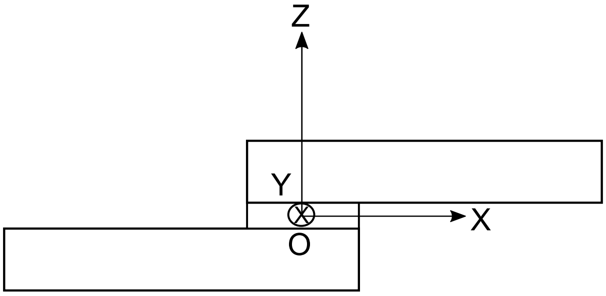

Figure 4.8: Single Lap Joint: cross-section.

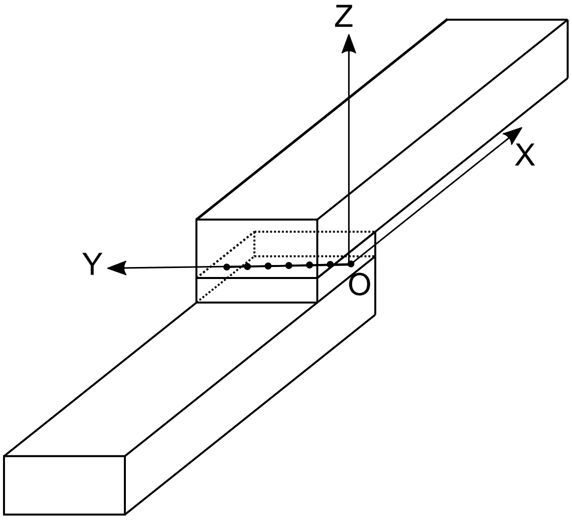

Figure 4.9: Single Lap Joint: 2B4 mesh.

Therefore, in the First Approach is possible to model and change the whole cross-section domain of the beam structure enabling the variation of the meshes while the beam element chosen remain the same. The pros and cons regarding the use of the First Approach are reported in the following lines. First of all, changing the mesh signifies change the entire model: even if the structure analysed is the same as before, a refined mesh is more complex to implement on the code because each time the connectivity matrix has to be changed and, in order to have the best precision which is expected from a graded mesh, the structure has to be divided into more and more elements to obtain an acceptable refined mesh; this means the change of the nodes on which loads and constraints are applied (and the following re-computation and reassignment of forces values on the nodes, if a grid force is used). However, this method allows to study single lap joints with different thickness only adding other structural nodes to the beam element and not changing the entire model: it can be used very well for composite plates because, when a composite layer is applied upon another one, the mesh can remain the same, while the new layer is investigated with the new beam element added to the previous one. Legendre polynomials are used from the 1^{st} until the 8^{th} order, enabling to achieve a prediction about the stress distribution more and more precise. In this section, results obtained by Vable & Maddi shown in the chapter 2 are compared to lap joints studied with MUL^2 *CODE* with uniform or graded meshes: respectively, Peel Stress refers to Mode **I** and Shear Stress refers to Mode **II** of deformation described in the previous chapter.

4.2.1.1 Uniform Mesh: Peel and Shear Stress results

The adhesive region has been initially studied with an uniform mesh (Fig. 4.10); adherends and adhesives are implemented with huge elements to evaluate the strength of the code and to compare results with the literature ones. On the adherends, two elements of 12.7 mm on the left and right extremity have been placed in order to recreate the same boundary conditions of [34] and, in fact, those nodes were clamped through z-axis (in [34] in these two region two carriages stop movements of the joint in the vertical direction); each 4^{th} node of the $2B4$ for every structural node of the connectivity is clamped through y-axis: this is the only possible way both to block movements in that direction and to respect the symmetry of the joint, giving an uniform y-boundary condition; horizontal translation is blocked with a x-constraint in the origin, i.e. the central node of the joint, not to affect the symmetrical distribution of stresses and strains.

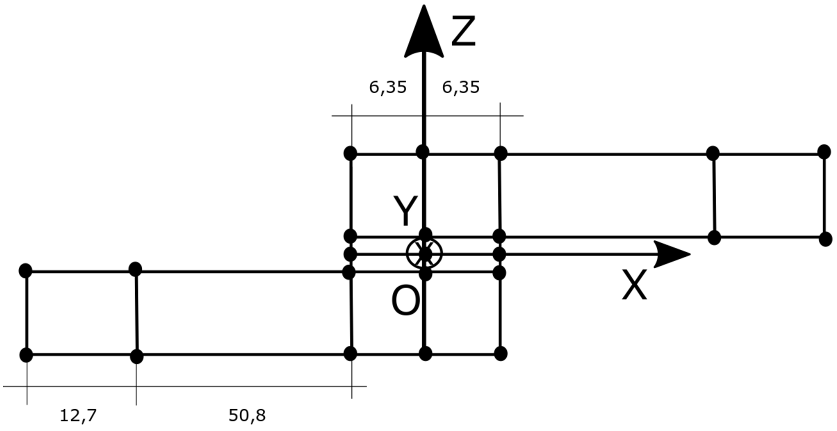

Figure 4.10: Uniform cross section HLE discretization [mm].

Loads are applied on the two external sides and a grid force made of 28 concentrated forces is applied on them, 14 on the nodes **I** of the $2B4$ creating the sides and the other 14 on the node **VII** of the $2B4$ (fig. 4.11). Static analysis with MITC integration is used.

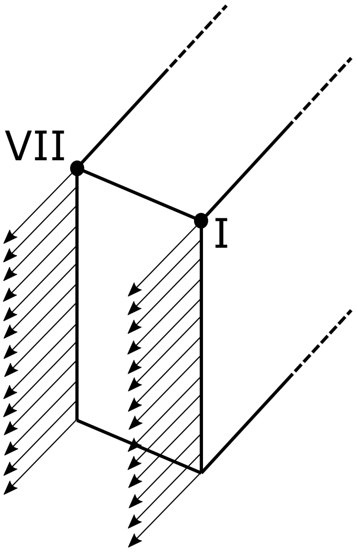

Figure 4.11: Grid force used both on left side (the same grid has been made on the right side).

Model	**DOFs**	**Peel Stress**	**Shear Stress**
HLE 1	483	0.0496	0.3144
HLE 2	1197	0.1453	0.5021
HLE 3	1911	0.3106	0.6829
HLE 4	2877	0.3417	0.6672
HLE 5	4095	0.3591	0.5999
HLE 6	5565	0.3607	0.6466
HLE 7	7287	0.3576	0.6315
HLE 8	9261	0.3499	0.6132
Vable & Maddi	/	0.8099	0.5099

Table 4.3: DOFs and Max values of Peel and Shear stress at the free edges - Single Lap Joint: uniform mesh (1^{st} approach).

Peel and Shear Stress at the beginning and at the end of the adhesive region ($x_1 = -6.35\,\mathrm{mm}$ and $x_2 = 6.35\,\mathrm{mm}$) have the same values because of geometrical, load and constraint symmetry (tab. 4.3). For Peel Stress (fig: 4.12), the peaks in adhesive region is due to the concentration of stress and the difference between the literature solution and MUL^2 *CODE* in the peak value at the extremity is evident: this because, as seen before, the mesh created in the adhesive region in [34] is made only by one single element through all the adhesive zone (fig . 1.11), while the uniform mesh of the software contains 4 elements, providing more precise results even if the mesh is coarse. The increment of the expansion order is clear in the two figures: from a linear shape function (HLE 1) which can not fit well even the shape function of literature, to the HLE 3 and higher orders which maintain the shape function of literature, but converge to unique results. In the lowest peaks Peel stress is negative and this situation describes a compression area: the equality of loads at the extremity provokes a bending of the lap and a resulting redistribution of stresses in adherends which determine the new, even very little, buckling. Shear Stress (fig. 4.13) has a parabolic shape and, as opposed to Peel Stress, from the 2^{nd} to 8^{th} polynomial order values found by MUL^2 $CODE$ are bigger than literature: this result is due to the different mesh which in [34] underestimates the peaks. The lowest point of transversal stress, as it is expected, leans in the centre of the adhesive because of symmetrical loads and constraints applied on the lap.

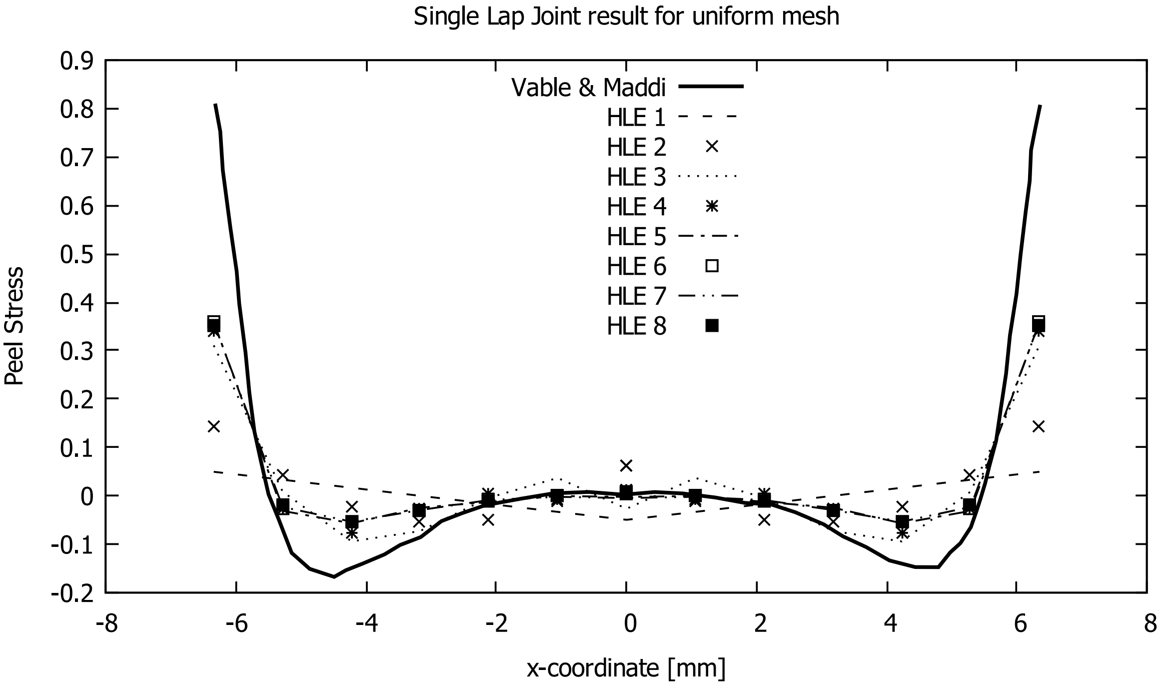

Figure 4.12: Peel Stress - Single Lap Joint: uniform mesh (1^{st} approach).

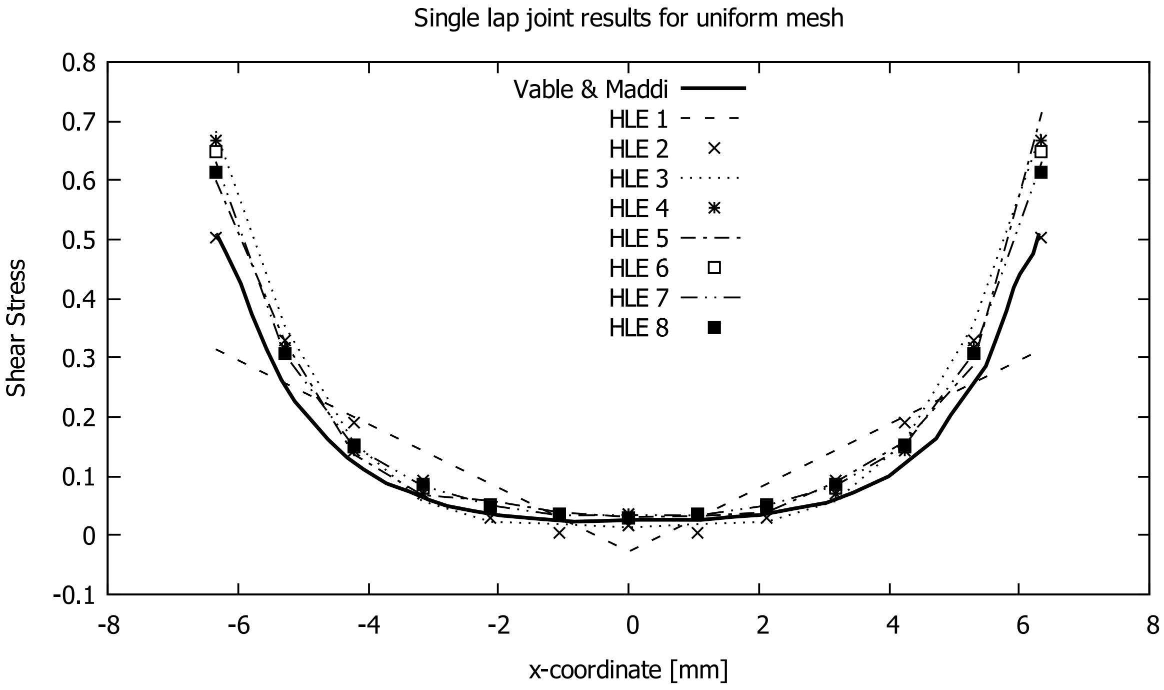

Figure 4.13: Shear Stress - Single Lap Joint: uniform mesh (1^{st} approach).

4.2.1.2 First Graded Mesh: Peel and Shear Stress results

In this section, the study will be leaded by using a first graded mesh (fig. 4.14). Adhesive is divided into 8 rectangular mesh elements (thus, redoubling the number of mesh elements than the previous case) of which 4 are placed next to the free edges of the adhesive zone in order to enrich that region and provide better and better fitting of results. The boundary conditions and the distribution of loads are the same as the previous section, after regenerating the mesh and adding the new points created on the adhesive region.

Peel and Shear Stress (fig. 4.15, 4.16) at the beginning and at the end of the adhesive region ($x_1 = -6.35\,\text{mm}$ and $x_2 = 6.35\,\text{mm}$) have the same values because of geometrical, load and constraint symmetry. For Peel Stress the convergence to an unique solution appears from the lowest expansion orders and also the compression zone is low enhanced and, so, the new refined mesh achieves its aim. Shear Stress shows a particular shape in the free edges, only detected by the HLE orders from 6^{th} to 8^{th}: the stress begins negative (compression area) and in very few millimetres it reaches great values; the mesh used in MUL^2 *CODE* should be refined another time in order to describe this behaviour also with lowest Legendre's expansion orders because the computational cost, as we can see form the table with numbers of DOFs, seriously increases (tab. 4.4).

Model	**DOFs**	**Peel Stress**	**Shear Stress**
HLE 1	693	0.1859	0.4726
HLE 2	1785	0.1736	0.5731
HLE 3	2877	0.4368	0.6452
HLE 4	4389	0.4008	0.6022
HLE 5	6321	0.3755	0.5309
HLE 6	8673	0.3523	0.4309
HLE 7	11445	0.3370	0.3121
HLE 8	14637	0.3149	0.1925
Vable & Maddi	/	0.8925	-0.1434

Table 4.4: DOFs and Max values of Peel and Shear stress at the free edges - Single Lap Joint: first graded mesh (1^{st} approach).

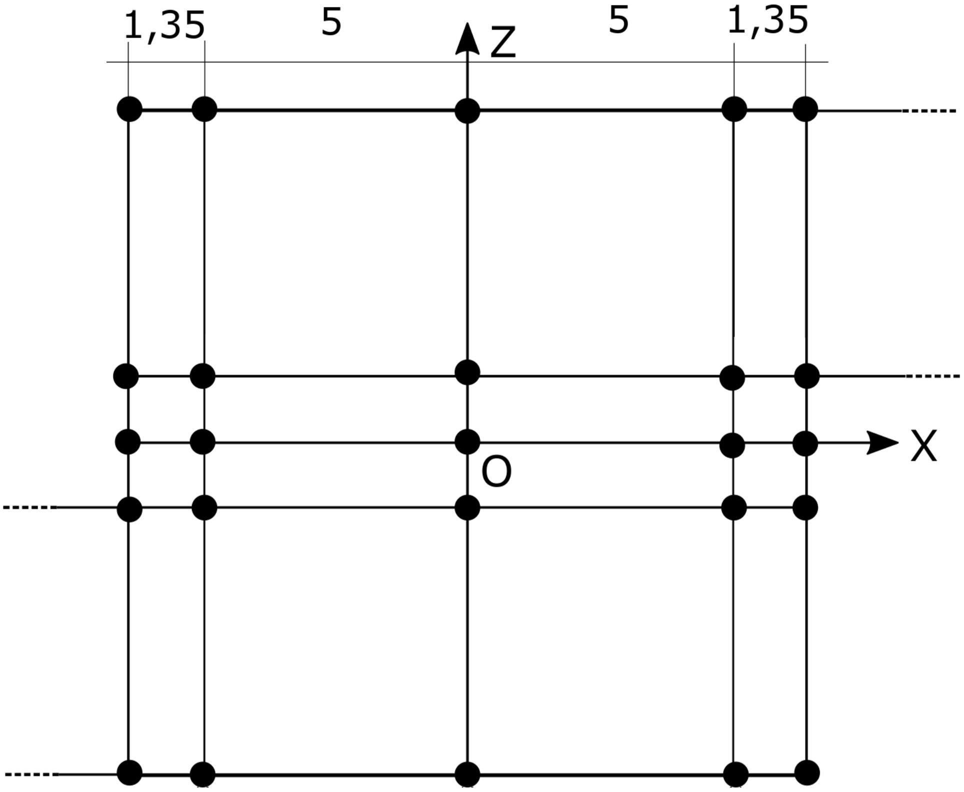

Figure 4.14: First Graded Mesh cross section HLE discretization [mm].

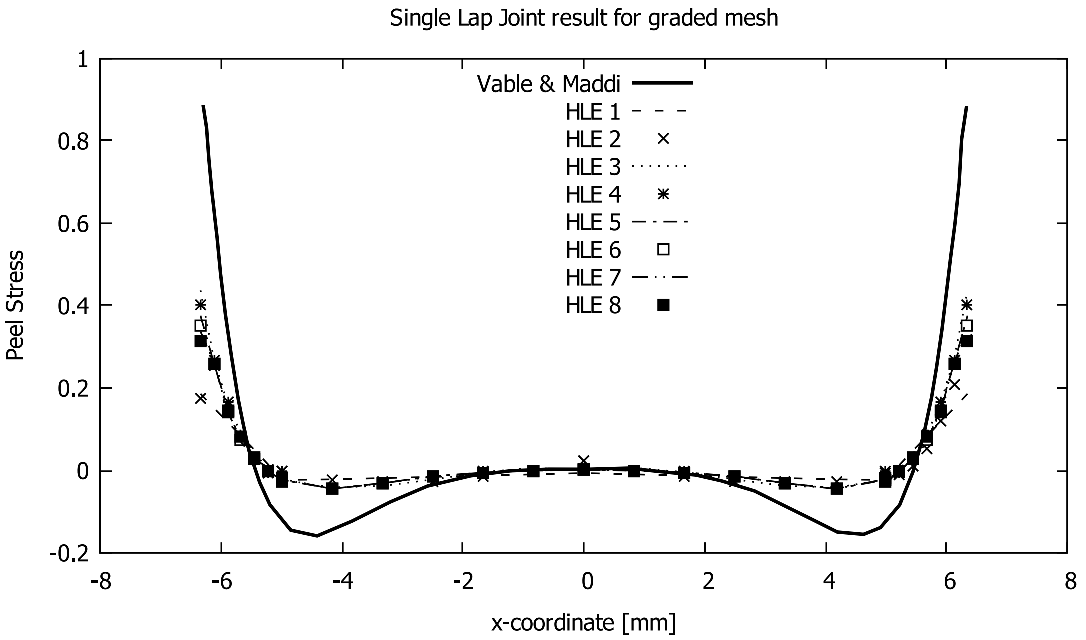

Figure 4.15: Peel Stress - Single Lap Joint: first graded mesh (1^{st} approach).

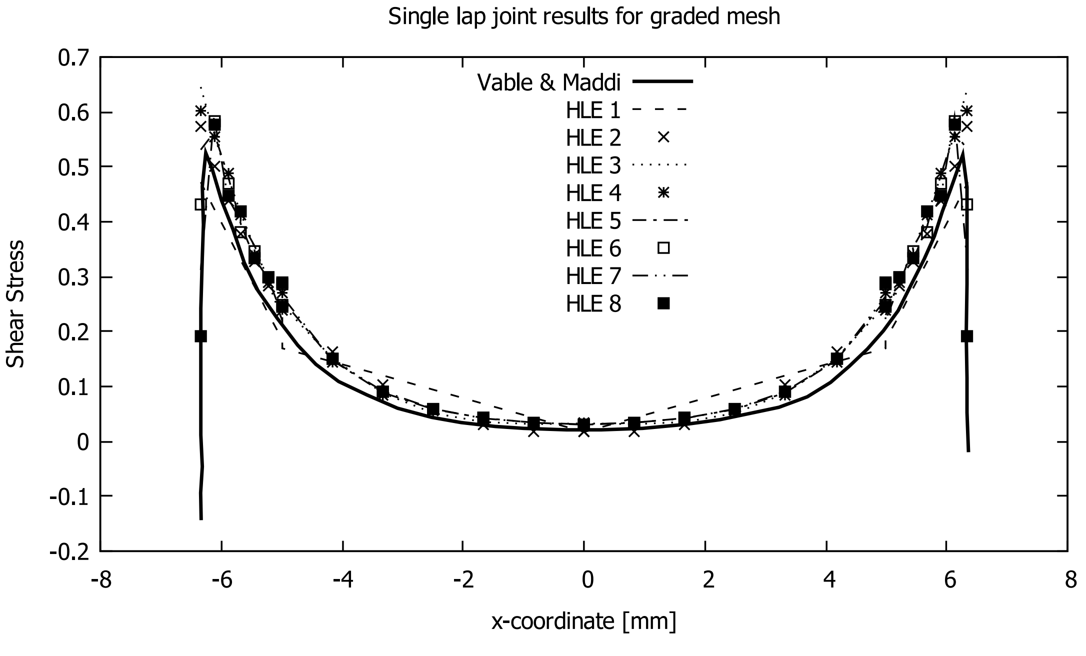

Figure 4.16: Shear Stress - Single Lap Joint: first graded mesh (1^{st} approach).

4.2.1.3 Second Graded Mesh: Peel and Shear Stress results

The last mesh used to study the single lap is shown below (fig. 4.17). Adhesive is divided into 12 rectangular mesh elements so redoubling the number of mesh elements leaning in the adhesive than the previous analysis: these ones are 0.35 mm long and they can easily investigate the free edges, but on the contrary the computational cost (tab. 4.5) and the complexity of creating the model increase very fast.

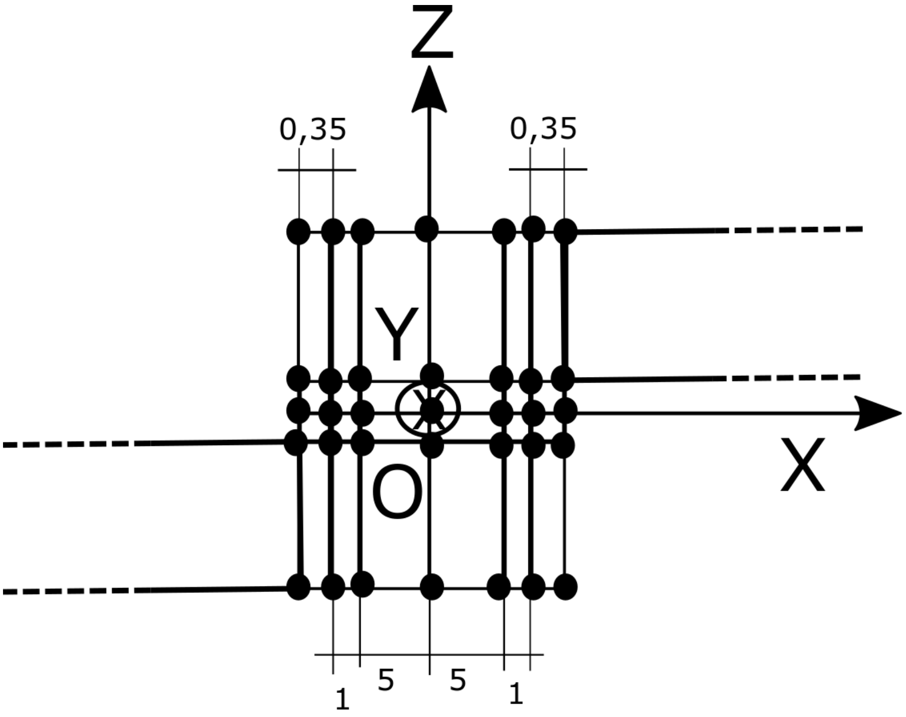

Figure 4.17: Second Graded Mesh cross section HLE discretization [mm].

Model	DOFs	Peel Stress	Shear Stress
HLE 1	903	0.2337	0.48
HLE 2	2373	0.2925	0.5221
HLE 3	3843	0.3696	0.4225
HLE 4	5901	0.3381	0.1662
HLE 5	8547	0.2991	-0.0304
HLE 6	11781	0.2603	-0.104
HLE 7	15603	0.2449	-0.0969
HLE 8	20013	0.2419	-0.0652
Vable & Maddi	/	0.8925	-0.1434

Table 4.5: DOFs and Max values of Peel and Shear stress at the free edges - Single Lap Joint: second graded mesh (1^{st} approach).

Peel and Shear Stress at the beginning and at the end of the adhesive region ($x_1 = -6.35\,\text{mm}$ and $x_2 = 6.35\,\text{mm}$) have the same values because of geometrical, load and constraint symmetry. For Peel Stress (fig: 4.18) the convergence to an unique solution appears from the lowest expansion orders (as before) and also the 1^{st} expansion order can fit better the shape of the stresses of the other higher orders. As we can see, the Shear Stress (fig. 4.19) can be now investigated with lower Legendre's expansion orders (from the 4^{th}) which manages to reach notable results at low DOFs and, so, low complexity of the model, which is the main aim pursued by *MUL^2 CODE*.

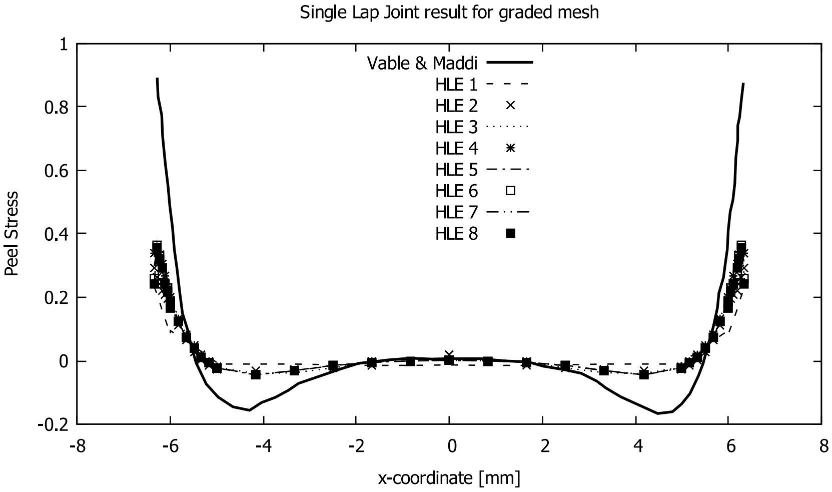

Figure 4.18: Peel Stress - Single Lap Joint: second graded mesh (1^{st} approach).

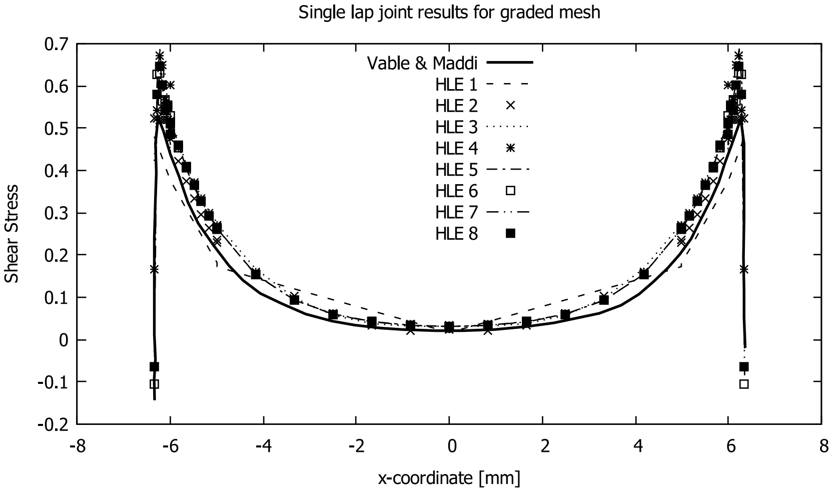

Figure 4.19: Shear Stress - Single Lap Joint: second graded mesh (1^{st} approach).

4.2.2 Second Approach: longitudinal axis

The second version of MUL^2 *CODE* is called Second Approach and, in opposite to the previous one, it allows to model structures whose main axis is through the main dimension of the beam, so, the y-axis of fig. 4.20. This approach is the most usual way to study beam elements because it models the beam as the classical beam theories described (EBBT and Timoshenko) and, for this reason, this version will be used when in the following sections a comparison with MUL^2 *CODE* will be needed.

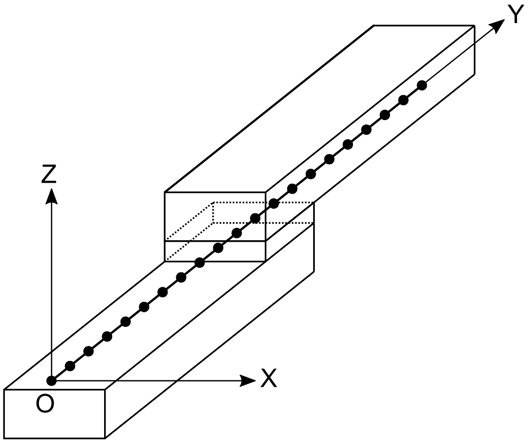

Figure 4.20: Single Lap Joint: 2B4 mesh.

In the Second Approach is possible to model and change the number, the type and the distance between the nodes of beam elements chosen, while the meshes and the whole connectivity of the structure remain the same. This tool allows creating models with variable sections through the axis and also more complex lap (as double lap joint) can be created easily (each section will have its own connectivity file which describes its material and geometrical properties, fig. 4.21).

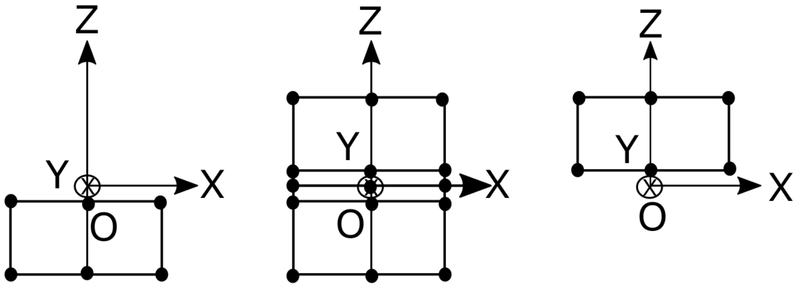

Figure 4.21: Single Lap Joint: cross-sections. From left: bottom adherend, the adhesive central zone and the top adherend.

In fact, after creating a simple mesh as for uniform case studied before, it's possible to achieve better precision only enriching the number of nodes of the beam elements and, for

that reason, the mesh will be the same in the following analysis, only the discretization on the axis will be changed. This version allows also to impose boundary conditions and loads as if they were an unique entity and, in fact, the input file is the same or them: an entire plane blocking or with forces applied on it can be created on the nodes of the beam element (i.e. using the coordinates of the main axis) and this is a more uniform way to apply loads than the grid force; as a consequence, from the lowest order expansions the shape of the function proposed by [34] should be fitted.
Legendre polynomials are used from the 1^{st} until the 8^{th} order, enabling to achieve a prediction about the stress distribution more and more precise. In this section, results obtained by Vable & Maddi shown in the chapter 2 are compared to lap joints studied with MUL^2 *CODE* with uniform or graded meshes: respectively, Peel Stress refers to Mode **I** and Shear Stress refers to Mode **II** of deformation described in the previous chapter.

4.2.2.1 Uniform Mesh: Peel and Shear Stress results

The axis of the single lap has been initially modelled with an uniform mesh, thus the shape and the distance between each node of the beam elements are the same (4.23 mm totalling 43 nodes on the entire length of the axis). For the first two regions long 12.7 mm on both the extremities, $1B4$ element is used to apply both loads and boundary conditions through z-axis; each node of the $B4$ elements used have been clamped with planes through x-axis: this is the only possible way both to block movements in that direction and to respect the symmetry of the joint; horizontal translation is blocked with a y-constraint in the central node of the joint, not to affect the symmetrical distribution of stresses, strains and loads, applied as planes on the external $1B4$ nodes. Static analysis with MITC integration is used.

Model	**DOFs**	**Peel Stress**	**Shear Stress**
HLE 2	2613	0.3325	0.6336
HLE 3	4101	0.3669	0.6337
HLE 4	6081	0.3414	0.6554
HLE 5	8553	0.3616	0.6323
HLE 6	11517	0.3559	0.6602
HLE 7	15000	0.3571	0.6374
Vable & Maddi	/	0.8099	0.5099

Table 4.6: DOFs and Max values of Peel and Shear stress at the free edges - Single Lap Joint: uniform mesh (2^{nd} approach).

Peel and Shear Stress at the beginning and at the end of the adhesive region ($y_1 = 63.5 mm$ mm and $y_2 = 76.2$ mm) have the same values because of geometrical, load and constraint symmetry. Both for Peel and Shear Stress (fig. 4.22, 4.23) the convergence to an unique solution appears from the lowest expansion orders and this means a solid modelling and code implementation even if the DOFs (tab. 4.6) and, so, the complexity of the model, is significantly huger.

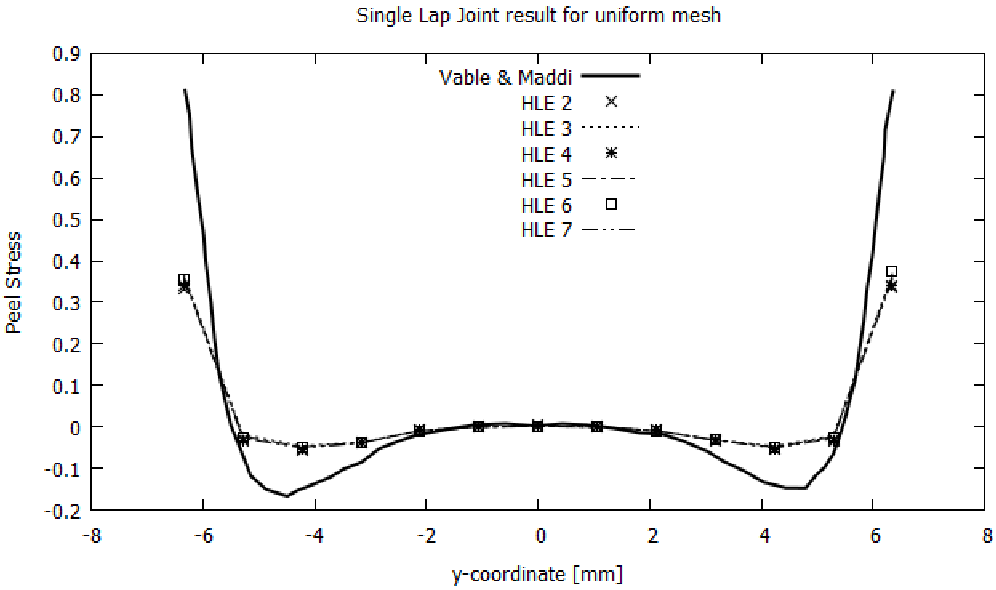

Figure 4.22: Peel Stress - Single Lap Joint: uniform mesh (2^{nd} approach).

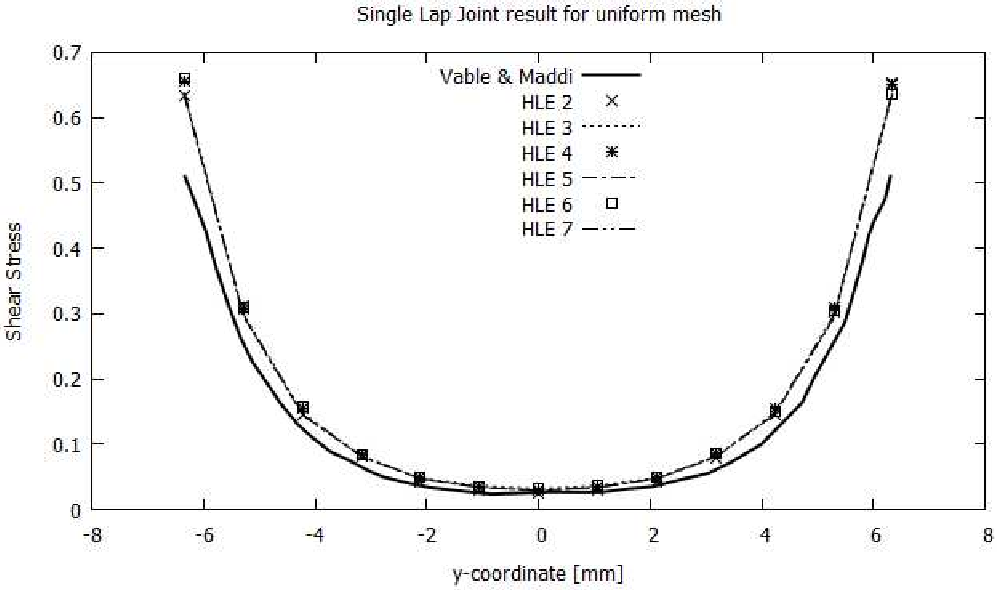

Figure 4.23: Shear Stress - Single Lap Joint: uniform mesh (2^{nd} approach).

4.2.2.2 Graded Mesh: Peel and Shear Stress results

In this section, the axis of the single lap is no more regularly spaced, but thicker beam elements will be used graded mesh: the distance between each node of the beam elements is the same 4.23 mm except for the free edges on adhesive region, in which the distance between each node is 0.11 mm, totalling 49 nodes on the entire length of the axis. As the previous case, for the first two regions long 12.7 mm on both the extremities, $1B4$ element is used to apply both loads and boundary conditions through z-axis; each node of the $B4$ elements used have been clamped with planes through x-axis: this is the only possible way both to block movements in that direction and to respect the symmetry of the joint; horizontal translation is blocked with a y-constraint in the central node of the joint, not to affect the symmetrical distribution of stresses, strains and loads, applied as planes on the external $1B4$ nodes. Static analysis with MITC integration is used.

Model	**DOFs**	**Peel Stress**	**Shear Stress**
HLE 2	3279	0.307	0.186
HLE 3	5163	0.299	0.170
HLE 4	7683	0.281	0.177
HLE 5	10839	0.307	0.172
HLE 6	14634	0.299	0.177
HLE 7	19071	0.32	0.18
Vable & Maddi	/	0.8925	-0.1434

Table 4.7: DOFs and Max values of Peel and Shear stress at the free edges - Single Lap Joint: graded mesh (2^{nd} approach).

Both for Peel and Shear Stress (fig. 4.24, 4.25) the convergence to an unique solution appears from the lowest expansion orders and the increased density of points is due to the bigger number of nodes than the uniform axis case; because of geometrical, load and constraint symmetry, Normal and Shear Stress at the beginning and at the end of the adhesive region ($y_1 = 63.5mm$ mm and $y_2 = 76.2$ mm) have the same value. As we can see, the code is able to balance the computational cost (tab. 4.7) due to this simulation with a more precise values of stresses achieved from 2^{nd} expansion order towards the higher ones.

The *MUL^2 CODE* allows to export data with the graphic software *Paraview*: in fig. 4.26 and 4.27, the stress concentration in the adhesive region (respectively for top and bottom adherend interfaces) evaluated across the longitudinal axis y is shown.

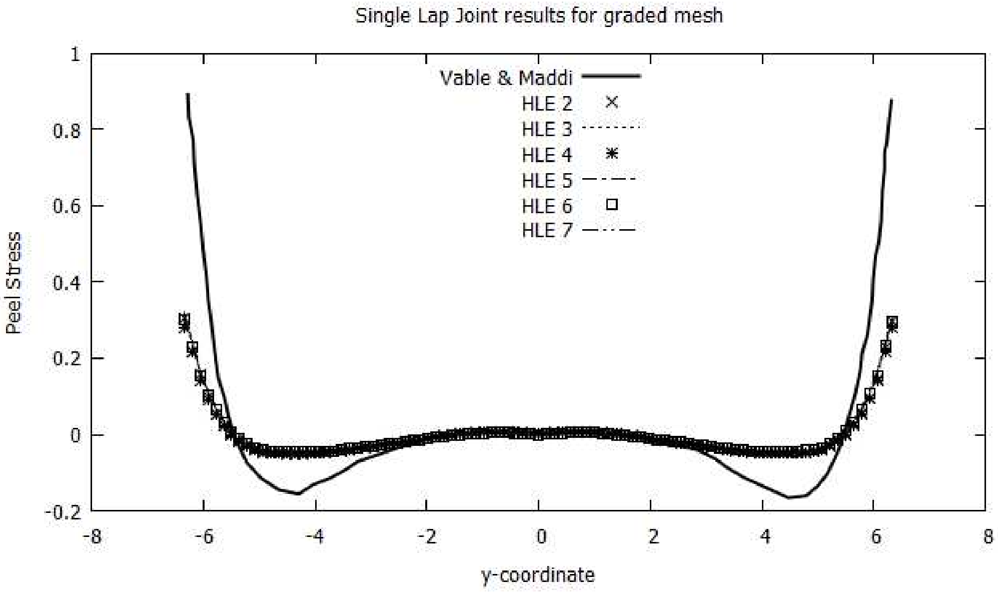

Figure 4.24: Peel Stress - Single Lap Joint: graded mesh (2^{nd} approach).

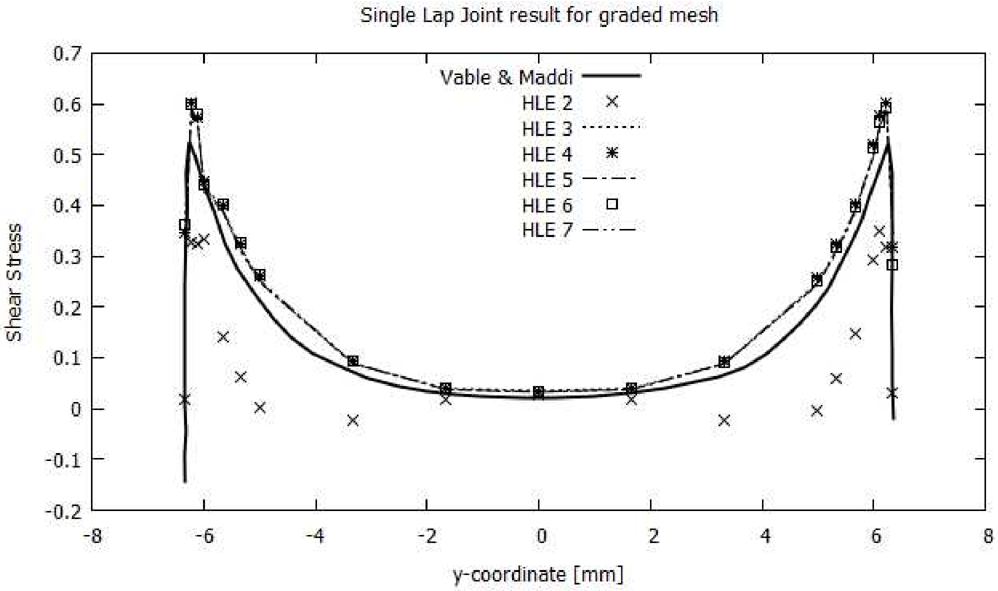

Figure 4.25: Shear Stress - Single Lap Joint: graded mesh (2^{nd} approach).

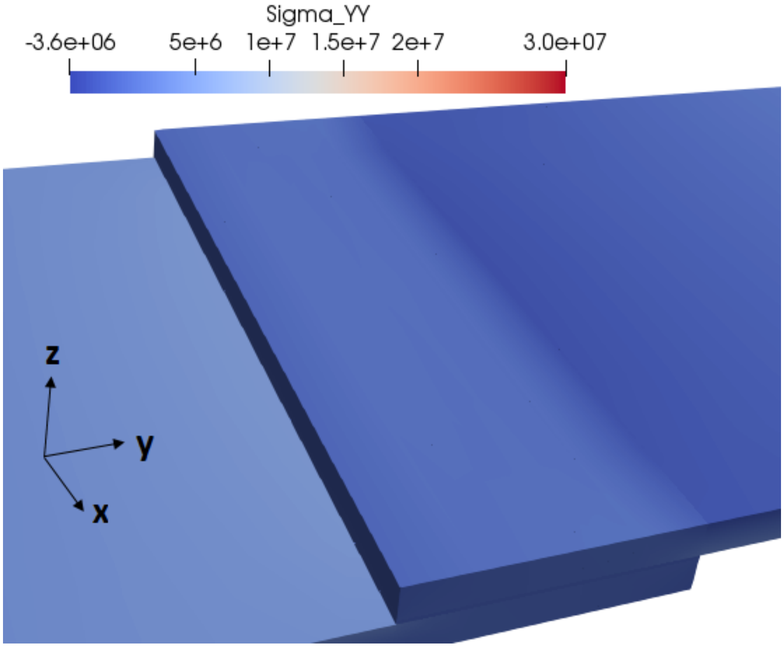

Figure 4.26: Stress distribution across the longitudinal axis y for interface between bottom adherend and adhesive.

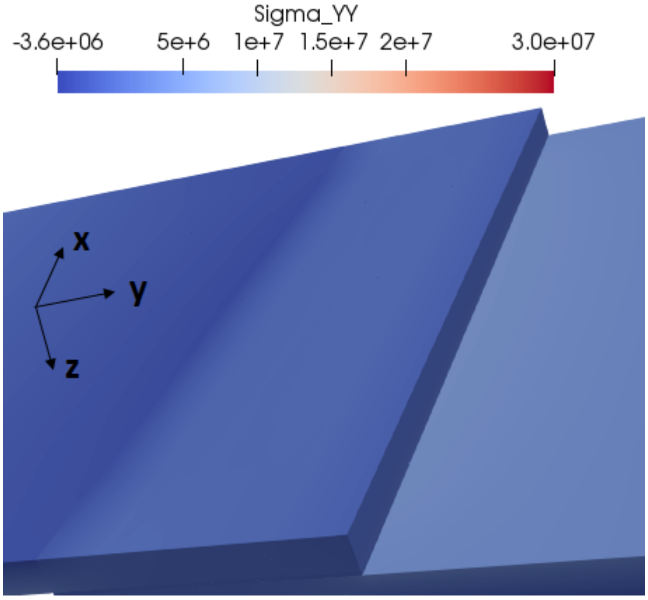

Figure 4.27: Stress distribution across the longitudinal axis y for interface between top adherend and adhesive.

4.2.3 ABAQUS validation

Results obtained with the MUL^2 *CODE* and the commercial finite element package ABAQUS are compared; ABAQUS models created are (tab. 4.8):

- *Model-1*: each part was assumed as a deformable 2D Planar shell type, CPE8 elements were used for the mesh (8-node biquadratic plain strain quadrilateral elements); mesh control of the adhesive's region is made through a linear decrease of the size of mesh elements (from 0.795 mm on the middle of the adhesive to 0.0795 mm at the free edges); adhesive's thickness is discretized into 4 mesh elements
- *Model-2*: adhesive was assumed as a deformable 3D solid part, SC8R were used for the mesh (8-node quadrilateral in-plane general-purpose continuum shell, reduced integration, finite membrane strains); top and2 bottom adherends were assumed as deformable 3D shell parts, S8 elements were used for the two parts; mesh control of the adhesive's region is made through a linear decrease of the size of mesh elements (from 0.795 mm on the middle of the adhesive to 0.0795 mm at the free edges); adhesive's thickness is discretized into 2 mesh elements

Model	**Adherends**		**Adhesive**	
	Number	**Type**	**Number**	**Type**
Model 1 GLA	324	CPE8	160	CPE8
Model 1 GNL	324	CPE8	160	CPE8
Model 2	800	S8	1600	SC8R

Table 4.8: Mesh properties - ABAQUS validation.

All the mesh used in the previous models use the hourglass control and stresses are calculated in the integration points. The materials used for analysis have equivalent mechanical properties as [34] and MUL^2 *CODE*, such as the Young's modulus $E = 69000$ Pa and the Poisson's ratio ν equal to 0.32 for the adherends (which is assumed as a simple isotropic material) and $E = 3000$ Pa and $\nu = 0.36$ for the adhesive, assumed as an isotropic material too: the Young's modulus are not expressed in GPa because the three models are created using the millimetres scale of length. On the both extremities of the adherends of the three models, concentrated forces applied on the mesh point act of respectively -150 N on the left side and 150 N on the right side: this leads to an almost equivalent loading field as the code and [34]. Vertical displacements are blocked with carriages on the adherends (recreating the two elements of 12.7 mm on the left and right extremities) and, as seen in pag. 65, the central node of the structure is clamped in the horizontal direction in order to implement the exact equivalent boundary conditions as the previous models. The ABAQUS models properties are summarized in the following table and compared to MUL^2 *CODE* HLE 7 "Second Approach: longitudinal axis" (pag. 64, tab. 4.9):

The extreme peaks for Peel and Shear stress in Model-1 shows divergences from the literature and MUL^2 *CODE*: the great drops of stress is due to the 2D Planar shell type used for analysis which does not perform very well at the extremities if a geometrical linear

Property	**Model-1 GLA**	**Model-1 GNL**	**Model-2**	**HLE 7**
Elements	808	808	3200	16
Nodes	2855	2855	4365	49
DOFs	5710	5710	18441	19062

Table 4.9: DOFs - Single Lap Joint: ABAQUS validation.

analysis (GLA) is carried out; a comparison with analysis including non-linear effects at the extremities (Geometrical Non Linearity, GNL) is highlighted in fig. 4.28:

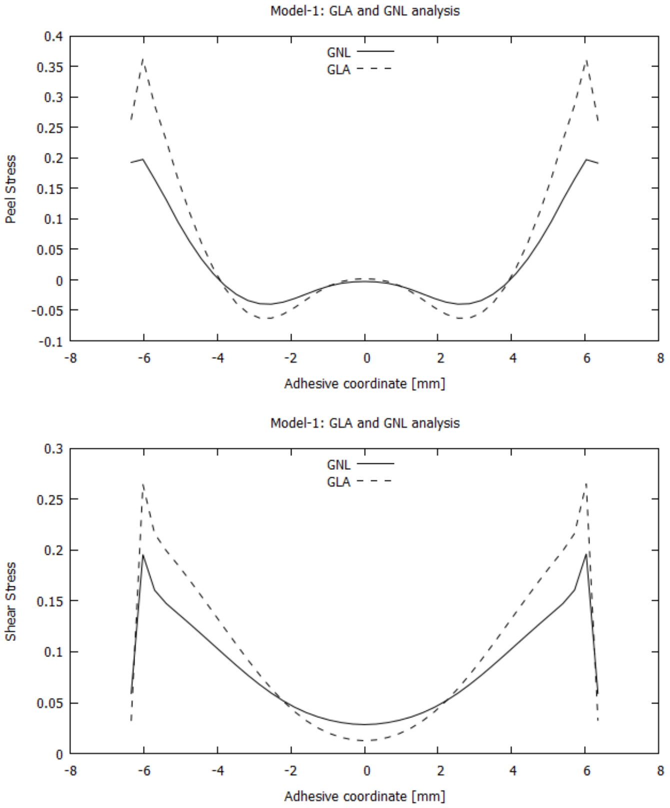

Figure 4.28: Peel (top) and Shear (bottom) stress evolution for 2D Planar shell type elements using linear analysis (GLA, dashed line) and including non-linearities at the extremities (GNL, solid line).

Below, results for M. Vable & J. Maddi[34], MUL^2 *CODE* and the commercial finite element package ABAQUS are shown (fig. 4.29, 4.30): the Model-2 is that one which is able to model the single lap at best because 3D shell type can describe a solid element with very thin thickness and, for that, it will be taken as reference for the complete validation of MUL^2 *CODE*; for Model-1, the GNL analysis is presented. As it's possible to see, even it has almost the same shape, the code is not so precise in detecting the values on the free edges and, in fact, the gap between code's and Model-2's solution is almost 0.1 which is probably due to the different meshes in that region (uniform on the cross-section for the code and well refined with linear decreasing for Model-2) and, also in the compression region, the code provides higher values than the ABAQUS model: a refinement of the mesh of the cross-section in the code is necessary. For Shear stress, the code has almost a mean value between [34] and Model-2 and, as told before, it can not reach the same values of stresses studied by ABAQUS model: except for these gaps, the code can be considered solid and accurate, although it is recommended to refine not only the mesh of the axis, but also changing the cross-section's one in order to provide more and more precise results not detectable with a coarse mesh on the cross-section, even if the axis is very refined meshed as that one used for this comparison.

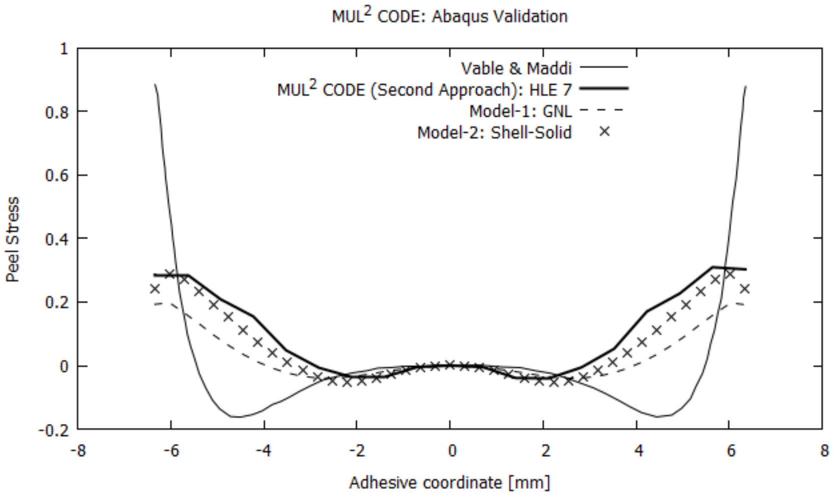

Figure 4.29: Peel Stress - ABAQUS validation.

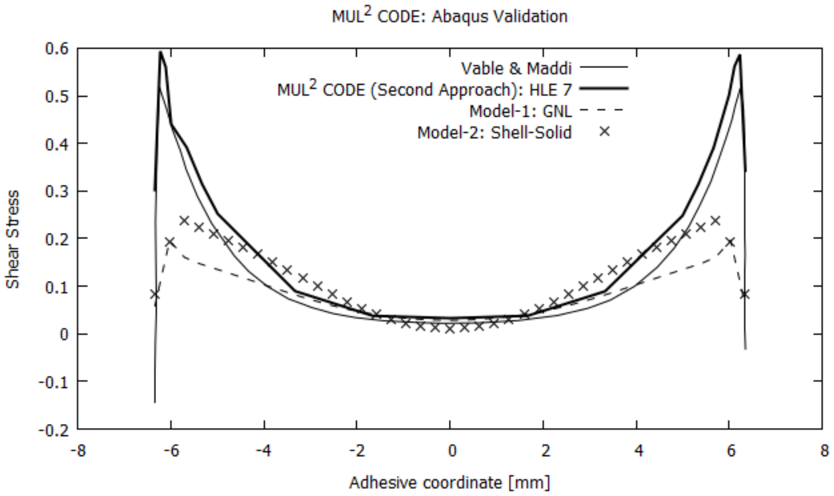

Figure 4.30: Shear Stress - ABAQUS validation.

4.3 Single Lap Joint - ABAQUS analysis

4.3.1 Parametric Study

As seen in the previous section, analysis of peaks values at the extremities for both Peel and Shear stresses can exhibit deviations from the attended results if only linear study is performed; in order to understand the behaviours of different laps in the simplest possible way, a parametric study was performed using a *Python* code to extend the possible cases of study. Single Lap Joint was created with an unique 3D deformable solid extrusion part sectioned into three elements (Bottom Adherend, Adhesive and Top Adherend) to which two different sections (and, so, two different materials) were assigned. Bottom and Top Adherend, then, were sectioned into three cells: two cells for the adhesive zone (with opposite direction for mesh bias ratio to achieve the best precision on the adhesive's free edges) and one external cell whose mesh bias ratio is oriented towards the adhesive zone in order to increase the number of mesh elements in the study zone; the mesh type used for the following analysis is C3D8, the default ABAQUS mesh type for solid parts. Parameters setted include:

- Geometrical and mechanical characteristics of both Adherends and Adhesive
- Type of mesh and number of mesh elements on every elements' edges (length, height and depth)
- Boundary Conditions
- Output and Analysis settings

First of all, some tests of convergence of the parametric code were made to assure solidity and stability of the models created with it; then, it was used to create four Single Lap Joints with the same geometry and materials characteristics of [34], but with different numbers of plies through the thickness of the adherends (1, 2, 4 or 6 plies: tab. 4.10): the aim is the study of linear/non-linear (GLA/GNL) behaviours (fig. 4.31, 4.32).

Model	**Adherends**		**Adhesive**	
	Number	**Type**	**Number**	**Type**
1 ply	1000	C3D8	400	C3D8
2 plies	2000	C3D8	400	C3D8
4 plies	26400	C3D8	10560	C3D8
6 plies	239600	C3D8	143760	C3D8

Table 4.10: Mesh properties - Parametric study.

The evolution of Peel and Shear Stress is shown below (fig. 4.33, 4.34): 1 element adherends is almost the same as [34] in both Peel and Shear stress, demonstrating from one side the modelling weakness of this configuration, but from the another convergence of the Python code to the literature results (for "4 elements" the non-linear analysis is

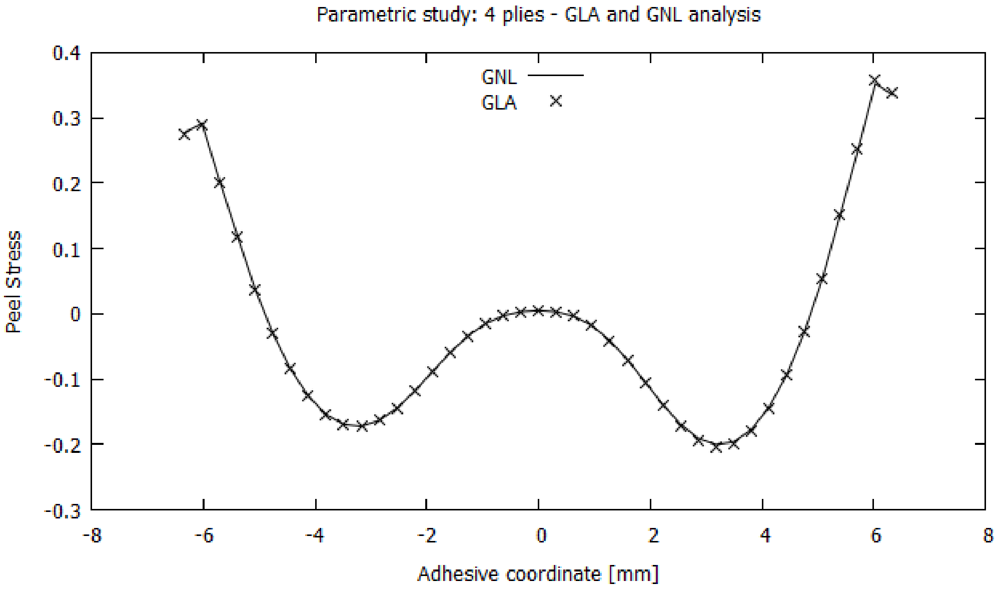

Figure 4.31: Peel Stress - linear (GLA)/non linear(GNL) analysis (Parametric study).

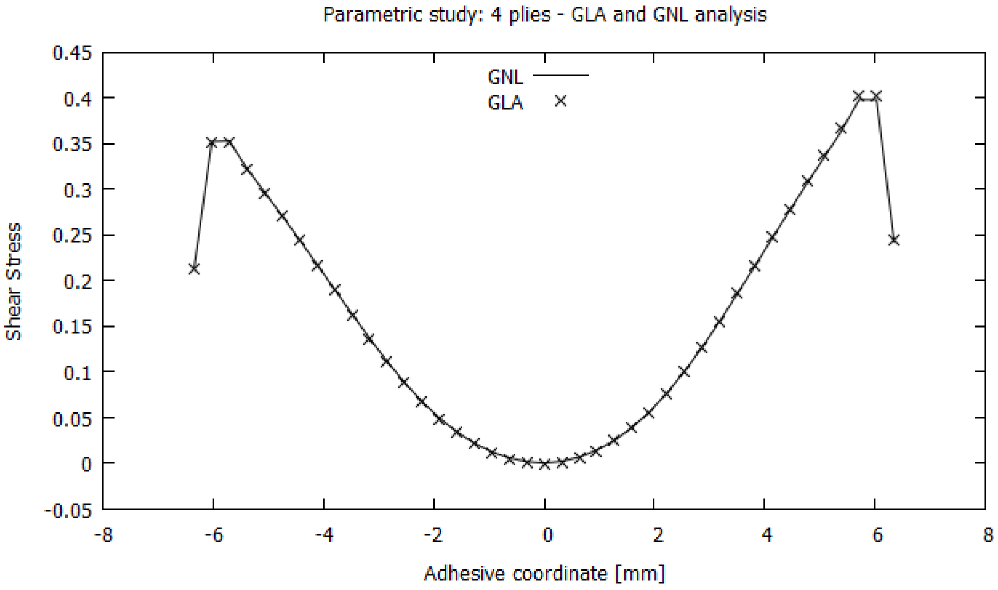

Figure 4.32: Shear Stress - linear (GLA)/non linear(GNL) analysis (Parametric study).

presented). At the free edges, the critical zones, the parametric models exhibit similarities to MUL^2 *CODE*, capturing the same shape even with lower values.

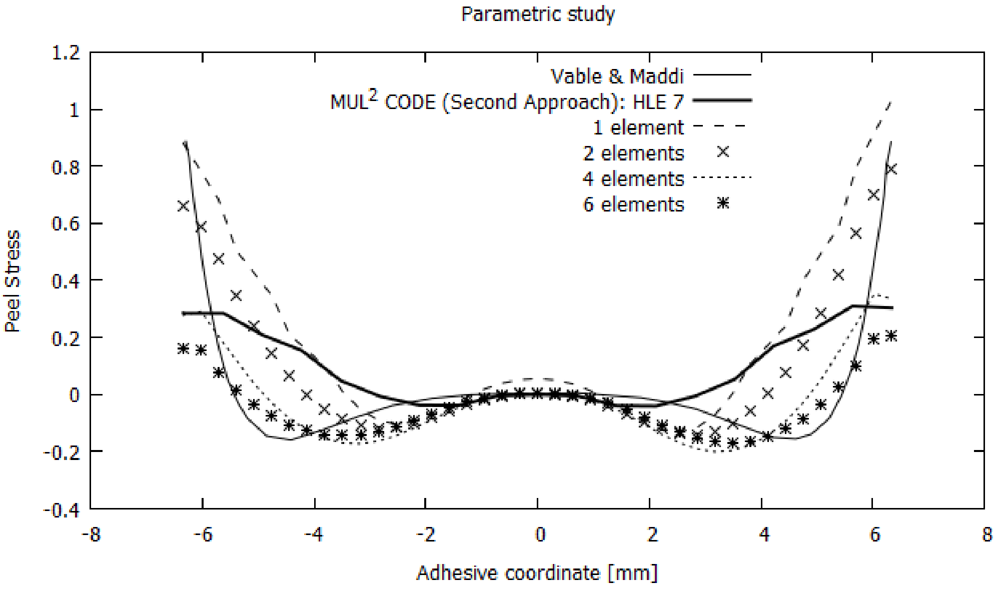

Figure 4.33: Peel Stress - Parametric study.

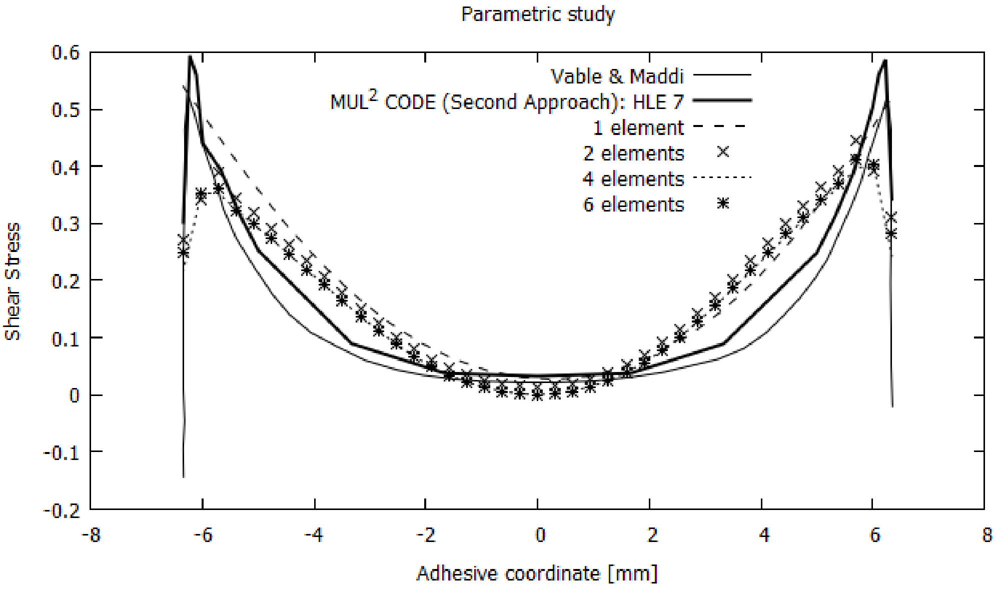

Figure 4.34: Shear Stress - Parametric study.

4.3.2 Damage study: cohesive elements

In this section, the adhesive is no longer modelled in ABAQUS as a solid homogeneous part, but, in order to study the behaviour of crack propagation, it is described as a cohesive element with an energetic damage evolution law and elastic traction characteristics with the following physical and mechanical properties:

Elastic Properties	**Cohesive element**
E_1 [GPa]	1.83
G_1 [GPa]	1.9
G_2 [GPa]	1.8

Table 4.11: Cohesive element: material properties.

The adherends are defined as solid shell planar homogeneous parts and meshed with 4 or 8 elements across the thickness (tab. 4.12) to analyse the evolution and diffusion of Peel and Shear stress with two different configurations from the adhesive through the adherends until the top and bottom faces of the top and bottom adherends, respectively: this was made to simulate an experiment in which on the faces of the two adherends some strain gauges have been applied. Concentrated forces applied on the mesh point act of respectively -150 N on the left side and 150 N on the right side (to keep an almost equivalent loading field as the code and [34]) with a tabular amplitude and on the interfaces between adherends and adhesive a no friction property with hard contact has been imposed not to affect the results with friction interaction between those surfaces; the models have been studied with dynamic implicit analysis and a time period of 60 steps corresponding to a minute of testing during which the damage evolution is the following (in ABAQUS, a broken portion of the cohesive element is drawn with an horizontal line at $y = 1$ because the software describes the percentage of progressive damage, fig. 4.35, 4.36, 4.37, 4.38)

Model	**Adherends**		**Adhesive**	
	Number	**Type**	**Number**	**Type**
4 plies	324	CPE4	40	COH2D4
8 plies	648	CPE4	40	COH2D4

Table 4.12: Mesh properties - Study of damage for cohesive elements.

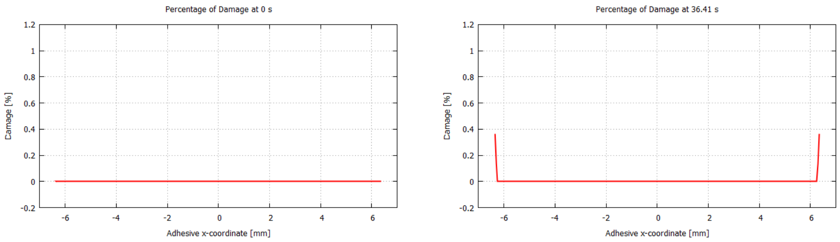

Figure 4.35: Percentage of damage evolution: on the left, at the 0% of the entire displacement corresponding to the total time period of the ABAQUS analysis; on the right, at the 60.68%.

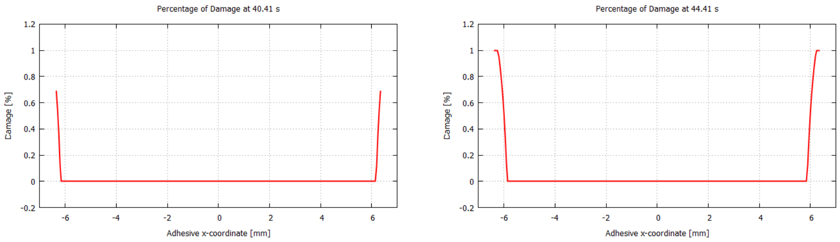

Figure 4.36: Percentage of damage evolution: on the left, at the 67.35% of the entire displacement corresponding to the total time period of the ABAQUS analysis; on the right, at the 74%.

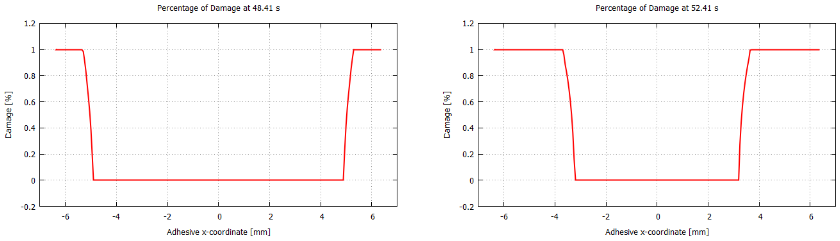

Figure 4.37: Percentage of damage evolution: on the left, at the 80.68% of the entire displacement corresponding to the total time period of the ABAQUS analysis; on the right, at the 87.35%.

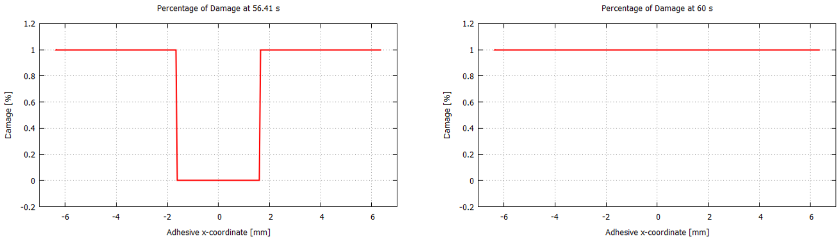

Figure 4.38: Percentage of damage evolution: on the left, at the 94% of the entire displacement corresponding to the total time period of the ABAQUS analysis; on the right, at the Total displacement.

In fig. 4.37 the length of the broken part of the adhesive is almost 1.35 mm which is a very convenient distance to place the virtual gauges because the half-length of the adhesive is 6.35 mm (fig. 4.39).

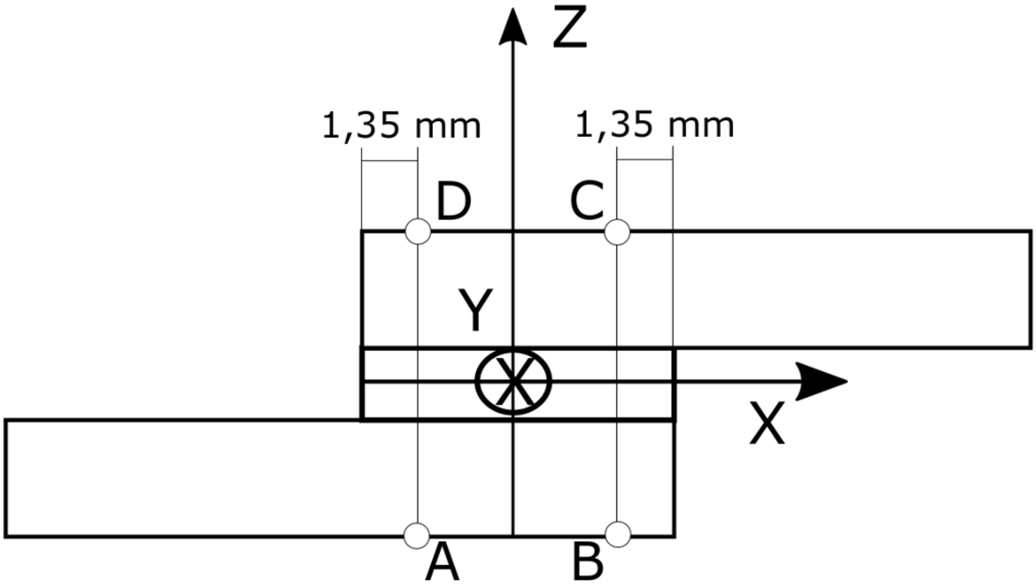

Figure 4.39: Single Lap geometry used for the analysis: the white dots positioned on the adherends are are the four virtual gauges used for analysis.

At first, a convergence test between the gauges **A** and **C** and between the gauges **B** and **D** was performed in order to validate the model and to appreciate its solidity and similarity to a real experiment: due to the symmetrical geometry, loads and boundary conditions, the values of Peel and Shear stresses found are the same across the gauges. Then, the evolutions of Peel and Shear stress during the entire test are shown for the 4- and 8-plies adherends in fig. 4.40, 4.41, 4.42, 4.43 (results have been normalised by the Young's modulus of the adhesive to make the results independent from the material used): at the step corresponding to 48.41 s, the peaks of stresses are evident, demonstrating a correlation between the damage propagation in the adhesive and the values reached in the adherends, even if there is not a perfect correspondence. For Peel stress, the 8-plies adherends configuration shows lower peaks than 4-plies, achieving a numerical convergence of the model towards its values of stress.

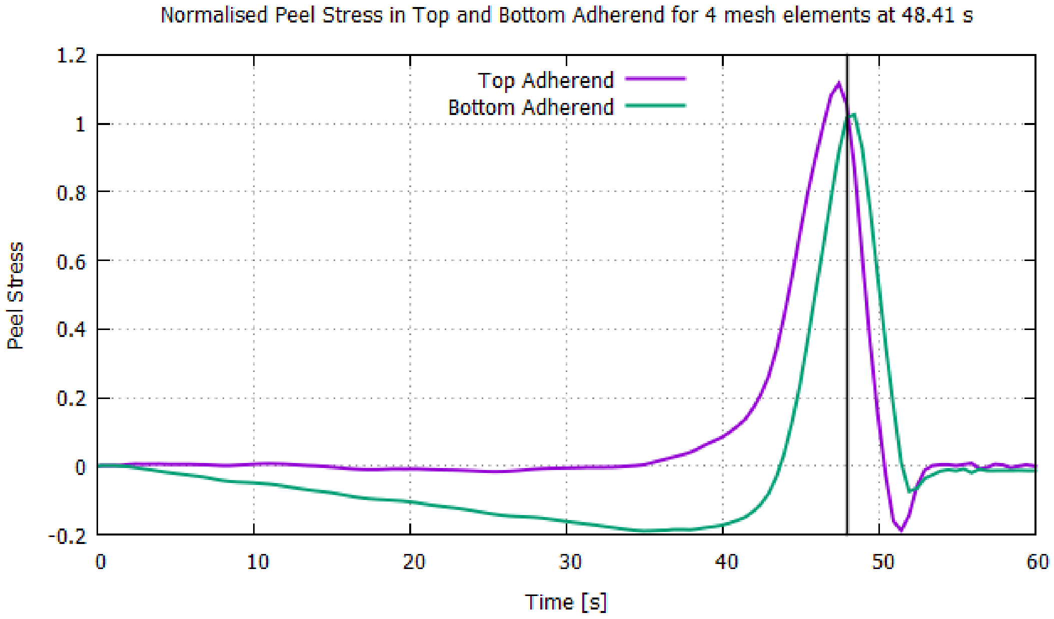

Figure 4.40: Peel Stress evolution for the 4-plies adherends analysis.

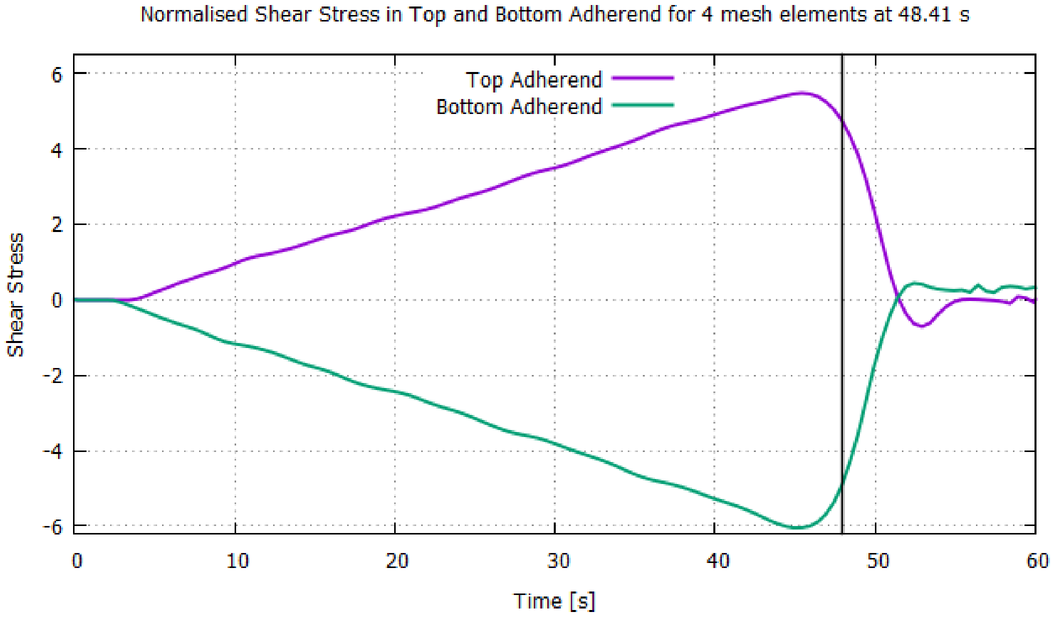

Figure 4.41: Shear Stress evolution for the 4-plies adherends analysis.

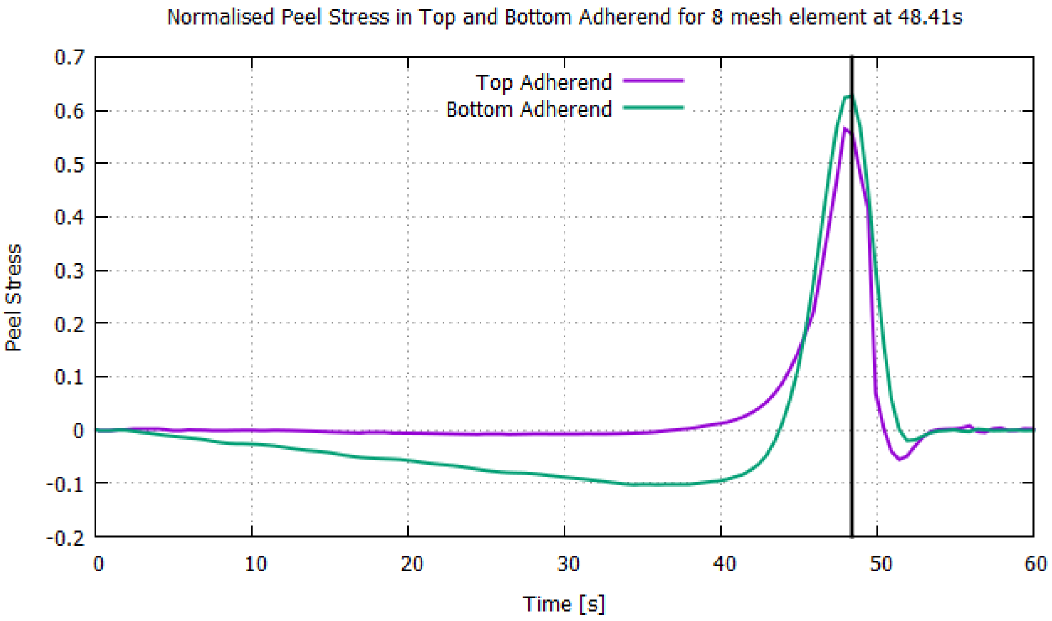

Figure 4.42: Peel Stress evolution for the 8-plies adherends analysis.

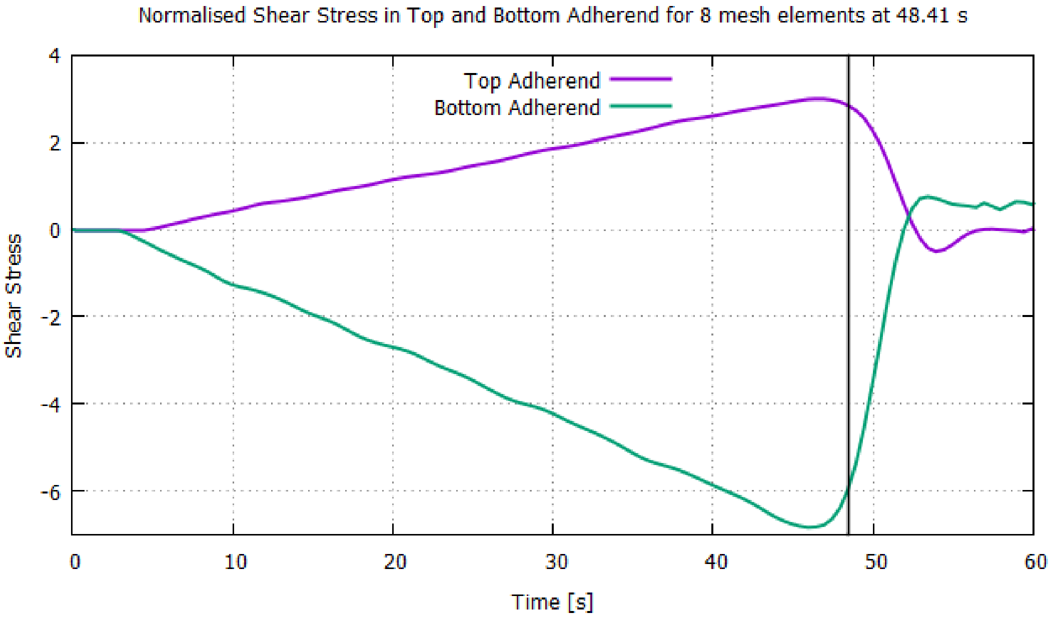

Figure 4.43: Shear Stress evolution for the 8-plies adherends analysis.

4.3.3 Composite materials and cohesive elements

Generally, the adherends of the bonded joints are made of composites which are materials obtained by the physical or chemical union of two or more materials macroscopically distinct and insoluble and having better technological properties than those of the components; the most used composite materials in aerospace engineering are made of a polymer matrix reinforced with fibres and they have little thickness, anisotropic characteristics in terms of elastic properties and toughness, high stiffness and strength. The Classical Lamination Theory (CLT) allows to analyse the global behaviour of laminated materials studying the relationships between loads, strains and stresses and it is based on the hypothesis which states that the plies are perfectly connected among them and an orthogonal plan to the middle plan before the deformation maintains its properties also after the deformation and, so, the continuity of strains and stresses is guaranteed through the interface, but composites have greater difficulties of analysis compared to isotropic materials and in fact for them the FEM numerical methods will be used instead of analytical solutions; composites in FEM can be described both as shell elements so having one element in the thickness, homogeneous properties through the thickness and able to study the deformations in plane stress conditions and solid elements, having more than one element in the thickness, orthotropic properties and able to study the interlaminar stresses.
In this section, the bonded single lap joint will be modelled with the same cohesive adhesive as before, but with composite shell type adherends made of HM Graphite/epoxy with the following physical and mechanical properties:

Elastic Properties	**HM Graphite/epoxy**
E_1 [GPa]	230
E_2 [GPa]	6.6
G_{12} [GPa]	4.8
ν_{12}	0.25

Table 4.13: Composite layers: material properties.

For adherends, naming x and y respectively the longitudinal and vertical axis and rotating plies around this latter, two configurations and different angle orientations will be studied; for simplicity and to keep the plots as clear as possible, the analysis will be named on the basis of the angle of orientation of the ply at the interface between the adherends and the adhesive in the following way:

- Adherends made of 4 plies:
  - *Interface 0°*: $[0°/90°]_s$
  - *Interface 45°*: $[45°/0°]_s$
  - *Interface -45°*: $[-45°/0°]_s$
  - *Interface 90°*: $[90°/0°]_s$

- Adherends made of 8 plies:
    - *Interface 0°*: $[0°/45°/\text{-}45°/90°]_s$
    - *Interface 45°*: $[45°/\text{-}45°/0°/90°]_s$
    - *Interface -45°*: $[-45°/45°/0°/90°]_s$
    - *Interface 90°*: $[90°/45°/\text{-}45°/0°]_s$

Adhesive is modelled as a cohesive elements having the same properties described in the previous section. The models have been studied with dynamic implicit analysis and a time period of 60 steps corresponding to a minute of testing; concentrated loads applied on the mesh point act of respectively -150 N on the left side and 150 N on the right side (to keep an almost equivalent loading field as the code and [34]) with a tabular amplitude and on the interfaces between adherends and adhesive a no friction property with hard contact has been imposed not to affect the results with friction interaction between those surfaces; vertical displacements are blocked with carriages on the adherends (recreating the two elements of 12.7 mm on the left and right extremities) and the central node of the structure is clamped in the horizontal direction in order to implement the exact equivalent boundary conditions as the previous models: results for Peel and Shear stress for the two configurations (4- and 8-plies adherends) will be compared at the same step time and they have been normalised by the Young's modulus of the adhesive (to make the results independent from the material used). Results for the step corresponding to 20s and 60s are shown in order to have a comparison between stresses at the beginning and at the end of the test. For the model with 4 plies, the layers are two for each ply, while the model with 8 plies has one layer for each ply, so the number of total layers is the same (tab. 4.14).

Model	**Adherends**		**Adhesive**	
	Number	**Type**	**Number**	**Type**
4 plies	628	CPE4	40	COH2D4
8 plies	628	CPE4	40	COH2D4

Table 4.14: Mesh properties - Study of damage for cohesive elements.

In fig. 4.44 the curves have the same shape as literature and MUL^2 *CODE*, but the peaks of *Ply 90°* for 8-plies are higher than 4-plies: this shows that this type of plies configuration is the weakest among the other and it leads to early breakups of the lap because the fibres are positioned perpendicularly to the external loads applied on the extreme edges. The configuration for *Ply 0°* appears the strongest one among the others.

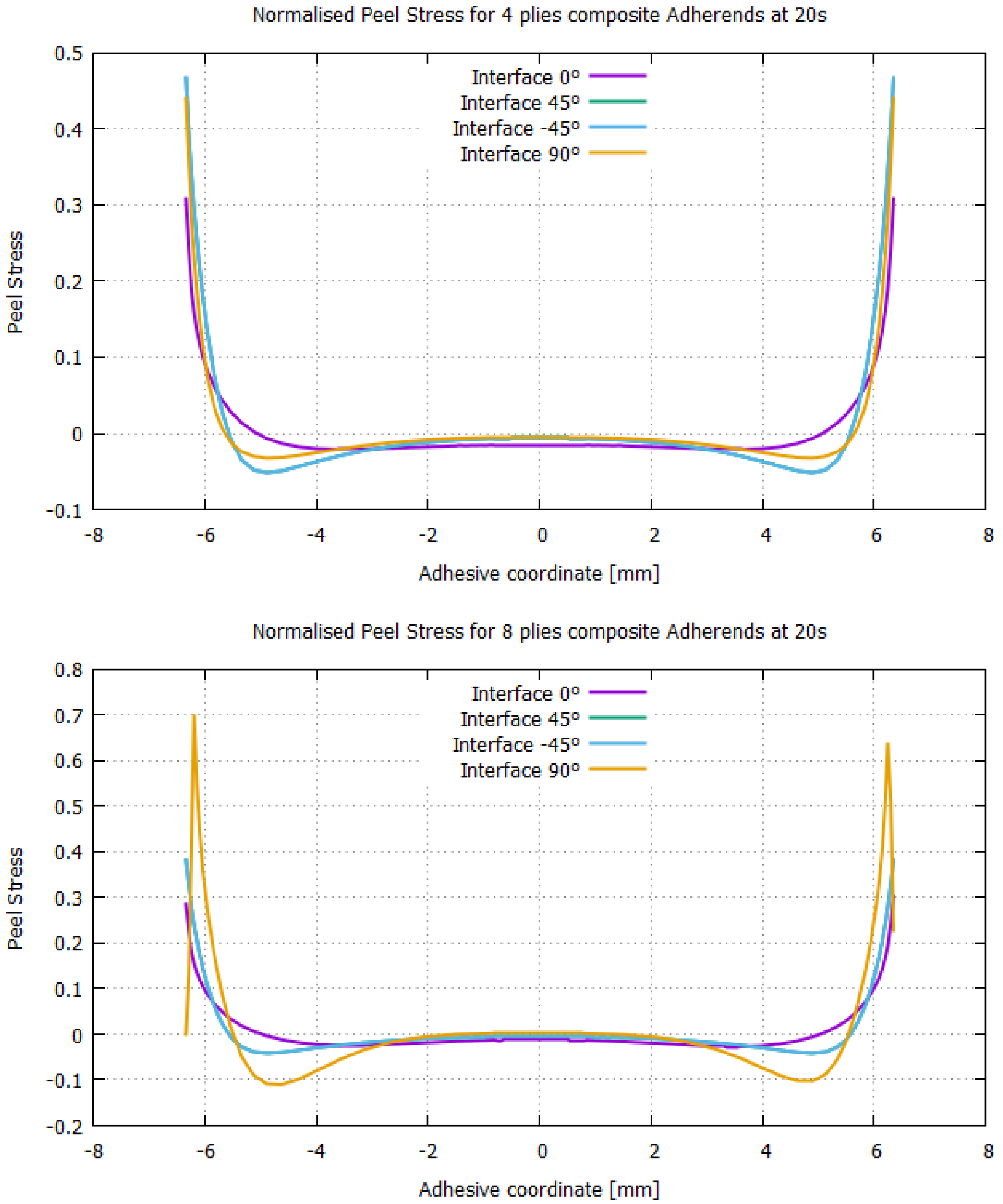

Figure 4.44: Peel Stress evolution for the 4-plies adherends (top) and 8-plies adherends (bottom) analysis evaluated at 1/3 of the entire displacement corresponding to the total time period of the ABAQUS test.

The curves of fig. 4.45 have the same shape as literature and MUL^2 *CODE*, but for 4-plies they have lower values due to a not totally correct modelling of this configuration for the lap joint: in fact, the *Ply 90°* configuration for 8-plies is able to detect the approaching breakup while for 4-plies the same configuration has only a little deviation from the shape as it is possible to see in the two lines which begins and ends the shape of the curve. As for Peel Stress, the configuration for *Ply 0°* appears the strongest one among the others.

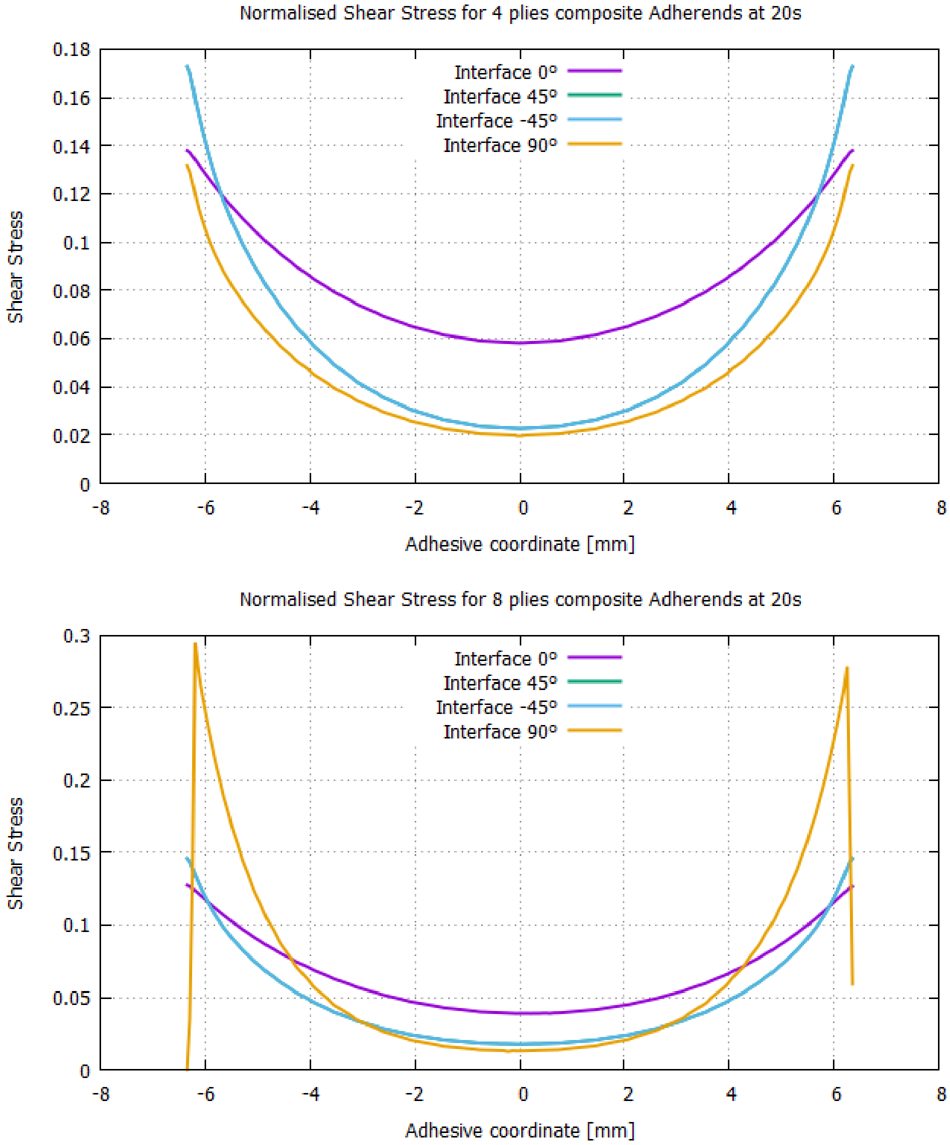

Figure 4.45: Shear Stress evolution for the 4-plies adherends (top) and 8-plies adherends (bottom) analysis evaluated at 1/3 of the entire displacement corresponding to the total time period of the ABAQUS test.

At the end of the test (fig. 4.46), the *Ply 90°* configuration demonstrates the lowest performances and in fact it is the first composite material which has breakups for a great length in the adhesive element (almost 2 mm, but also the *Ply 45°* and *Ply -45°* configurations (which are overlapped) express their weakness in tensile loading applications. The non-symmetry of the plots is due to numerical approximations made by the software's computational solver. As for the same plot for Peel Stress at the time step corresponding to 20s, the configuration for *Ply 0°* rests the strongest one among the others.

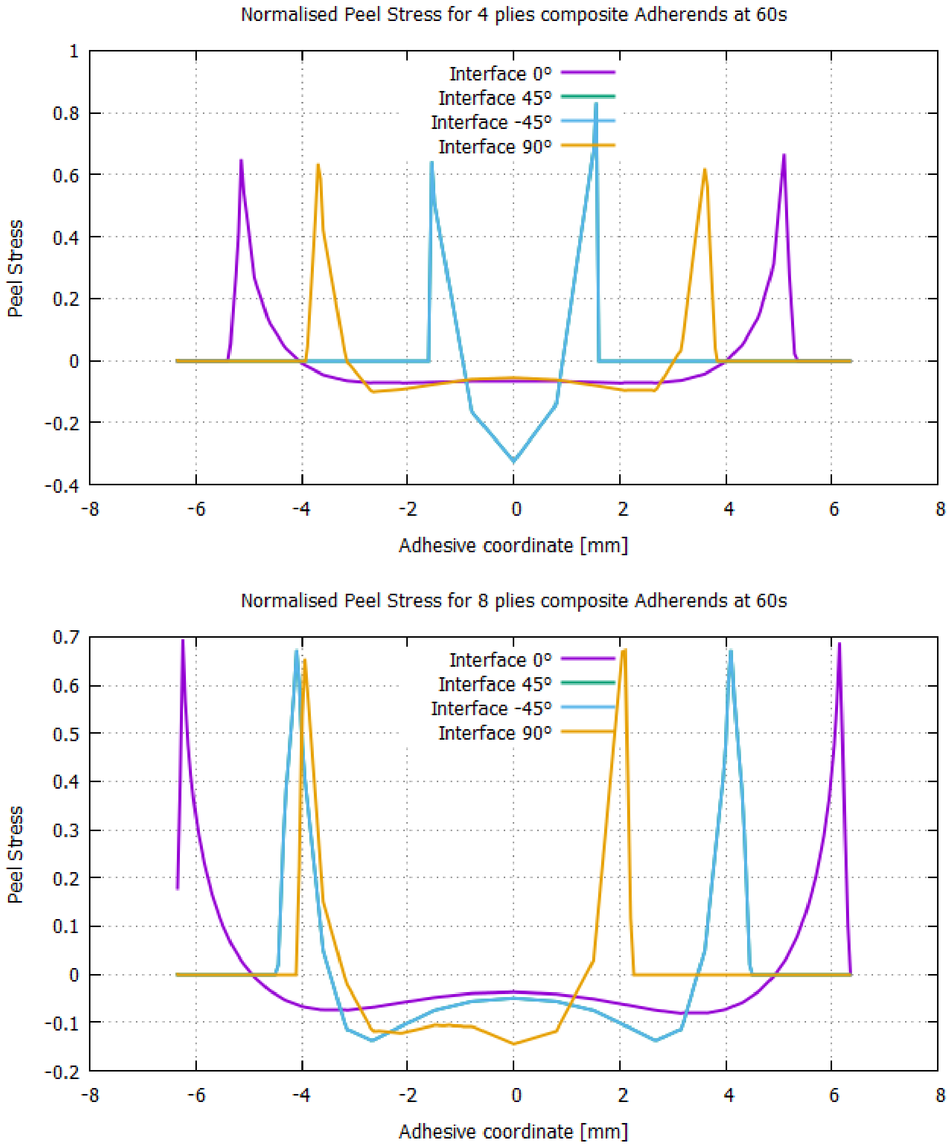

Figure 4.46: Peel Stress evolution for the 4-plies adherends (top) and 8-plies adherends (bottom) analysis evaluated at the total displacement corresponding to the Total time period of the ABAQUS test.

At the end of the test (fig. 4.47), the configuration for *Ply 0°* demonstrates its strength among the others because it shows almost the same minimum peak value as the other configurations (in 8-plies the peak converges to a lower result than for 4-plies) and it also does not experience breakups, although the two external edges of the curves express a damaged adhesive. As expected, the *Ply 90°* configuration is the weakest one and it reveals its lack of structural and engineering importance for a single lap joint model.

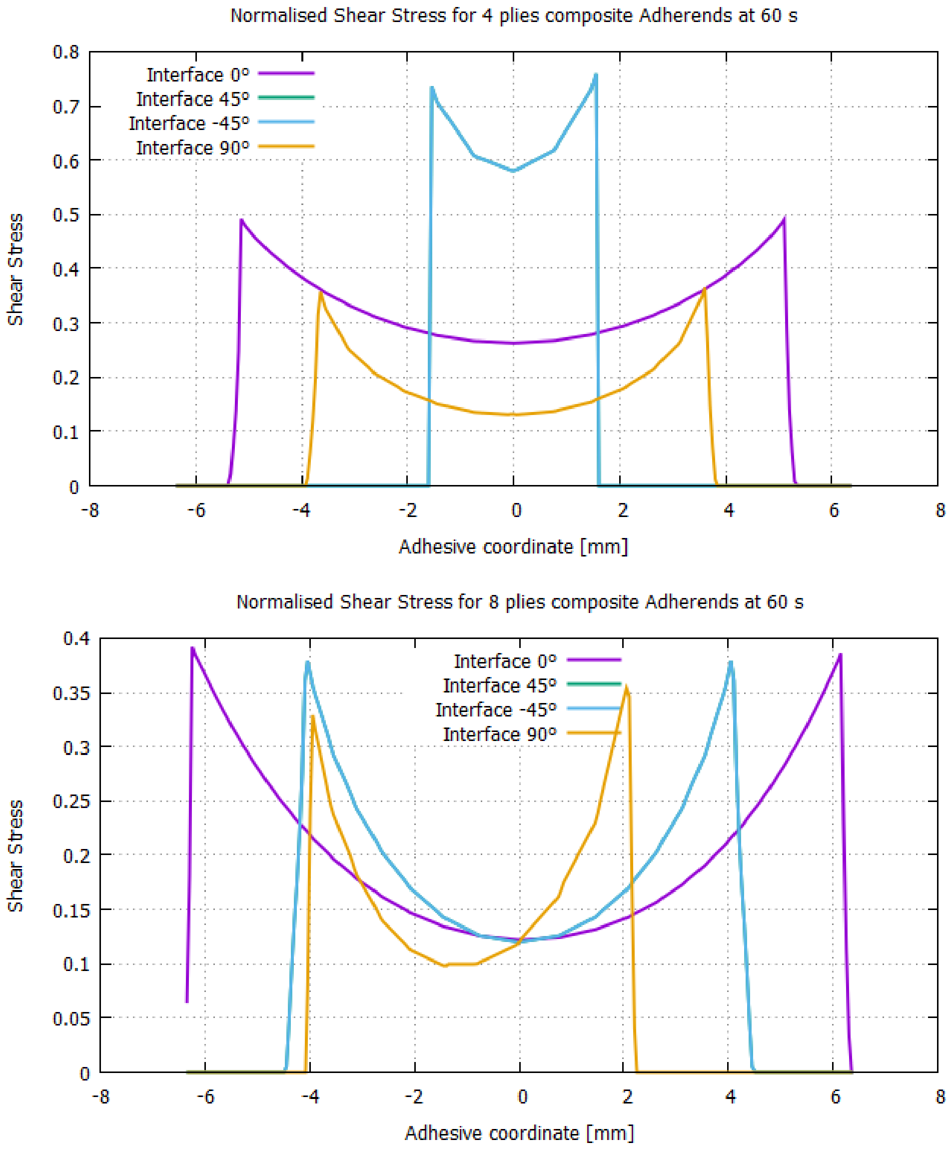

Normalised Shear Stress for 4 plies composite Adherends at 60 s

Normalised Shear Stress for 8 plies composite Adherends at 60 s

Figure 4.47: Shear Stress evolution for the 4-plies adherends (top) and 8-plies adherends (bottom) analysis evaluated at the total displacement corresponding to the Total time period of the ABAQUS test.

4.4 Hybrid-adhesive double lap joint

In order to reduce Peel and Shear stresses, a combination of stiff and flexible adhesives along the bondline can be used, as analysed by Pires et al. in [24]: Pires' results indicate that joints' strength can be optimised by appropriate geometrical and material property selection to become higher for joints with bi-adhesive bondlines compared with those with single adhesives in the bondline. The double lap joint studied derives from Ozer & Oz's works[22] (the case analysed is $l_1/l_2 = 0.7$): *Aluminum alloy 7075* was used as inner and outer adherends, *Hysol EA9313* and *Terokal 5045* epoxy adhesives were used as stiff and flexible adhesives, respectively; the double lap joint has the following geometrical and physical characteristic (fig. 4.48, tab. 4.15) taken from [22, pag. 51]:

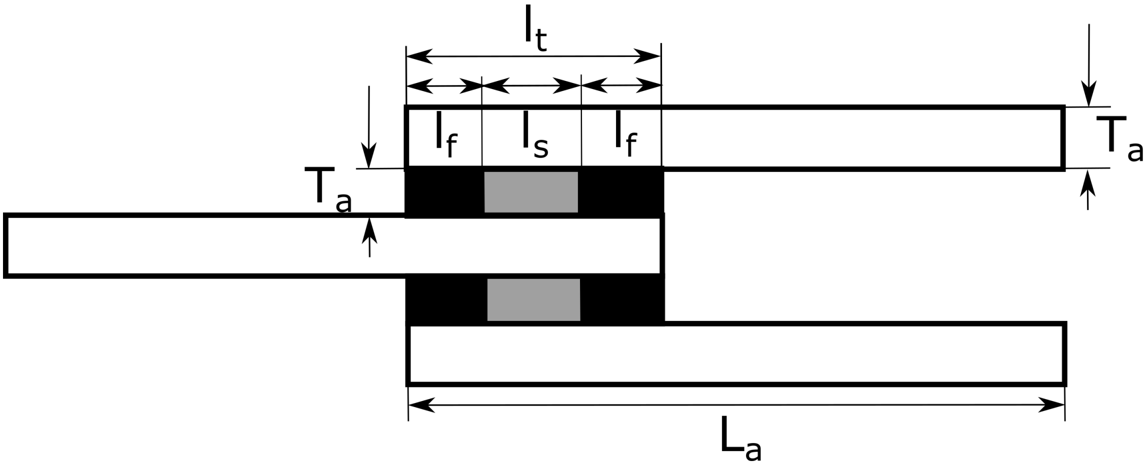

Figure 4.48: Double Lap Joint, Ozer & Oz.

Geometrical characteristics	**Value**
l_f	3.6456 mm
l_s	5.208 mm
L_a	100 mm
width	25 mm
T_a	1.5 mm
$E_{Adherend}$	71.7 GPa
$E_{FlexibleAdhesive}$	0.4374 GPa
$E_{StiffAdhesive}$	2.274 GPa
$\nu_{Adherend}$	0.33
$\nu_{FlexibleAdhesive}$	0.38
$\nu_{StiffAdhesive}$	0.36
σ	3.6 kN

Table 4.15: Hybrid-adhesive double lap joint - Material and geometrical properties.

4.4.1 First Approach: cross axis, uniform mesh

The double joint (fig. 4.49) is bounded through x- and z- in the outer adherends and only through x-axis in the inner adherend; each 4^{th} node of the cross section's $2B4$ (fig. 4.50) has been bounded through y-axis (tab. 4.16). A load of 3.6 kN is applied to the left side of the inner adherend and, after normalising values by the average value of σ_{xz}, graphical results can be obtained (fig. 4.51, 4.52).

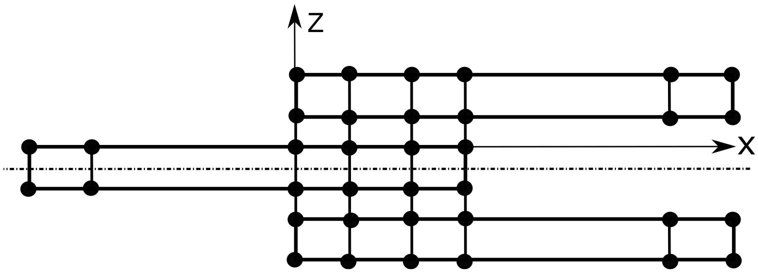

Figure 4.49: Hybrid-adhesive double lap joint cross section HLE discretization.

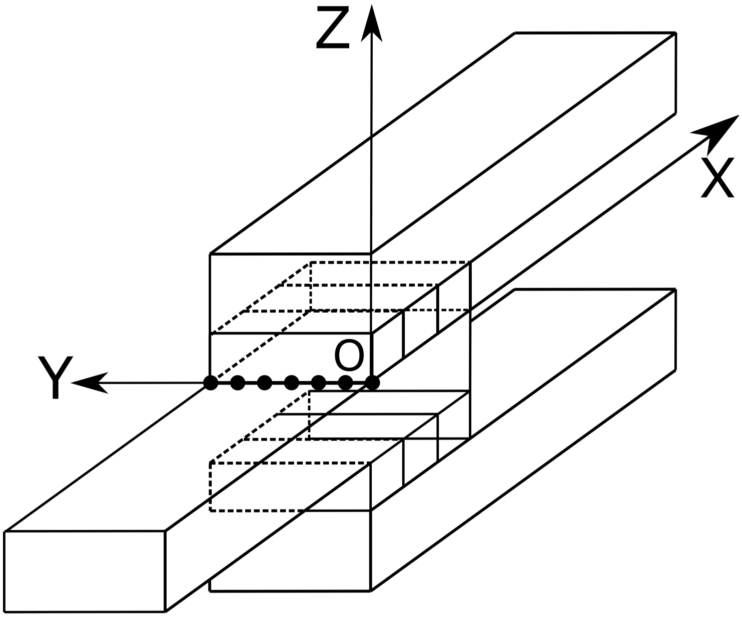

Figure 4.50: Hybrid-adhesive double lap joint mesh: cross axis.

Model	DOFs	Peel Stress	Shear Stress
HLE 6	9282	0.6673	1.3632
HLE 7	12222	0.6583	1.3522
HLE 8	15603	0.6597	1.3289
Ozer & Oz	/	0.7032	1.3333

Table 4.16: DOFs and Max values of Peel and Shear stress at the free edges - Hybrid-adhesive double lap joint: uniform mesh (1^{st} approach).

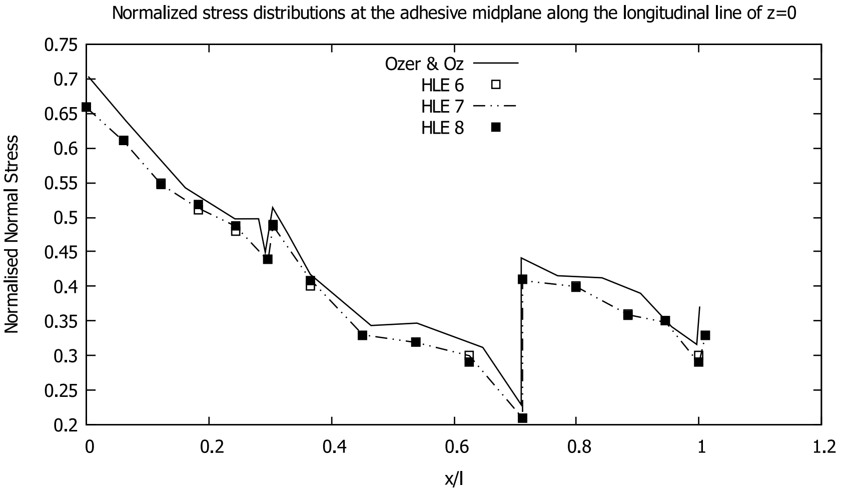

Figure 4.51: Peel Stress - Hybrid-adhesive double lap joint: uniform mesh (1^{st} approach).

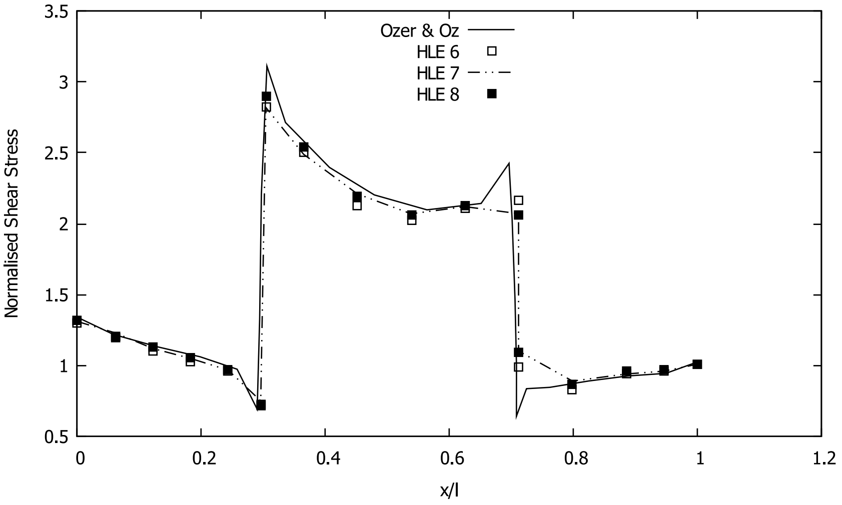

Figure 4.52: Shear Stress - Hybrid-adhesive double lap joint: uniform mesh (1^{st} approach).

4.4.2 Second Approach: longitudinal axis, uniform mesh

In the second approach, the axis considered is the longitudinal axis: in this way, variable sections through the longitudinal axis can be evaluated (Fig. 4.53). Mesh can be changed for the different regions without changing the global connectivity (Fig. 4.54): in order to study the mechanical behaviour at the connection point between adherend and adhesive and between Stiff and Flexible adhesives, a graded mesh is highly recommended (fig. 4.55, 4.56, tab. 4.17).

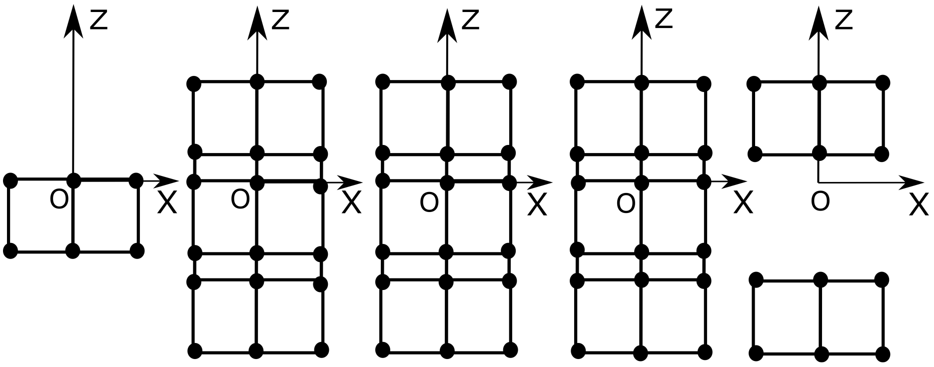

Figure 4.53: Hybrid-adhesive double lap joint cross section HLE discretization: the three central ones correspond to the cross section of the Flexible Adhesive, then the Stiff Adhesive and then again the Flexible Adhesive.

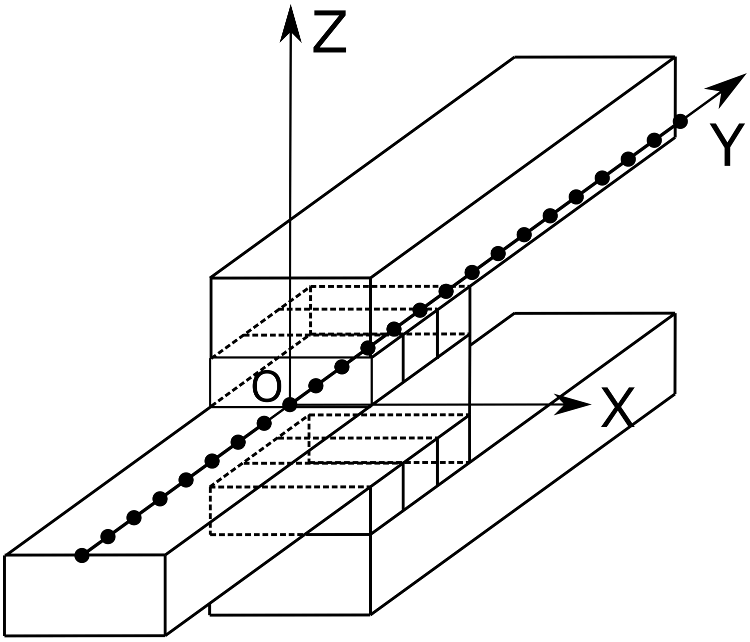

Figure 4.54: Hybrid-adhesive double lap joint mesh: cross axis.

Model	DOFs	Peel Stress	Shear Stress
HLE 6	13869	0.6598	1.3741
HLE 7	18228	0.6682	1.3602
Ozer & Oz	/	0.7032	1.3333

Table 4.17: DOFs and Max values of Peel and Shear stress at the free edges - Hybrid-adhesive double lap joint: uniform mesh (2^{nd} approach).

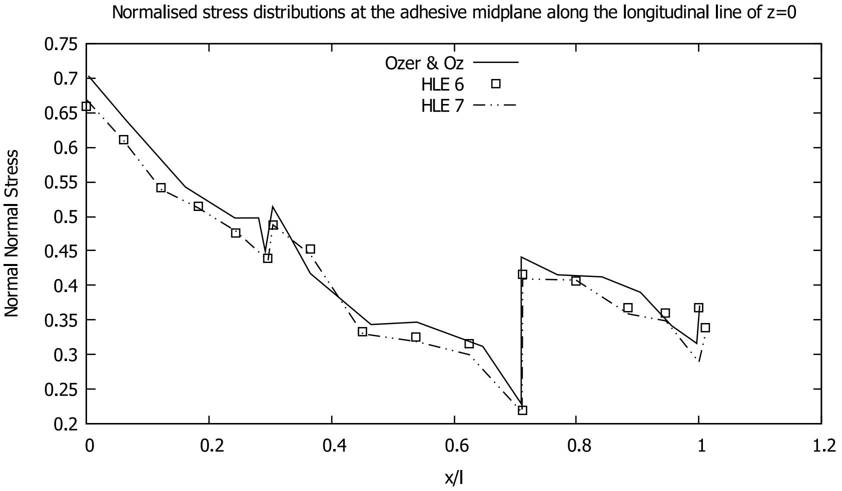

Figure 4.55: Peel Stress - Hybrid-adhesive double lap joint: uniform mesh (2^{nd} approach).

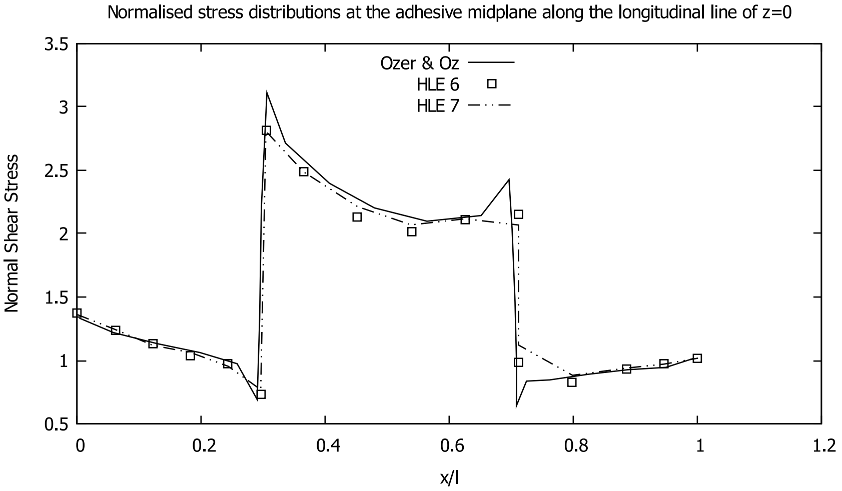

Figure 4.56: Shear Stress - Hybrid-adhesive double lap joint: uniform mesh (2^{nd} approach).

Chapter 5

Conclusions

Three different types of joints with increasing complexity have been investigated in this thesis.
The first part of the results are devoted to the assessment of MUL^2 *CODE* implemented for the first time with Hierarchical Legendre Expansion Order. The use of Carrera Unified Formulation has been fundamental in order to write the displacements field in a compact formulation. The second part concerns the complete study of a single lap joint in ABAQUS proceeding by steps from homogeneous mechanical properties to orthotropic composite material for adherends and cohesive elements for adhesives.
The results showed by the present thesis allow to state that:

- The MUL^2 *CODE* based on HLE is an efficient method to study bonded joints and, generally, composites structures: numerical results and the global shapes of the curves obtained are very close to literature benchmarks and also to numerical exact solutions deriving from ABAQUS
- The MUL^2 *CODE* can detect the most relevant behaviours of the significant zones of a loaded structure as well as the commercial finite element package ABAQUS, for example having highlighted, using a thinner and thinner mesh in those regions, that the Peel Stress in the free edges of the single lap joints tends to zero
- Implementing a parametric *Python* code which use the ABAQUS solver can be the easiest way to perform excellent analyses on single lap joints because its results can achieve the same accuracy of the highest expansion order of MUL^2 *CODE*
- It is possible to collect precise information about the evolution of the stress adhesive characteristics which propagate through the thickness of the single lap joint by applying gauges on the external skin of the adherends
- The most important layer of an adherend made by composite is that one at the interface with adhesive which can determine more than the other ones (whose angles of orientation of fibres less affect the behaviour of the structure) the toughness of the lap

Bibliography

[1] https://www.journals.elsevier.com/international-journal-of-adhesion-and-adhesives.

[2] https://www.mae.ncsu.edu.

[3] http://www.mul2.polito.it.

[4] M. Tekelioglu A. Kaya. "Three dimensional stress analysis in adhesively bonded joints". In: *Department of Mechanical Education Sakarya University, Sakarya - Turkey* (1998).

[5] T.L. Andersson. "Fracture Mechanics - Fundamentals and Applications." In: *Department of Mechanical Engineering, Texas A&M University, CRC Press* (1991).

[6] "ASTM D35286. Standard test method for strength properties of double lap shear adhesive joints by tension loading". In: (2008).

[7] J. J. Bikerman. "The Science of Adhesive Joints". In: (1968).

[8] Tardini C. "La teoria della flessione di Navier: testimonianze delle prime applicazioni nella Francia nel XIX secolo". In: *Bollettino ingegneri* (2013), pp. 15–20.

[9] Kennon S. Carey G. "Adaptive mesh redistribution for a boundary element (panel) method." In: *International Journal for Numerical Methods in Enigineering* (1987).

[10] Petrolo M. Carrera E. Giunta G. "Structures Classical and Advanced Beam Theories". In: (2008).

[11] Petrolo M. Carrera E Pagani A. "Use of Lagrange multipliers to combine 1D variable kinematic finite elements". In: *Computers and Structures* (2013).

[12] Anita Catapano. "Stiffness and Strength Optimisation of the Anisotropy distribution for Laminated Structures". PhD thesis. Université Pierre et Marie Curie - Paris VI, 2013.

[13] R. D. Cook. "Concepts and Applications of Finite Element Analysis". In: *Wiley, New York* (1981).

[14] Z. Zhao F. Roters S. Zaefferer D. Raabe M. Sachtleber. "Micromechanical and Macromechanical effects in grain scale polycristal plasticity experimentation and simulation". In: *Elsevier Science Ltd* (2001), pp. 15–96.

[15] A. Beukers D.M. Gleich M.J.L. VanTooren. "Analysis and evaluation of bondline thickness effects on failure load in adhesively bonded structures." In: *Journal of Adhesive Science Technology* (2001), pp. 1091–1101.

[16] Bruce K. Donaldson. “Analysis of Aircraft Structures, An introduction”. In: *Cambridge Aerospace Press* (2008), pp. 68–79.

[17] Oded Rabinovitch Dvir Elmalich. “A high-order finite element for dynamic analysis of soft-core sandwich plates”. In: *Journal of Sandwich Structures and Materials* (2012).

[18] A. Pagani E. Carrera A.G. de Miguel. “Hierarchical theories of structures based on Legendre polynomial expansions with finite element applications”. In: *International Journal of Mechanical Sciences* (2017).

[19] M. Petrolo E. Carrera A. Pagani. “Use of Lagrange multipliers to combine 1D variable kinematic finite elements”. In: *Elsevier Ltd* (2013).

[20] M. A. Crisfield G. Alfano. “Finite Element Interface Models for Delaminaion Analysis of Laminated Composites: Mechanical and Computational Issues”. In: (2001).

[21] B. Zuccarello G. Marannano. “Adhesion and Adhesives - Science and Technology”. In: *Chapman Hall, London - New York* (1987).

[22] O. Oz H. Ozer. “Three dimensional finite element analysis of bi-adhesively bonded double lap joint”. In: *International Journal of Adhesion Adhesives* (2012), pp. 50–55.

[23] A. Lystrup H. Toftegaard. “A design and test of lightweight sandwich T-joint for naval ships.” In: *Applied Science Manufactures* (2005), pp. 1055–1065.

[24] J.F. Durodola A. Beevers I. Pires L. Quintino. “Performance of bi-adhesive bonded aluminium lap joints”. In: *International Journal of Adhesion Adhesives* (2003), pp. 215–223.

[25] G.R Irwin. “Analysis of Stresses and Strains Near the End of a Crack Traversing a Plate.” In: *Journal of Applied Mechanics 24* (1957), pp. 361–364.

[26] R.D. Adams J.A. Harris. “Effect of Preforming - Adherends on Static and Fatigue Strength of Bonded Composite Single Lap Joints”. In: *Langley Research Center Elampton, Virginia - NASA* (1984).

[27] R.D. Adams J.A. Harris. “Strength prediction of bonded single lap joints by nonlinear finite element methods”. In: *International Journal Adhesion Adhesives* (1984), pp. 65–78.

[28] Z. Suo J.W. Hutchinson. “Mixed-mode cracking in layered materials”. In: *Journal of Applied Mechanics* (1992), pp. 63–191.

[29] A.J. Kinloch. “Numerical experimental analysis of hybrid double lap aluminum-CFRP joints.” In: *Chapman Hall, London - New York* ().

[30] S. Krenk. “Non-Linear Modeling and Analysis of Solids and Structures.” In: *Cambridge University Press* (2009).

[31] Hart-Smith LJ. *Design methodology for bonded-bolted composite joints.* Flight Dynamics laboratory - Wright Patterson Air Force Baie Aeronautical Laboratories - Ohio.

[32] E. Reissner M. Goland. “The stresses in cemented lap joints.” In: *Journal of Applied Mechanics* (1944), A17–A27.

[33] K. Chawla M. Meyers. “Mechanical Behaviour of materials”. In: *Bollettino ingegneri* (), pp. 15–96.

[34] J. R. Maddi M. Vable. “Boundary element analysis of adhesively bonded joints”. In: *International Journal of Adhesion Adhesive* (2006).

[35] Marianna Maiaru. “Multiscale approaches for the failure analysis of fiber-reinfoced composite structures using the 1D CUF”. PhD thesis. Politecnico di Torino, 2014.

[36] S.K. Mazumdar. “Composites Manufacturing”. In: *CRC Press, Boca Raton* (2002).

[37] L.E. Meade. “Joining Technologies for the 1990s”. In: *Buckley J.D and Stein, B.A. editors, Park Ridge, NJ* (1986).

[38] T. Belytschko N. Moes. “Extended Finite Element Method for Cohesive Crack Growth.” In: *Department of Mechanical Engineering, Northwestern University, USA* (2001).

[39] A. Needleman. “An Analysis of Decohesion Along an Imperfect Interface.” In: *International Journal of Fracture, Vol.42* (1990), pp. 21–40.

[40] A. Pagani. “Modelli Component-wise per analisi statica, dinamica e aeroelastica di strutture alari”. PhD thesis. Politecnico di Torino, 2011.

[41] Giunta G. Petrolo M Carrera E. “Beam structures: classical and advanced theories”. In: *John Wiley and Sons* (2011).

[42] A. K. Pickett and L. Hollaway. “The Analysis of Elastic Adhesive Stresses in Bonded Lap Joints in FRP Structures”. In: *Department of Civil Engineering, University of Surrey, Guildford, Surrey, (UK)* (1985), pp. 55–79.

[43] M.F. de Moura P.P. Camanho C.G. Davila. “Numerical Simulation of Mixed-mode Progressive Delamination in Composite Materials”. In: *American Society for Composites* (2002).

[44] N. A. Peppiatt R. D. Adams. “Stress Analysis of Adhesive Bonded Tubular Lap Joints”. In: *Department of Mechanical Engineering, University of Bristol, Queen’s Building* (1977).

[45] J. N. Reddy. “An introduction to the finite element method.” In: *McGraw-Hill* (1993), pp. 143–167.

[46] J.R. Rice. “A Path Independent Integral and the Approximate Analysis of Strain Concentration by Notches and Cracks.” In: *Journal of Applied Mechanics Vol. 35* (1968), pp. 379–386.

[47] Timoshenko S. “History of strength of materials”. In: (1953).

[48] E. Carrera S. Brischetto. “Static analysis of multilayered smart shells subjected to mechanical, thermal and electrical loads”. In: *Springer Science* (2013), pp. 1246–1289.

[49] A. Ochsner L. F. Martins da Silva. “Modeling of Adhesively Bonded Joints”. In: *Springer-Verlag Berlin Heidelberg* (2008), pp. 53–57.

[50] Tohru Nishigaya Hirohisa Ishikawa Toshiyuki Sawa Katsuhiro Temma. “Analytical Models with Stress Functions”. In: *Journal of Adhesion Science Technology, vol. 9, n. 2* (1994), pp. 215–236.

[51] J.W. Hutchinson V. Tvergaard. “The Relation Between Crack Growth Resistance and Fracture Process Parameters in Elastic-Plastic Solids.” In: (1992).

[52] W. Voigt. “Lehrbuch der Kristallphysik : mit Ausschlu d. Kristalloptik.” In: *Teubner,Leipzig* (1910).

[53] O. Volkersen. “Die Nietkraftverteilung in Zugbeanspruchten Nietverbindungen mit Konstanten Laschenquerschnitten”. In: *Luftfahrtforschung, Vol. 15* (1938), pp. 41–47.

[54] Jianqiao Ye. “Structural and Stress Analysis: Theories, Tutorials and Examples”. In: *Composite Structures* (2012), pp. 12–20.

[55] E. Zappino. “Variable kinematic 1D, 2D and 3D models for the Analysis of Aerospace Structures”. PhD thesis. Politecnico di Torino, 2014.